TOMOGRAPHIC RECONSTRUCTION OF VOID - FRACTION PROFILES IN A MERCURY - NITROGEN FLOW SYSTEM

by

P. Jaya Kumar

NUCLEAR ENGINEERING & TECHNOLOGY PROGRAMME

INDIAN INSTITUTE OF TECHNOLOGY KANPUR

FEBRUARY, 1996

TOMOGRAPHIC RECONSTRUCTION OF VOID FRACTION PROFILES IN A MERCURY-NITROGEN FLOW SYSTEM

A Thesis Submitted

in Partial Fulfilment of the Requirements

for the Degree of

Master of Technology

by

P. Jayakumar

to the

NUCLEAR ENGINEERING & TECHNOLOGY PROGRAMME
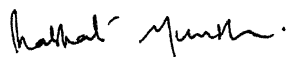
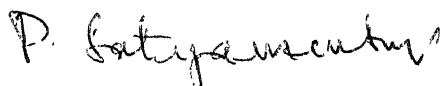INDIAN INSTITUTE OF TECHNOLOGY KANPUR

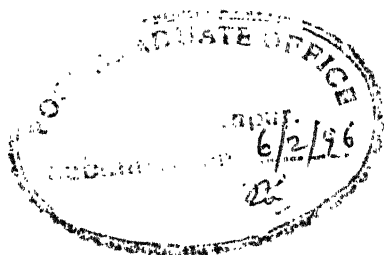February, 1996

NETP - 1996 - M - KUM - TOM

CERTIFICATE

It is certified that the work contained in the thesis entitled **Tomographic Reconstruction of Void-fraction Profiles in a Mercury-Nitrogen Flow System**, by **P. Jayakumar**, has been carried out under our supervision and that this work has not been submitted elsewhere for a degree.

Dr. Prabhat Munshi
Associate Professor
Department of Mechanical Engineering
and
Nuclear Engineering & Technology Prog.
Indian Institute of Technology
Kanpur
February, 1996

Dr. P. Satyamurthy
Scientist SG
Laser & Plasma Technology Division
Bhabha Atomic Research Centre
Bombay
February, 1996

ACKNOWLEDGEMENTS

ABSTRACT

Void fraction distribution in mercury-nitrogen flows is determined using gamma ray tomographic techniques. The measurements are made in the upcomer of the natural circulation loop of a Liquid Metal Magnetohydrodynamic (LMMHD) system. Measured cross sectionally averaged values range from 0.10 to 0.38 corresponding to nitrogen flow rates of 1.2 to 7.1 g/s. Tomographic reconstruction of the distribution from measured length-averaged values is done using the algorithm Chord Segment Inversion (CSI) and two of its modified versions. These algorithms assume radial symmetry in the property distribution and are thus suited to the present application. A formula (based on propogation of errors) is derived to find the error in the reconstructed values caused by the statistical nature of radioactive decay. The magnitude of dynamic bias error is calculated assuming the variation of void fraction in time to be similar to that of air-water flows for which such information exist. A minimum number of 3000 photon counts are collected per measurement to minimise errors due to Poisson uncertainty. Variations occuring in reconstructions for lower values of photon counts are experimentally ascertained.

Contents

List of Symbols

a_i, Area of the i'th zone.

A, Area of cross section

B, Build up factor

L, Length of chord through flow area.

N_l ,Number of photon counts with liquid filling the pipe.

N_g, Number of photon counts with gas filling the pipe.

N_{tp}, Number of photon counts with two-phase mixture filling the pipe.

r, radius

R, Inner radius of the pipe.

S_{jk}, Length of the j'th chord passing through the k'th zone.

t, time

α, void fraction.

α_i, Void fraction in the i'th zone.

$\bar{\alpha}(t)$, Instantaneous chord averaged void fraction

$\bar{\alpha}$, Chord-averaged void fraction.

$\hat{\alpha}$, Chord-averaged, time-averaged void fraction.

$\langle \alpha \rangle$, Cross sectionally averaged void fraction.

λ path length.

μ_l Linear attenuation coefficient of the liquid.

μ_g Linear attenuation coefficient of the gas.

μ_p Linear attenuation coefficient of the pipe material.

$\sigma_{\alpha i}$ Statistical error in α_i

$\sigma_{\bar{\alpha} i}$ Statisticala error in α_i.

τ measurement time.

List of Figures

List of Tables

Chapter 1

INTRODUCTION

1.1   Overview

This thesis is on the measurement of void fraction distribution across the cross section of a mercury-nitrogen two-phase flow using tomographic techniques. The mercury-nitrogen flow is that of the upcomer of the natural circulation loop of a Liquid Metal Magneto-Hydrodynamic (LMMHD) system. Measurements have been made for various flow rates of the mixture.

The determination of the void fraction distribution proceeds in two steps. First is the collection of data from the system to calculate length-averaged values at different locations of the cross sectional plane of the pipe. Second, the subsequent computations using tomographic algorithms to calculate the local values. The measurement of length-averaged void fraction is by means of the familiar gamma-ray attenuation technique. The tomographic algorithms used make use of the inherent radial symmetry of such flows, enabling considerable savings in the quantity of data required to be collected.

The information of void fraction distribution from this LMMHD system

1

will be of interest to the general two-phase flow studies. Also, this will contribute towards the optimisation of the system as the behaviour of the two-phase mixture in the upcomer is . critical to its overall performance. While this is so, this thesis confines itself to the *process* of determining the void fraction. Further analysis of data so generated is not attempted.

Unfortunately, the results from the present measurements cannot be confirmed by independent methods. This is due to many reasons, including the complexity of the natural circulation loop and the nature of the fluid being used. However, possible errors have been identified, and magnitudes calculated wherever feasible.

Chapter 2 describes the tomographic algorithms used in the present work. Chapter 3 presents the experimental data and details on the flow system. The errors involved in the measurements are discussed in Chapter 4, and estimates have been derived . The Results are presented in Chapter 5.

1.2   LMMHD systems

The objective of this section is to briefly describe the basic operations of Magneto Hydrodynamic (MHD) systems with emphasis on the Liquid Metal Magneto Hydrodynamic (LMMHD) systems. The promise that such systems hold for more efficient generation of electricity and the relevance of void fraction measurements in them are also discussed. Much of the information presented here is based on the article by P. Satyamurthy [1].

MHD power converters are based on the fundamental law of electrodynamic induction with the qualification that the conductor moving across the magnetic field (so that an electromotive force is induced in it) is a liquid. The conventional route to produce electrical energy from heat energy requires an intermediate conversion of heat to mechanical work. MHD systems obviate this requirement. They also achieve higher thermodynamic efficiences enabling power generation from low-grade heat sources.
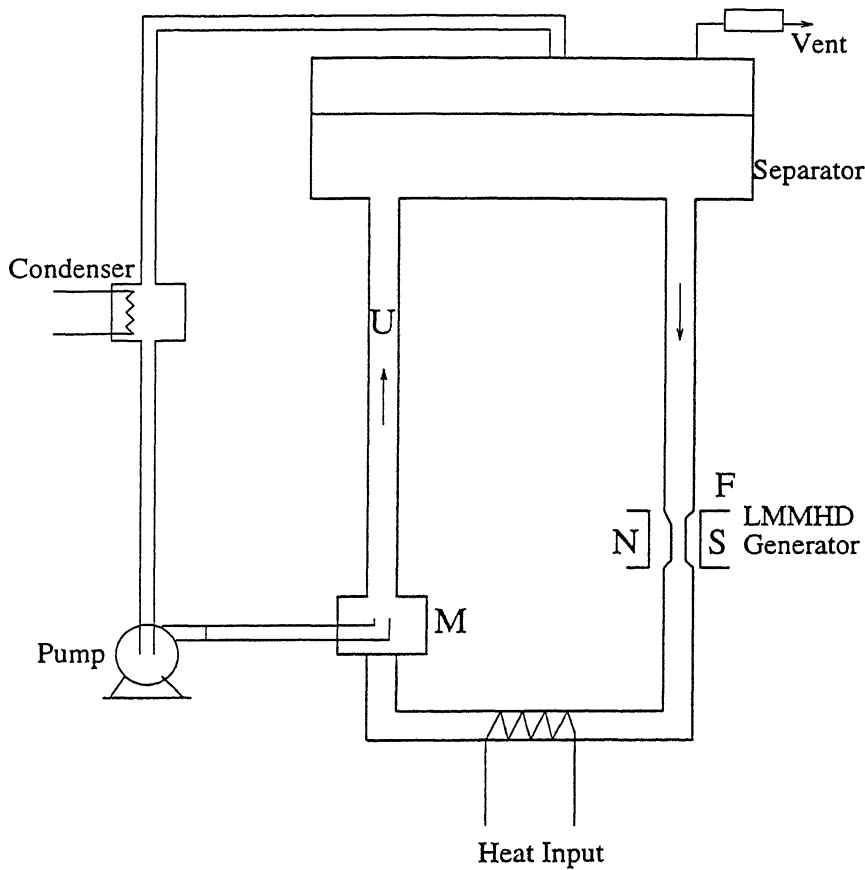
Figure 1.1: Gravity based LMMHD system

1.2.1 Classification

MHD systems can be classified according to the conducting fluids employed in them. Systems using ionised gases (plasma) as the conducting fluid are known as Plasma based MHD convertors. Liquid Metal MHD systems use a liquid metal as the conductor.

LMMHD systems can be further classified into gravitational (vertical) and non-gravitational (horizontal) systems. The experimental set-up in which the present void fractionmeasurements were carried out belongs to the former class.

1.2.2 Gravity Based LMMHD Systems

Figure 1.1 schematically shows the basic configuration of a gravity based LMMHD system. The principal components of the system are upcomer (U),

downcomer (D), mixer (M) and the MHD generator (G). Heat energy is added to the liquid metal by means of a heat exchanger. A vapour, gas, or volatile liquid (called the thermodynamic fluid) is introduced into the mixer at an appropriate pressure and temperature. The two-phase fluid thus created flows to the separator through the the upcomer. The thermodynamic fluid is removed at the separator (S), condensed, and returned to the mixer. The pressure differential created between the upcomer and downcomer establishes a natural circulation of the liquid metal in the system. A single phase flow of the liquid metal alone takes place in the downcomer and electrical power is extracted from the MHD generator located at its bottom.

1.2.3   Present Status

Early research into LMMHD systems began at the Jet Propulsion Laboratory, USA began in the 1960s. Commercialisation of the LMMHD Energy Conversion Technology was achieved by Professor Branover and co-workers of the Ben-Gurion University, Israel through their ETGAR programmes. The ETGAR-3 plant, commercialised in 1985, is delivering 8 kW of electrical power. It employs lead-bismuth alloy as the electrodynamic fluids and steam at 170 deg.C as the thermodynamic fluid. ETGAR-5 producing 650 kWe is a cogeneration plant set up at Negev in Israel. It consists of a high pressure and low pressure twin loop, with steam and lead as the fluids.

In India, a 500 We steam-mercury LMMHD facility is at an advanced stage of completion at the Bhabha Atomic Research Centre (BARC), Bombay. The design details of this facility have been summarised by P. Satyamurthy et al. in Ref. [2]. At the present stage of development the natural circulation of mercury is attained by admitting nitrogen at the mixer. An electrical heater of 10 kW is being setup to heat the mercury to 165 deg.C. On completion of this, it is proposed to introduce water at the mixer.

1.2.4   Relevance of Void-fraction Measurements in Upcomer

Several parameters are of interest towards the optimisation of the system for a given heat input. These include the total inventory of mercury, flow rates of

the electrodynamic and thermodynamic fluids, diameters of the upcomer & downcomer, magnetic field to be applied to the MHD generator etc. It may be noted that many of the parameters above are interdependent and a number of studies have been carried out to understand these interrelationships. Minimisation of the slip between vapour and liquid metal in the upcomer is of cruicial importance to achieve maximum liquid metal flow-rate (& power) for a given heat input. Hence the need to understand the complex two phase flow taking place in the upcomer. The present measurements of void fraction in the upcomer are expected to aid this understanding.

1.3 Literature Survey

Non-intrusive techniques based on the scattering and attenuation of gamma-ray, X-ray, β particles or neutrons have been employed by several researchers for the studies of two-phase flows. Jones & Delhaye [3], Rouhani & Sohal [4] and, more recently, Stekelenburg & van der Hagen [5] have reviewed them.

Studies to measure void fraction relate the absorption or scattering cross sections of the radiation to the density of the intervening fluid mixture. One way to classify these methods would be by the "resolution" achieved by them. Consider a plane where the distribution of a physical property $\mu(x, y)$ exists. As applied to two-phase flow studies, this plane is usually the cross section of a pipe normal to its axis and the physical property is void fraction $\alpha(x, y)$.

One-Shot techniques measure the cross sectional average of the property,

$$\langle \alpha \rangle = \frac{1}{A} \int \int \mu(x, y) dx dy \qquad (1.1)$$

where A is the area of cross-section. The beam used is collimated by a thin slit of small width. The length of the slit, perpendicular to the pipe-axis, is equal to or larger than the diameter of the pipe.

Beam Traverse methods give further information by evaluating the chordal-average,

$$\bar{\alpha} = \frac{1}{L} \int \mu(x, y) ds \qquad (1.2)$$

where L is the length of the beam passing through the flow area. The beam. collimated by a fine hole, is made to traverse the whole area of the plane. Note that a series of chordal-averages obtained at different positions can provide the cross-sectional average, $\langle \alpha \rangle$.

Tomographic techniques divide the plane into discrete regions and evaluate the property in each of them, thus comprehensively providing the distribution $\alpha(x, y)$. The data collection, in general, is through a number of sets of beam traverses, with each set done at a particular angle.

1.3.1   One-Shot and Beam Traverse Experiments

Heineman, Marechatere and Mehta [6] measured void fractions in NaK-Argon flows using the one-shot method. The flow was through a 1 in. conduit and an error of 20% is estimated in the range of 0 to 0.5 void fractions in comparison with another method they propose.

Isbin et al ([7], [8]) describe the measurement of chord-averaged void fractions in horizontal steam-water flows for various pressures. The gamma rays from a 20 curie Thulium-170 source where collimated into a beam of 1/32 in. and the readings were taken at steps of 1/16 in. across the pipe.

Gibson, Rennie & Say [9] made measurements of chord-averaged densities along the axis of a reactor containing a mixture of paraffin and water-gas. A 20 millicurie, Cs-137 source was used with the beam being collimated to 5 mm.

Pike, Wilkins, & Ward [10] employed polychromatic x-rays (10keV to 45keV) to determine the chord-averaged void fractions simulated by lucite mock-ups in 1 in. tubes. They show that the 0.035 in. thick tube wall of steel leaves only the 30 to 45 keV spectrum unattenuated, for which range the linear attenuation coefficient is constant.

Harms, Lo and Hancox [11] used a one-shot neutron attenuation method to estimate void fractions in mock-ups of lucite panels with holes of different

sizes. The incident neutrons were fast and epithermal and the detector was cadmium covered BF_3 counter. The neutron radiation is suggested to be more sensitive to hydrogenous flows than x-rays and gamma rays because of its higher macroscopic cross section in the medium of interest compared to that in the pipe walls.

Banerjee, Hussein and Menely [12] have proposed a neutron scattering method for measuring void fractions in two-phase flows. A fast and epithermal neutron beam, collimated by a 100×10 mm slit is incident on the test section. The scattered thermal flux is detected by 55 mm dia ^3He counter. The void fraction is found from the empirical relation

$$\langle \alpha \rangle = \frac{(N_g - N_{tp})}{(N_g - N_l)} \tag{1.3}$$

where N_g, N_l & N_{tp} are the counts observed with gas, liquid and two-phase mixture respectively filling the test-section. By simulating various flow regimes using aluminium-water test sections it has been showed that the scattered flux depended only on the mass of hydrogeneous material and not on its distribution. This is a definite advantage in view of the errors of the attenuation one-shot method mentioned in Ref. [13] due to preferential orientation of phases. The experimental results were interpreted by a Monte-Carlo simulation.

1.3.2 Tomographic Experiments

Zakaib, Harms and Vlachopoulos [14] utilised neutron beam attenuation to carry out tomographic reconstruction of a 2 cm. diameter lucite block with holes of known patterns in it. The study was done in order to apply the method to two-phase flows ultimately. Data was collected in a parallel beam geometry with 30 rays and 15 projections. An Algebraic Reconstruction Technique (ART2) was selected from several other iterative algorithms after trials with simulated data. The pixel array size used was 40×40. The neutron beam was 6.35 mm wide, and the ray spacing was 1.27 mm. Reconstructions for counting times of 20 seconds and 2 seconds are obtained. Simulations using different ART algorithms for various number of projections, number of
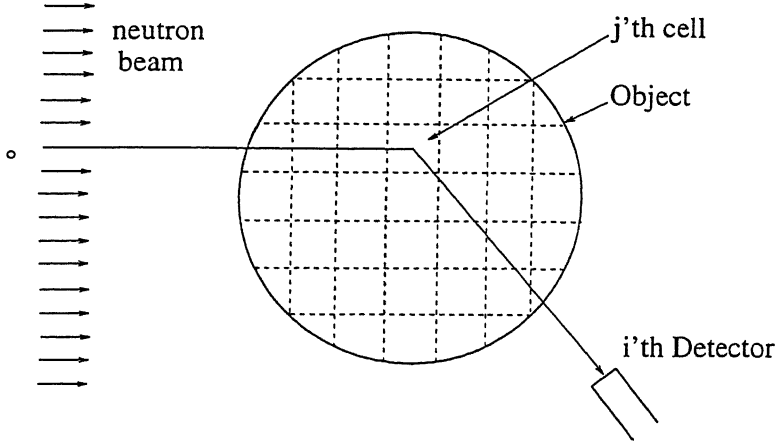
Figure 1.2: Schematic arrangement for SENT technique

rays, ray spacings, ray widths and counting times are compared. The loss in resolution because of ray-widths being greater than ray-spacings is found not to be significant.

Munshi [15] carried out tomographic void fraction reconstructions of actual air-water bubbly flows. The flow was through a 150 mm diameter pipe with cross-sectionally averaged void fractions ranging from 0.1 to 0.4. The data was collected in a fan-beam geometry mode. 6 scans, where each scan consists of 25 chordal-averages spaced at 2.5 deg., form one set of data. Gray values of the 40×40 pixel array is calculated by the Convolution-Back Projection (CBP) algorithm after transforming the data into the parallel mode. The estimated average error for the entire range is 0.04 void fractions. Kulacki et al. have summarised the main results and observations of this study in Ref. [16].This data has subsequently motivated the development of improved filter functions and a series of simplified algorithms specifically suited to radially symmetric two-phase flows.

Hussein and Meneley [17] proposed a Single Exposure Neutron (SENT) technique applicable to two-phase flows.
Figure 1.2 shows the schematic arrangement of the technique. A pipe carrying the two-phase flow is exposed to a beam of 14 MeV neutrons while a set of detectors surrounding the test section is used to measure the energy spectrum of the scattered neutrons. The energy of the scattered neutrons provide information on the location of water in the test-section and the num-

ber of neutrons of that energy reaching the detector provides information on the quantity of water. The number of scattered neutrons, at each discrete energy range of their spectrum, detected by detectors kept at different positions, forms the data. The direct SENT problem is posed as follows.

$$[A][\rho] = [s]$$

Here $[\rho]$ is the unknown vector of pixel densities, and $[s]$ is the data vector of dimension m, $m > n$. A is an $m \times n$ matrix whose element a_{ij} is calculated based on the contribution of cell j to the measurement s_i. The paper describes the mathematical and physical aspects of the experiments and reports reconstructions from various geometries of aluminium-water test sections.

Hummel and Wesser [18] briefly mention the results of a real time x-ray tomography study on two-phase flows of various regimes. The following parameters are considered as the pixel densities.

1. Mean of the PDFs of void-fractions

2. Second moment about the mean (Variance)

3. Third moment about the mean (Skewness)

Morooka et al. [19] have measured void fraction distrubutions in steam-water flows using a modified medical x-ray CT scanner. The test section was a 68×68 mm vertical channel with a 4×4 array of heated 12.3 mm dia rods simulating a BWR bundle. Data is collected in the parallel geometry mode with 8 rays and 30 views. The counting time per beam was 4 milliseconds, but counting was reapeated till successive values converged. The reconstruction on pixels of size 1×1 mm was carried out by Convolution Back Projection. The experiment was done in the following range of flow parameters. Pressure: 0.49 to 0.98 MPa, Mass flux: 3 to 5 $kg/cm^2 h$ and quality: 0 to 12%. The measured cross sectional averaged void fraction is compared with calculated values from various correlations.

Akira Inoue et al [20] have recently repeated the above work with an improved CT scanner and for a wider range of parameters. The test section is similar to a BWR tube bundle with an 8×8 heated rod array. The

flow parameters are closer to an actual BWR assembly. (Pressure: 1 to 8.6 MPa , Mass flux: 284 to 1998 kg/cm^2s and quality: 0 to 25 %). The CT scanner consists of an x-ray tube and 512 detectors. Data is collected in the fan beam geometry mode with 360 views. The reconstruction is finer, on 0.3×0.3 mm pixel elements. Effects of varying the quality and introducing unheated rods in the array are discussed. The results are compared with standard subchannel analysis computer codes.

Recently Thiyagarajan et al. [21] have reported void fraction profile measurements in mercury-nitrogen flows of their Liquid Metal Magnetohydrodynamic system. This is the same experimental system as that of the present work , and so the details are mentioned in Chapter 3.

1.3.3   Errors in Measurements

Review of literature shows that several researchers have contributed towards identifying and estimating the errors associated with the measurement of void fraction in two-phase flows using radiation attenuation techniques. These errors are relevant for the data collection in tomography also, and have been mentioned in the book by Herman [22] as,

1. Photon Statistics

2. Polychromaticity of the radiation beam.

3. Divergence of the beam from the source.

4. Time dependance of the measured property.

5. Detection of scattered photons.

6. Change in detector characteristics during measurement.

7. Mechanical instability of the measuring apparatus.

All these errors, except perhaps (2), are applicable to gamma-ray tomography of two-phase flows. Measures to combat error from one reason often leads to increased errors due to another. For instance, the fine collimation of a diverging beam reduces photon counts, resulting in poor statistics.

In this section literature on errors due to photon statistics and time dependance of measured property (dynamic bias error) is reviewed in some detail. These are felt to be more pertinent to the present study. Works relating to the other errors are only briefly mentioned.

Poisson Uncertainty

The usual precedure to estimate the statistical error in radiation attenuation due to the inherent random nature of radioactive decay is described in the book by Gardner and Ely [23]. This approach, followed by many authors, is as follows. The quantity to be ascertained from the measurement is expressed as a function of the number of photon counts detected. As the counts are governed by Poisson statistics, the uncertainty (1-σ) associated with N counts is $\sqrt{N}$. Then, applying the error propogation formula (see Section 4.1) to the expression relating the counts to the quantity being sought, the uncertainty in the measured quantity is determined.

Malaviya & Lahey [24] adopt the above approach to estimate the error in the measurement of instantaneous chordal-average in a two phase flow using their dual-beam x-ray technique. The percentage error for a given void fraction is expressed as a function of number of counts accumulated, chord length and linear attenuation coefficient of the liquid. The analysis is extended to evaluate the required source intensity for a specified error.

Schlosser, De Vuono, Kulacki and Munshi [25] have estimated the statistical error occuring in the pixel densities of the tomographic reconstruction of a two-phase flow density field with fan-beam mode of data collection. They have derived a relationship between the uncertainty in the pixel value and four other parameters, namely, diameter of the pipe, pixel size, measurement time and source strength. A parametric analysis using the above five independent variables is carried out to investigate the feasibility of adapting CT scanner for two-phase flow measurements.

Munshi and Vaidya [26] have studied the errors due to photon statistical fluctuations in the tomographic reconstruction of two-phase flow void fractions. The Poisson noise was simulated by adding random numbers within 1-σ confidence level to the data counts. The resulting reconstructions are

found to vary from the real ones most at the centre. Apparently, the errors show no preference for sign, and are significant if the data counts are less than 3000.

Dynamic Bias Error

Void fraction is stochastic in a local sense even in a steady-state flow. This time dependance of a property being measured by means of radiation attenuation results in dynamic bias error as the logarithm of a time-averaged value of measurement is not equal to the time-average of the logarithm of measurement.

The dynamic bias error was initially recognised and experimentally verified by Harms & Forrest [11]. Subsequently Harms & Laratta [27] have analysed this error in detail. We quote the following from their work.

The actual time-averaged, length-averaged void fraction which we seek to determine is given by

$$\hat{\alpha}_a = \frac{1}{\tau} \int_0^\tau \bar{\alpha}(t) dt \qquad (1.4)$$

where $\bar{\alpha}(t)$ is the instantaneous value of the chord-averaged void fraction and τ is the measurement time. It is shown in Ref. [27] that from a long-duration attenuation measurement, (assuming $\bar{\alpha}(t)$ to be constant) it is possible to calculate only,

$$\hat{\alpha}_m = \frac{1}{\lambda} \ln \left(\frac{1}{\tau} \int_0^\tau e^{\lambda \bar{\alpha}(t)} dt \right) \qquad (1.5)$$

where,

$\lambda = \mu_l L$

L = Length of the beam in the flow area.

τ = Measurement time.

$\hat{\alpha}_m$ = Measured chord and time averaged value under the assumption of constant void fraction.

The value of $\hat{\alpha}_m$ calculated by Eq. (1.5) is not equal to the value of $\hat{\alpha}_a$ given by Eq. (1.4) when $\bar{\alpha}(t)$ is varying with time. The dynamic bias error is then expressed as a function of $\bar{\alpha}(t)$ as,

$$\Delta\hat{\alpha}_D = \frac{1}{\lambda}\ln\left(\frac{1}{\tau}\int_0^\tau e^{\lambda\bar{\alpha}(t)}\right) - \frac{1}{\tau}\int_0^\tau \bar{\alpha}(t)dt \qquad (1.6)$$
$$= \hat{\alpha}_m - \hat{\alpha}_a \qquad (1.7)$$

Note that the determination of dynamic bias errors requires the knowledge of the variation of length-averaged void fraction with respect to time. An alternate expression for Eq. (1.7), which permits a more intuitive understanding, has been derived by Laratta & Harms [28] and is mentioned in Section 4.2.

Techniques to minimise dynamic bias error have been suggested by many researchers. Hancox & Harms [29] proposed a finite interval or 'gating' technique in which the measurements are made in a series of short-duration time intervals. The interval is so short that void fraction may be assumed to be effectively constant. Barret [30] discusses the statistical uncertainities which assume significance when measurement time is reduced for the gating technique. Interestingly, the probability distribution functions (PDFs) and moments of void fractions measured in small time intervals have revealed considerable information on two-phase flows. Jones & Zuber [31] and Vince and Lahey [32] have used this information to predict the flow regime. Some aspects of their works are described in Section 4.2.

Lahey, Krycuk and Malaviya [33] suggest another way to circumvent the dynamic bias error through electronically linearising the measurment signal by taking logarithms prior to time-averaging. They describe this method and the design features of their X-ray system employing it.

Wyman & Harms [34] have mathematically showed that the total void fraction error is specified by a PDF whose (a) mean is determined by the variation of $\bar{\alpha}(t)$ and (b) variance is determined by the poisson source fluctuations. They determine the upper and lower bounds of the time interval to be adopted in the gating technique for a pre-specified error in the calculated void fraction. In this comprehensive analysis, it is proved that the dynamic

bias error always causes the void fractions to be overestimated. In other words, that $\Delta\hat{\alpha}_D$ of Eq. (1.7) is always positive.

Other Errors

Errors due to preferential distribution of phases and detection of scattered photons are not of much importance to the present study. However, they are significant in One-shot experiments where the beam is not finely collimated as in a traversing technique.

Petric and Swanson [13] have studied the effects due to preferential distribution of phases in two-phase flow by simulating various flow-regimes with lucite patterns. The measurements show an average error of 36.5% for one-shot method and 7.3% for traversing technique in the range of 0.1 to 0.6 void fractions. This emphasises the prior knowledge of the flow regime for accurate one-shot results.

Harms, Lo and Hancox [35] incorporated the effects of build up in calculations for their one-shot nuetron attenuation experiment using lucite mock-ups. The build up factor is experimentally determined using the following expression.

$$B(x) = \left(\frac{I_L(x)}{I_0} \right) e^{\Sigma x} \qquad (0 < x < L) \qquad (1.8)$$

where

$x =$ Length of the beam in the flow area and

$I_L(x), I_0 =$ Intensity of the neutron beam with zero and full void respectively.

The void fraction is then iteratively evaluated from the expression below.

$$I_{TP}(x) = B\left(x(1-\alpha)\right) e^{-\Sigma x(1-\alpha)} I_0 \qquad (1.9)$$

A.M.C. Chan and S. Banerjee [36] have described the design procedure for a one-shot gamma densitometer to be operated in the count mode. The

selection of the optimum gamma source to provide sufficient sensitivity with a source strength for pre-specified poisson error is discussed. The shielding requirements are dictated by the source selected. Guide lines to choose suitable detector and signal processing instrumentation depending on the gamma ray energy and required count-rates are mentioned.

De Vuono, Schlosser, Kulacki and Munshi [37] discuss several aspects of the design of a CT scanner for two-phase flow measurements. The prototype scanner proposed by them uses 18 mCi Cs-137 source and collects data in the fan-beam mode with 48 detectors. The collimators are designed so as to keep the detection of scattered radiation below 5%, thus eliminating the need for pulse height analysis. This, in turn, enables the signal processing to be done in the current mode by which higher count-rates could be detected. The estimated error in pixel values is 3% for a spatial resolution of 1.15 cm and measurement time of 1 sec.

1.3.4   Tomographic Algorithms

The fundamentals and physical aspects of computerised tomography (CT) have been discussed in the book by G.T. Herman [22]. Munshi [38] has reviewed the applications of CT on two-phase flow studies.

The following definition of image reconstruction [22] (that is, the evaluation of point-densities in a plane) is apt for our purpose.

> Image reconstruction from projections is the process of producing an image of a two-dimensional distribution (normally of some physical property) from estimates of its line integrals along a finite number of lines of known locations.

In many two-phase flows through cylindrical pipes, an assumption that the property of interest is radially symmetric is valid. Incorporation of this radial symmetry has resulted in the recent development of the following three algorithms by Rathore et al. ([39] [40] & [41]).

1. Bessel Function Algorithm

2. Radial Polynomials

3. Chord Segment Inversion

These algorithms bring forth considerable savings in the quantity of data required to be collected and subsequent computations. The Bessel Function Algorithm and Radial polynomials are summarised in [38]. Chord Segment Inversion (CSI) is used in the present work, and is derived for a parallel-beam mode of data collection in Chapter 2. Recently the CSI algorithm has been modified by Thiyagarajan et al. [21] by making the system of equations overdetermined and obtaining the solution by least square solution. This modified algorithm, LSS, is also used in the present work and is described in chapter 2.

1.4 Objectives

1. To measure void fraction distribution across the cross section of mercury-nitrogen flows using radial gamma-ray tomographic techniques.

2. To compare the reconstructions from two algorithms LSS and Collapsed-CSI (C-CSI), to be introduced subsequently.

3. To calculate the statistical error in the reconstructed values.

4. To compare the reconstructions of data-sets with different values of constant-counts. To investigate whether reconstructions comparable to data with 3000 counts are possible with any lower value of the constant-count.

Chapter 2

TOMOGRAPHIC ALGORITHMS

2.1 Overview

Tomographic techniques are used to reconstruct the point-wise distribution of a function from a set of chord averaged values of the function. Simplified algorithms to find the void fraction distribution in radially symmetric two phase flows have been reviewed in Chapter 1.

The present measurements are on fully developed, steady flows at sufficient distances away from the point of mixing of the two fluids. Hence the assumption that void fraction distribution is radially symmetric is facilitated. In this Chapter we modifiy the algorithm Chord Segment Inversion (see Rathore et al. [41]) for parallel-beam mode of data collection. An overdetermined version of CSI, called Least Square Solution (LSS) (see Thiyagarajan et al. [21]) is described and a 'collapsed version', named Collapsed-CSI (C-CSI) is proposed. In this study, void fraction profiles are reconstructed using the above algorithms.

The chord-averaged values, multiplied by the length of the chord passing through the flow area, constitute the input data for the tomographic algorithms. We denote the chord-averaged value from the ith chord by $\bar{\alpha}_i$.

$$\bar{\alpha}_i = \frac{1}{L} \int_{C_i} \alpha(r, \phi) \, ds \qquad (2.1)$$

where,

s = Distance of the chord,

C_i = Path along s,

r, ϕ are the cylindrical co-ordinates and

L = Length of the ray in the flow area

In this work the chord-averaged void fraction along a particular chord is calculated by the familiar relation (see for eg., [23]).

$$\bar{\alpha}_i = \frac{\ln\left(I_{tp}/I_l\right)}{\ln\left(I_g/I_l\right)} \qquad (2.2)$$

where I_g, I_l and I_{tp} are the count rates (s^{-1}) obtained along the same chord with gas alone, liquid alone and two-phase alone in the pipe. Though the above formula is well known, for continuity and for explaining the assumptions made in it we freshly derive it in Appendix A.

2.2 Basic-Chord Segment Inversion Algorithm

The Chord Segment Inversion algorithm (abbreviated as CSI) is proposed by Rathore et al. [41] for a fan-beam geometry of data collection. The data for the present work was collected in a parallel-beam geometry. Hence, in this section, CSI is modified accordingly. Later in this Chapter, another version of CSI is suggested, and so, we refer to the original algorithm (after modifying it for parallel-beam geometry) as Basic-CSI (B-CSI).

Figure 2.1 shows the data collection geometry. In the parallel-beam geometry the chords C_i along which data is collected are parallel to each other, with each chord identified by its distance from the centre. We denote data from the kth chord by d_k.

Thus,
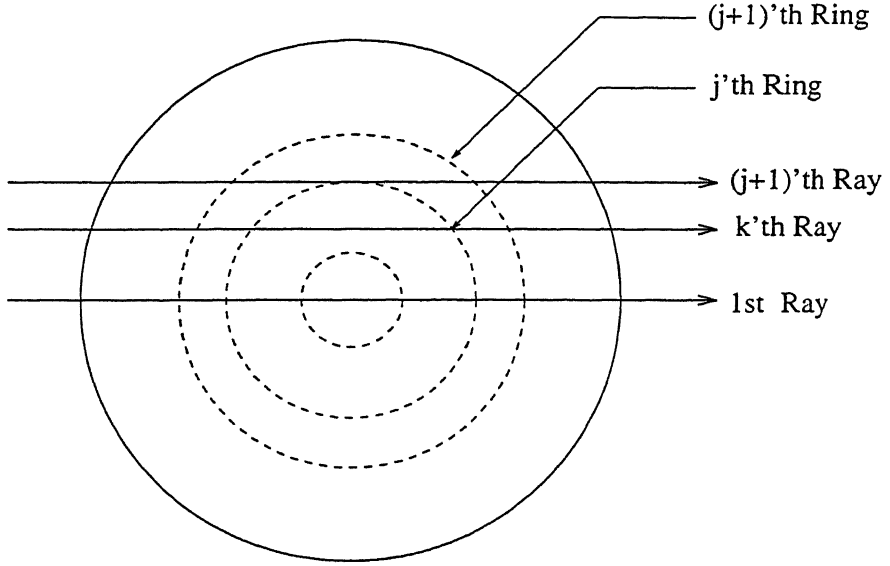
Figure 2.1: B-CSI Data Collection

$$d_k = \int_{C_k} \alpha(r, \phi) ds \qquad (2.3)$$

Clearly,

$$d_k = L_k \times \bar{\alpha}_k \qquad (2.4)$$

We divide the flow cross section into as many number of zones as the rays (chords) and assume that, because of the radial symmetry, the void fraction in any zone j is constant, α_j. The discrete form of Eq. (2.3) can then be written as

$$d_k = \sum_{j=1}^{m} S_{k,j} \alpha_j, \qquad (k = 1, 2, \ldots, m) \qquad (2.5)$$

where,

$S_{k,j}$ = Length of the kth ray passing through the jth zone,

α_j = Average void fraction in the jth zone

m = number of zones (= number of rays)

Equation (2.5) can be rewritten in matrix notation as,

$$[d] = [S][\alpha] \tag{2.6}$$

where,

$$
\begin{aligned}
[d] &= (d_1, d_2, \ldots, d_m) \\
[\alpha] &= (\alpha_1, \alpha_2, \ldots, \alpha_m)
\end{aligned}
$$

and

$$
[S] = \begin{bmatrix}
S_{11} & S_{12} & \cdot & \cdot & \cdot & S_{1m} \\
0 & S_{22} & \cdot & \cdot & \cdot & S_{2m} \\
\cdot & \cdot & \cdot & \cdot & \cdot & \cdot \\
\cdot & \cdot & \cdot & \cdot & \cdot & \cdot \\
\cdot & \cdot & \cdot & \cdot & \cdot & \cdot \\
0 & 0 & \cdot & \cdot & \cdot & S_{mm}
\end{bmatrix}
$$

so that

$$[\alpha] = [S^{-1}][d] \tag{2.7}$$

The cross sectional average is calculated from

$$\langle \alpha \rangle = \frac{\sum_{i=1}^{m} a_i \alpha_i}{A} \tag{2.8}$$

where
a_i = Area of the ith zone and
$A = \sum_{i=1}^{m} a_i$, the total area of the cross section.

ALGORITHM (B-CSI)

1. Read in values into data vector $[d]$ of Eq. (2.6). Calculate the elements by Eq. (2.2) and Eq. (2.4).

2. Calculate matrix S. S_{kj} is the length of the $k'th$ ray passing through the $j'th$ zone.

3. Find the local values of α by Eq. (2.7)

2.3 Least Squares Solution Algorithm

This modification to the CSI algorithm has been recently suggested [21]. Here, the number of zones (n) assumed is less than the number of rays (m). That is, an LSS zone can have more than one ray passing through it. This makes Eq. (2.6) overdetermined. Matrix $[S]$ becomes $m \times n$ where $m > n$. The resulting overdetermined set of equations is solved using least squares criterion through one of the various methods available. The zone diameters and positioning of rays are always chosen such that $[S]$ is never rank-deficient.

2.4 Collapsed-CSI Algorithm

This algorithm, which we abbreviate as C-CSI, is outlined below.

First the void fraction is evaluated in m zones, where m is the number of rays, using the B-CSI algorithm described in Section 2.1. Then the flow area is divided into a fresh set of n C-CSI zones, such that $n < m$. That is, each C-CSI zone is comprised of more than one B-CSI zones. The void fraction in each C-CSI zone is then calculated by area-averaging the values of B-CSI zones which constitute it. This is done as follows.

Consider the kth C-CSI zone shown in Fig. 2.2. (By the kth C-CSI zone, we mean the area between the kth and $(k-1)^{th}$ C-CSI rings.) Starting from the jth, p B-CSI zones are included in this. Then the area-averaged value in the kth C-CSI zone is calculated by,
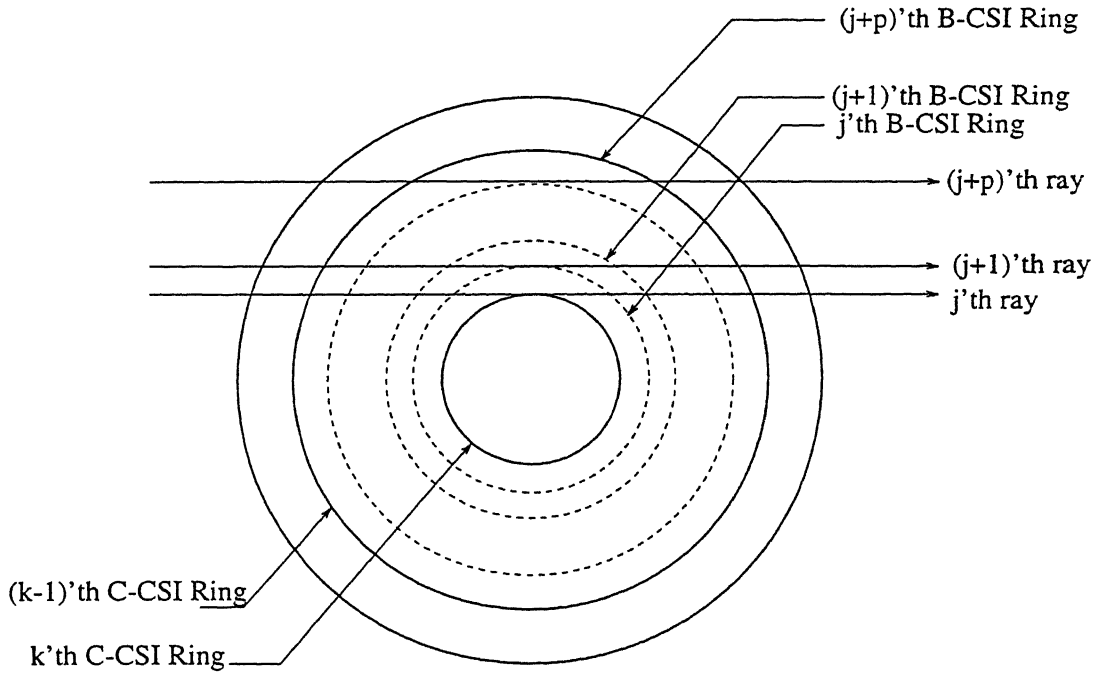
Figure 2.2: Collapsing B-CSI zones into one C-CSI zone

$$\langle \alpha \rangle_k = \frac{\sum_{i=j}^{(j+p)} \alpha_i a_i}{A_k} \qquad (2.9)$$

where

α_i = Void fraction in the ith B-CSI zone.

a_i = Area of the ith B-CSI zone, and,

A_k = Area of the kth C-CSI zone.

Note that the cross sectional average $\langle \alpha \rangle$ calculated by both C-CSI and B-CSI will be the same.

ALGORITHM (C-CSI)

1. Evaluate void fraction in as many zones as the number of rays (m) using the B-CSI algorithm described in Section 2.2.

2. Divide the flow area into n C-CSI zones such that $n < m$.

3. Area-average the B-CSI values within each C-CSI zone using Eq.(2.9).

2.5 Why C-CSI and LSS

It is seen that void fraction profiles reconstructed from actual experimental data using B-CSI exhibit sharp differences between values in adjacent zones, especially when the ray spacing is fine. In this context, we recognise the possibility of errors being present in the data vector $[d]$ of Eq. (2.7). Some of these errors. like those due to Poisson uncertainty, flow fluctuations and instrument instabilities are random in nature. How these errors affect the resulting B-CSI reconstructions have not been comprehensively studied as yet. However. when Poisson noise was numerically incorporated in simulated data (described in Section 4.1.2, Fig. 4.6) the reconstructions have exhibited fluctuations.

When reconstructions are carried out assuming the number of zones to be half the number of rays, (using either C-CSI or LSS) smoother void fraction profiles result. Also, it is found that C-CSI and LSS reconstructions are very similar to each other, in spite of the simiplicity of the former algorithm. Hence, if it is desired to have a smooth void fraction profile from noisy data with closely spaced rays, LSS or C-CSI would be preferred. We may add, however, that LSS & C-CSI solutions are dependent on the corresponding B-CSI solution. This is clearly evident from the simple procedure (described in Section 2.4) of obtaining a C-CSI solution from a B-CSI solution.

It would be unrealistic to consider that all the errors are confined only to the data vector $[d]$. Inaccuracies in finding the centre of the pipe and improper positioning of the rays with regard to the centre will introduce errors in $[S]$. These errors are mainly due to human reasons and, to that extent, minimisable. Should such errors in $[S]$ appear to be substantial, more appropriate methods will have to be sought to solve Eq. (2.7).

Chapter 3

SET-UP, PROCEDURE AND DATA COLLECTION

3.1   Overview

Void fraction profile measurements on mercury-nitrogen two-phase flows,which form the present study, were carried out on the Upcomer of a Liquid Metal Magnetohydrodynamic (LMMHD) system. This experimental LMMHD system is situated at the Laser & Plasma Technology Division of Babha Atomic Research Centre (BARC), Bombay. At an advanced stage of completion, the system will employ steam as the thermodynamic fluid in place of nitrogen on being fully functional. Details of this system are briefly mentioned in Section 1.2. The gamma-densitometer used for measurements existed before this study was undertaken (see Ref. [21]). Hence the detailed design of the densitometer does not appear in this work. The salient features are, however, mentioned in the subsequent sections of this Chapter. A summary of these features appear in Table 3.1. Described below are the flow system, data collected for the study, and precautions adopted against possible errors.

3.2   Flow System

A schematic diagram of the experimental LMMHD setup is shown in Fig. 3.1. Void fraction measurements were carried out at two elevations of the upcomer (U), 1.1 m and 2.8 m above the mixer (M). The upcomer is a 4.06
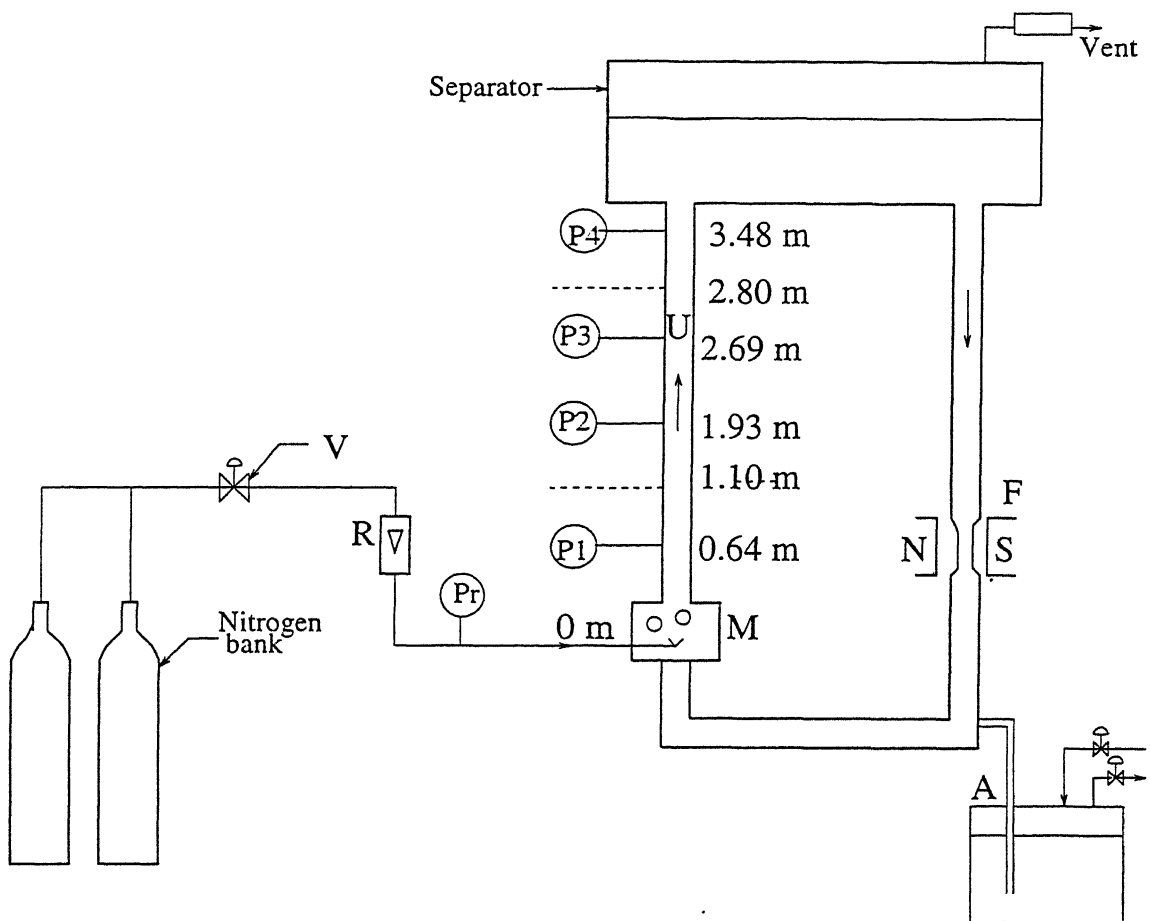
U - Upcomer, M - Mixer, A - Accumulator, F - MHD flow meter, V - Nitrogen inlet Valve R - Rotameter.

Figure 3.1: Flow System

Sl. No.	Item	Details
1.	Pipe	Dimensions – 88.9 mm OD × 77.9 mm ID Material – Stainless steel
2.	Gamma-ray source	Co-60 Strength – 20 mCi
3.	Collimation	By means of 3 mm dia holes in 50 mm tk. lead blocks. Both at source-end & detector-end
4.	Detector	NaI(Tl) Scintillation head.
5.	Signal processing Instrumentation	Operating in count-mode with the SCA set to detect 1.33 MeV. Window = 40 eV
6.	Data collection Geometry	Parallel-beam mode. Ray spacing in scans = 2 mm (min.), 7 mm (max) Farthest chord from centre at 36 mm.

Table 3.1: Densitometer Details

m long stainless steel pipe, 77.9 mm inner diameter and 5.5 mm thick (80NB x sch.40).

The required inventory of mercury is loaded into the system from the accumulator (A). Mercury is circulated in the loop by admitting nitrogen from a bank of cylinders at the bottom the upcomer through the mixer. Fig. 3.2 is a dimensioned sketch of the mixer. Specifications of the flow and pressure measuring devices are included in Appendix D.

3.3   Apparatus and Instrumentation

Figure 3.3 is the top view of the apparatus fabricated to collect data. (P) is the cross section of the upcomer pipe. (B) is a movable table carrying 20 mCi cobalt-60 source (S) and the NaI(Tl) detector (D). It can be moved along rails (R) by operating mechanism (M). The pointer attached to the table against the stationary scale (F), graduated in divisions of 0.5 mm, determine the position of the source with respect to the pipe.

The source is heavily shielded. Gamma rays are collimated both at the source-end and detector-end with 3 mm dia holes in 50 mm thick lead blocks. The detector is covered all around using similar lead blocks to prevent de-

78

225

(N₂Inlet)

A ————— A

Inlet)

60

65

168.3

15 NB x Sch. 40

B

40

B

20 NB x Sch. 40

1.5 mm dia holes
(20 Nos in a row)

A - A

B - B
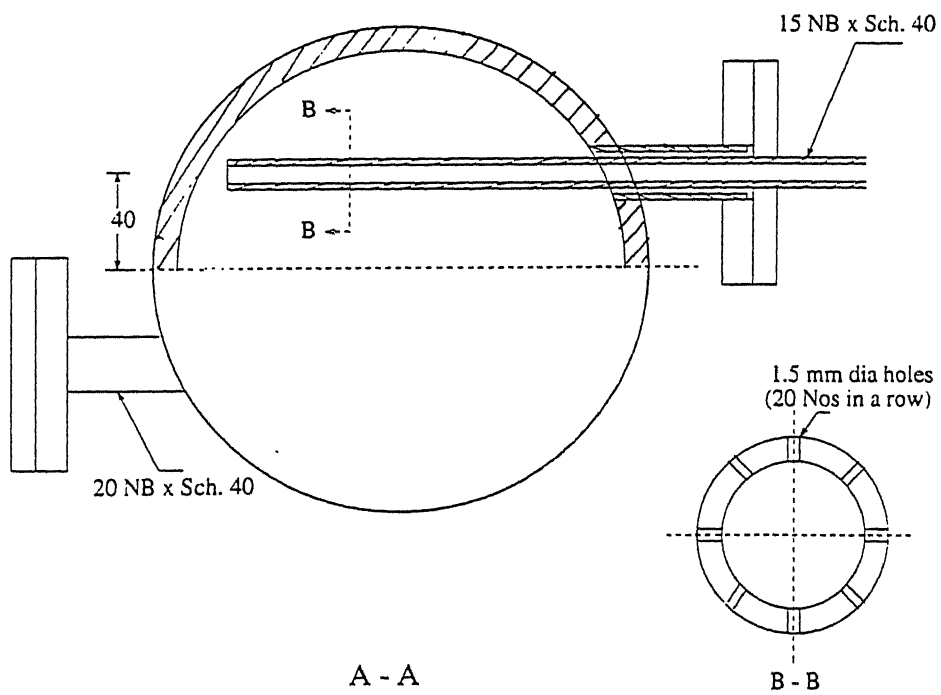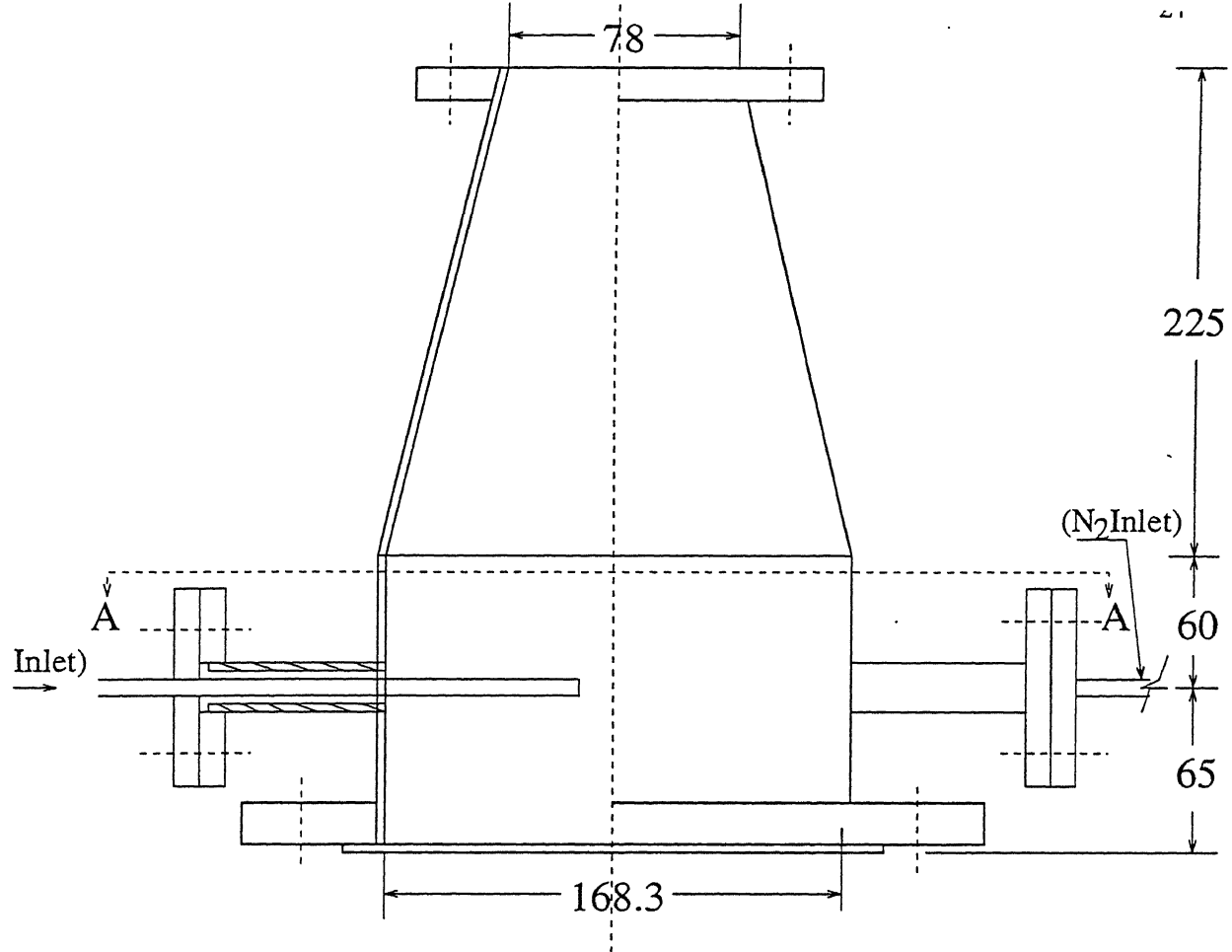
(Dimensions in mm)

Figure 3.2: MIXER
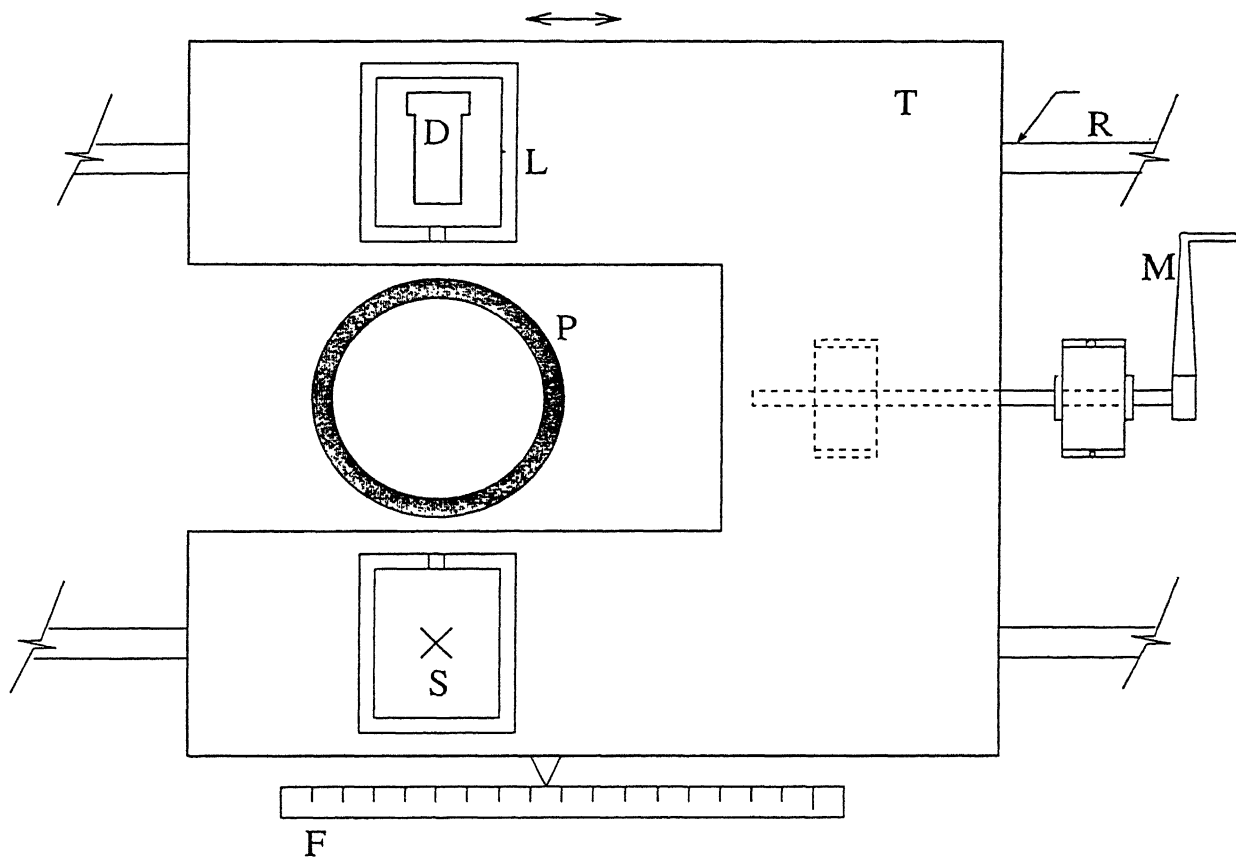
P - Upcomer, T - Table, S - Source, D - Detector, R - Rails, M - Mechanism,
F - Scale.

Figure 3.3: Apparatus
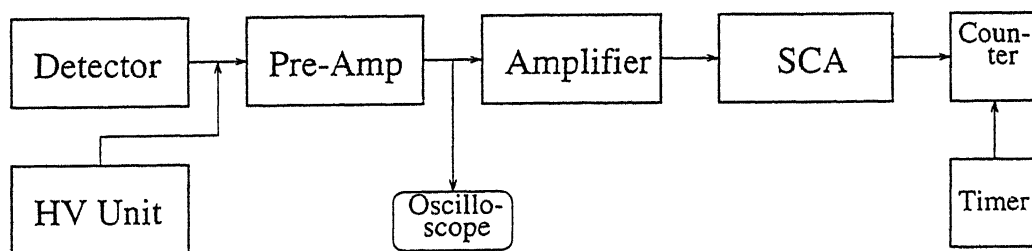
Figure 3.4: Signal Processing Instrumentation

tection of stray and scattered radiaton.

Figure 3.4 is a block diagram showing the detector and associated signal processing instrumentation. The preamplifier of the detection head is connected to the HV and LV units. The output from the preamplifier is connected to a Single Channel Analyser (SCA) through a linear amplifier. The SCA output is connected to the scaler through a timer. Detailed specifications of the units in the signal processisng instrumentation appear in Appendix D.

3.4   What Forms The Data

To determine radial void fraction distribution at a certain plane, length averaged void fractions along a number of parallel chords at different radial distances between the centre and inner periphery of the pipe are to be obtained. These form the input to the algorithms of Chapter 2. The length-averaged void fraction along a chord is calculated using Eq. (2.2). Therefore, through any chord, characterised by its perpendicular distance from the centre of the pipe, three count rates are to be measured with the following media filling the pipe.

1. Nitrogen (or air)

2. Mercury

3. Mercury-nitrogen two phase flow, of a fixed nitrogen flow rate.

We refer to a *reading* as the number of counts observed and the time taken to do so. A set of readings taken along a number of parallel chords from the centre to the inner periphery of the pipe is referred to as a *scan*. For a given nitrogen flow rate, the two phase, mercury and air scans together form the *data* for that flow rate, with the readings of these scans taken along exactly the same chords. That is, the data for two different flow rates at a given plane and half of the pipe differ only in their two-phase flow scans. Data collected in this work is described in a subsequent section.

3.5 Procedure

At first, the 3 mm dia collimating holes at the source and detector ends were aligned. The colimating lead blocks were rigidly fastened to the table so as to keep the alignment undisturbed while the table is in motion. A portable laser beam of 0.5 mm dia was used to ensure that the axes of the holes were indeed collinear, first at start and then occasionally, when the experiment was in progress. The scale reading corresponding to that position of the table at which the (collinear) axes of the collimator holes pass through the centre of the pipe was determined.

To carry out the air scan, the pipe was emptied (that is, filled with air) and the table positioned at the central scale reading. The first reading was taken at the centre, then the table moved by a short distance, the next reading taken, and so on, till the periphery is reached. Repeated at the other half of the pipe also. Similarly the pipe was filled with mercury and carried out the mercury scan.

Next, nitrogen is admitted at the mixer and the flow rate gradually increased by slowly opening valve (V) of Fig. 3.1 . The volume flow rate of nitrogen is measured by the rotameter (R). The pressures at four positions are monitored by the pressure gauges P1 to P4. The pressure upstream the rotatameter is measured by P_r. The mass flow rate of mercury is obtained from the MHD flow meter (M). Detailed specifications of the flow and pressure measuring devices are included in Appendix D.

After attaining the required nitrogen flow rate, waited till all the above system parameters stablised. Then the two phase flow scan was carried out. While the two-phase flow scan was in progress, all the flow and pressure readings were observed at 15 minute intervals.

3.6 Data Collected

The experiment was carried out at two elevations of the upcomer, at 1.1 m (bottom) and 2.8 m (top) above the mixer. At each elevation scanning was done on both (the north & south) halves. The data is presented as 11 major

cases depending on the following.

1. Elevation (Top or Bottom)

2. Half (North or South)

3. Nitrogen Flow Rate (10, 20, 40, 60, 80 litres per minute)

Following the recommendation of Munshi and Vaidya (see Ref. [26]), a minimum of 3000 photon counts were collected for each two-phase and mercury readings. For the air readings this minimum ranged between 7000 and 15,000 for different data sets.

To study the effects of Poisson statistics, the times taken to collect 300, 600, 1000 and 2000 two-phase counts also have been observed in three cases. These form 12 minor cases and have been grouped (with 4 in each group) depending on the major cases from which they originate. That is, the minor cases in any group differ from the corresponding major case only in their two-phase readings. All other parameters remain common.

The names assigned to the 11 major cases, along with the related parameters appear in Table 3.2. The names of the minor cases are listed in groups with their corresponding minimum number of two-phase counts in Table 3.3. Key to the names is given in Fig. 3.5.

Data for all the major cases are presented in Appendix B. Two-phase readings for the minor cases also appear in Appendix B. Each of these, in conjunction with the air and mercury readings of the corresponding major case, form a complete set of data. The flow and pressure gauge readings are given in Table B.1 of Appendix B.

Major Case Name	Nitrogen Flow rate (lpm)	Elevation	Half	Number of readings per scan
BN400	40	Bottom	North	10
BS400	40	Bottom	South	19
BN600	60	Bottom	North	19
BS600	60	Bottom	South	19
TN400	40	Top	North	10
TS400	40	Top	South	19
TN600	60	Top	North	10
TS600	60	Top	South	10
TS800	80	Top	South	6
TS200	20	Top	South	6
TS100	10	Top	South	6

Table 3.2: Parameters for Major Case Data-sets

Major Case	Minimum No. of Two-Phase Counts			
	300	600	1000	2000
BS600	BS603	BS606	BS601	BS602
TN400	TN403	TN406	TN401	TN402
TS400	TS403	TS406	TS401	TS402

Table 3.3: Minor Case Data-set groupings

BS400

Minimum
Two-Phase Counts
0 - 3000, 1 - 1000, 2 - 2000
3 - 300, 6 - 600

N_2 flow rate
10 - 10 lpm, 20 - 20 lpm,
40 - 40 lpm, 60 - 60 lpm
80 - 80 lpm

Half
S - South, N - North

Elevation
B - Bottom   T - Top
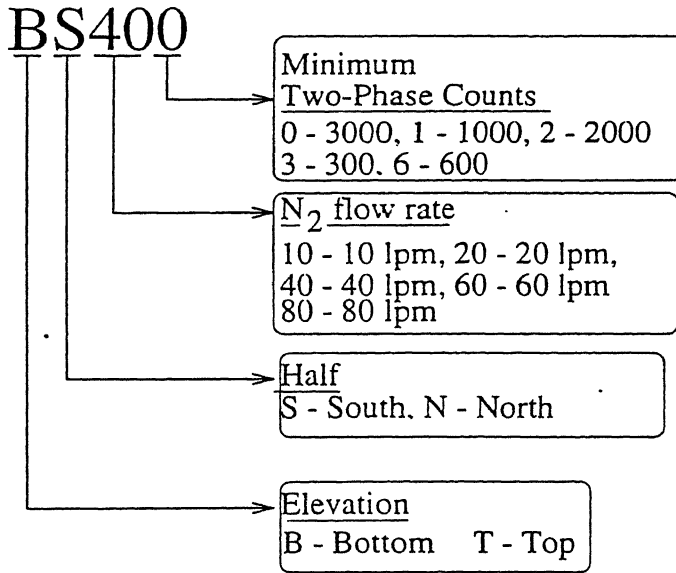
Figure 3.5: Key to Data Set Names

3.7 Precautions against errors

In view of the many reasons likely to cause errors, several steps had to be adopted during the design of the gamma-ray densitometer and during the process of data collection. These are detailed below.

Poisson Uncertainty The minimum number of photon counts collected for each reading was maintained at 3000. This, and the high linear attenuation coefficient of mercury, ensure that the uncertainties in the reconstructed local vlaues remains negligibly small. See Section 4.1.2 for a detailed discussion.

Dynamic Bias Error The only possible step to reduce the dynamic bias error in a long-duration radiation attenuation measurement is to minimise the pathlength of the ray through the flow medium, λ. (See Eq. (4.10), where $\lambda_{max} = \mu_l \times L_{max}$). The diameter of the pipe is fixed at 77.9 mm on considerations of LMMHD design. In order to minimise λ_{max}, the remaining option is to select a high energy source to provide a low value of μ_l. Hence the selection of Co-60 as the gamma ray source. We recognise that even at 1.33 MeV, $\mu_l = 0.78$ cm^{-1} giving a high value of $\lambda_{max} = 6.1$. See Section 4.2 for a further discussion of these aspects.

Alignment Proper alignment between the source and detector axes was of foremost concern during the data collection. At the start and end of every scan, this alignment was checked using a portable laser beam of 0.5 mm dia. This still does not ensure whether the alignment is retained while moving the table for scanning the pipe. Note, however, that the value of unobstructed counts does not appear explicitly in Equation(2.2). The unobstructed counts for various scans are only expected to be *equal* at a given position of the table. This can be accomplished even in the event of minor misalignments as long as these are systematic. Any random misalignments will be large enough to alert the experimenter through a sudden and large fall in the counts being observed.

Instrument instabilities The signal processing sytem used is adequately equipped to minimise the effects due to input voltage fluctuations. Also, the low count rates make it possible to operate the system in count-mode in which these voltage fluctuations have a less significant effect. However, to ensure that the system remains indeed stable during the experiments, the following procedure was adopted. At every 15 minutes, the source-detector axis was moved away from the pipe and the unobstructed counts were observed. Differences between these successive observations were within the Posisson uncertainty. In the few instances when higher differences were observed, the base voltage of the SCA was adjusted by $\pm 0.1V$ and the experiment repeated.

Flow instabilities Transients are to expected during long duration experiments on a complex natural circulation loop as the present one. Variation in the nitrogen flow-rate was recognised as the parameter likely to cause flow instabilities. Hence the reading at the Rotameter (R) (see Fig. 3.1) was constantly monitored while the expriment was in progress. The float oscillated within $\pm$ 0.2 lpm around the specified flow rate. The experiment was begun only after the system stabilised and the above criterion was achieved.

Chapter 4

ERROR IN RECONSTRUCTIONS

Among the different errors likely to affect any tomographic measurement, of particular importance to the present work are those due Poisson statitics and dynamic bias. Procedures to find the effects of these two errors on reconstructions are discussed in this chapter. Simulated data generated from an assumed distribution in a hypothetical mercury-nitrogen flow, through a geometry similar to that of the present work, is used to illustrate the trends and magnitudes of these errors. Errors resulting from the improper positioning of the rays with respect to the object being scanned are also discussed.

4.1 Statistical Uncertainty

The data obtained from a radiation attenuation measurement is associated with statistical uncertainties due to the random nature of radioactive decay. The parameters calculated from such data have, therefore, these uncertainties carried over to them. Suppose we are calculating a quantity u which is a function of measured values $x, y, z, \ldots$ such that $u = f(x, y, z, \ldots)$. Let each of the measured values $x, y, z, \ldots$ have associated uncertainties, expressed in terms of their standard deviations $\sigma_x, \sigma_y, \sigma_z, \ldots$ If the fluctuations in the measured values are small and uncorrelated, the variance of the desired quantity u is given by (see for eg., Ref. [42]),

$$\sigma_u^2 = \left(\frac{\partial u}{\partial x}\right)^2 \sigma_x^2 + \left(\frac{\partial u}{\partial y}\right)^2 \sigma_y^2 + \left(\frac{\partial u}{\partial z}\right)^2 \sigma_z^2 \qquad (4.1)$$

The assumptions of Eq. (4.1) hold good for many cases of nuclear measurements (see Ref. [43]) and here we apply it to evaluate the statistical error in the chord-averaged and reconstructed values of void fraction.

4.1.1 Statistical error in chord-averaged Void fraction

The chord-averaged void fractions which constitute the input to further tomograhic algorithms, are calculated using Eq. (2.2) and is repeated below.

$$\bar{\alpha} = \frac{\ln(I_{tp}/I_l)}{\ln(I_g/I_l)} \qquad (4.2)$$

where,

$$
\begin{aligned}
I_{tp} &= N_{tp}/t_{tp} \\
I_l &= N_l/t_l \\
I_g &= N_g/t_g
\end{aligned}
$$

and N_l, N_g & N_{tp} are the gamma counts observed along the same chord with liquid, gas and two-phase filling the pipe respectively. t_l, t_g and t_{tp} are the times (s) in which the counts N_l, N_g and N_{tp} are collected.

If, during a single measurement N counts are observed, with $(1-\sigma)$ confidence, the true mean of the (Poisson) distribution lies between $(N - \sqrt{N})$ and $(N + \sqrt{N})$. That is, the $(1-\sigma)$ error in the measurement of N is $\sqrt{N}$.

Considering the above and assuming that there is no error in the measurement of times t_l, t_g and t_{tp} the $(1-\sigma)$ error of $\bar{\alpha}$ can be expressed as,

$$\Delta\bar{\alpha}_s = \frac{1}{\ln(I_g/I_l)}\left[\frac{1}{N_{tp}} + \frac{(\bar{\alpha}-1)^2}{N_l} + \frac{\bar{\alpha}^2}{N_g}\right]^{1/2} \qquad (4.3)$$

Equation (4.3) is derived in Appendix A.
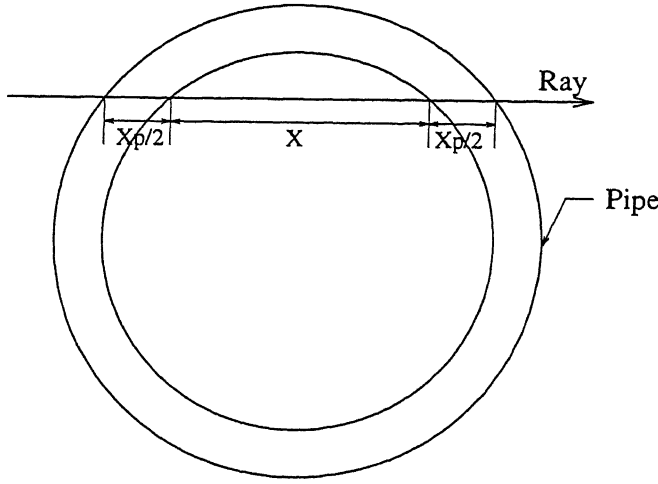
Figure 4.1: Ray passing through pipe

Illustration–1

Consider a stainless steel pipe of 78.9 mm inner diameter and 5.5 mm thickness through which a two-phase mercury-nitrogen flow takes place. Linear attenuation coefficient of mercury is taken as 0.78 cm^{-1} (Ref. [44]). The (1-σ) statistical error in chord-averaged void fractions for the full range $0 \leq \bar{\alpha} \leq 1$ is calculated using Eq. (4.3). All these calculations were done with $N_g = 12000$ and $N_l = 3000$. The number of two-phase counts for each case are mentioned in the corresponding plot (Figs. 4.2 & 4.3).

Figure 4.2 shows the error $\bar{\alpha}_s$ as a function of $\bar{\alpha}$ for three positions of the chords. Expectedly, the error increases as the chord moves away from the centre. But its variation with $\bar{\alpha}$ is not considerable.

To study the effect of the number of counts of the constant count experiment, we select the chord farthest from the centre (the worst case). In Fig. 4.3 $\Delta\bar{\alpha}$ is plotted for a chord 0.87R units away from the centre for three values of N_{tp}. The error increases with lower values of N_{tp}. The almost constant error of 0.025 obtained for $N_{tp} = 300$ is high, especially for lower values of $\bar{\alpha}$.

To make the effects of some parameters on $\Delta\bar{\alpha}$ explicit, we expand the first term of Eq. (4.3) as follows. (See Fig. 4.1) μ_l, μ_l and μ_g are the

linear attenuation coefficients (cm^{-1}) of the pipe-material, liquid and gas that comprise the two-phase flow. Then,

$$
\begin{aligned}
I_g &= I_0 e^{-(\mu_p x_p + \mu_g x)} \\
&\approx I_0 e^{-(\mu_p x_p)} \qquad (\mu_g \approx 0) \\
I_l &= I_0 e^{-(\mu_p x_p + \mu_l x)}
\end{aligned}
$$

Hence,

$$
\frac{1}{\ln(I_g/I_l)} = \frac{1}{x\mu_l} \tag{4.4}
$$

That is, in a constant-count experiment, for a given void fraction the statistical error is inversely proportional to the length of the ray (chord) inside the pipe and the linear attenuation coeffient of the liquid.

4.1.2 Statistical Error in Local Void fractions Reconstructed with B-CSI

The B-CSI algorithm is derived in section 2.2. The unknown void fraction in each of the m zones is evaluated by Eq. (2.7) which is repeated here.

$$
[\alpha] = S^{-1} \mathbf{d} \tag{4.5}
$$

where,

$$
d_i = L_i \times \bar{\alpha}_i
$$

L_i = Length of the ith chord passing through the flow area.

Using Eq. (4.3) we can evaluate the statistical errors, $\sigma_{\bar{\alpha}i}$, in each chord-averaged value, $\bar{\alpha}_i$. We also assume that there are no errors associated with the elements of $[S]$ and the lengths L_i, though this need not be strictly true. Applying the error propogation formula (4.1) to each equation in (4.5), we can thus calculate the (1-σ) standard deviations of the elements of $[\alpha]$. This results in (see Appendix A),
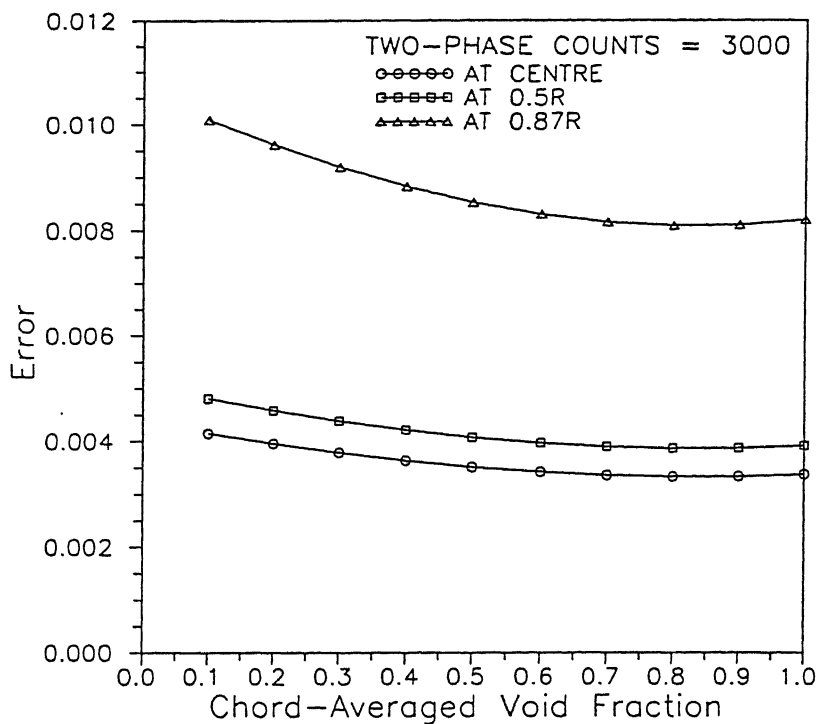
Figure 4.2: Absolute statistical error in chord-averaged values, $\Delta\bar{\alpha}_s$, for different chordal positions. ($N_g = 12000, N_l = 3000 \& N_{tp} = 3000$)
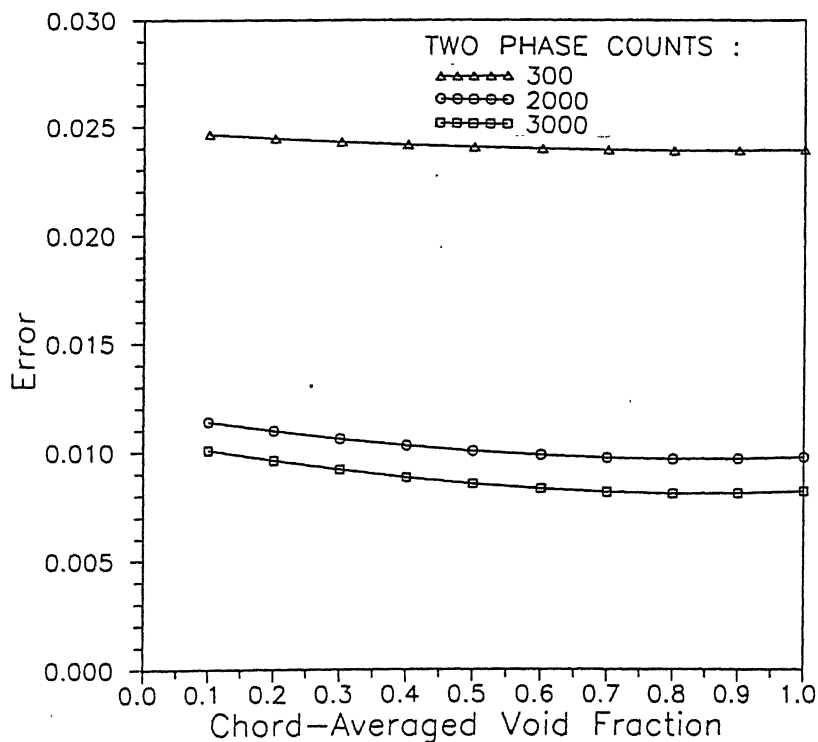
Figure 4.3: Absolute statistical error in chord-averaged values, $\Delta\bar{\alpha}_s$, for different two-phase counts at the chordal position 0.87R. ($N_g = 12000 \& N_l = 3000$)

$$\sigma_{\alpha k} = \frac{1}{S_{kk}} \left(L_k^2 \sigma_{\bar{\alpha}k}^2 + \sum_{j=k+1}^{m} S_{kj}^2 \sigma_{\alpha j}^2 \right)^{1/2} \qquad (4.6)$$

For $k = m$, since $L_m = S_{mm}$

$$\sigma_{\alpha m} = \sigma_{\bar{\alpha}m},$$

where,

$\sigma_{\alpha k}$ = (1-σ) uncertainty in the the local value calculated in the k'th zone.

$\sigma_{\bar{\alpha}k}$ = (1-σ) uncertainty of length-averaged value at the k'th chord.

and,

m = Number of rays = Number of zones.

Illustration–2

To illustrate the use of Eq. (4.6) in estimating (1-σ) errors in a reconstructed void fraction profile, we consider a mercury-nitrogen two phase flow in stainless steel pipe of inner diameter (2R) = 78.9 mm and 5.5 mm thickness. A typical void fraction distribution of $\alpha(r) = 0.4 \cos\left(\frac{\pi r}{2R}\right)$ is assumed in this flow. Simulated data, conforming to the actual data of this work, is calculated for this system. 19 rays starting from the centre and with a step size of 2 mm are considered. For all the cases the mercury counts were fixed at 3000 and the nitrogen counts at 12000. The two-phase counts are as mentioned in each illustration.

Figure 4.4 plots the absolute errors in the reconstruction for various (constant) values of two-phase counts. That is, the counts collected at various chordal positions in a single scan are held constant, and we are estimating the errors for different scans. For the distribution considered, the error is highest at the centre. However, even the maximum, occuring for the lowest of the constant counts (1000), is only 0.06. The percentage error (see Fig.4.5) increases sharply towards the wall, but this is due to the low values of the cosine void-fraction distribution considered.

Our interest in the errors of experiments of different constant-counts is due to obvious reasons. While it is expected that larger the counts, smaller the errors, this requires either a *stronger* (and more hazardous) source or *larger* data collection times. Apart from the economics, a longer data collection time invites further errors due to increased instrument instabilities which can be substantial.

The validity of the (1-σ) errors predicted by Eq. (4.6) was checked by the following procedure. To each count N of the simulated data, random numbers between $-\sqrt{N}$ and $+\sqrt{N}$ were added to recreate the (1-σ) Poisson fluctuations. The reconstructions obtained from 2 such sets of corrupted data is shown in Fig. (4.6). The fluctuations are more towards the centre, and largely within the predicted values.
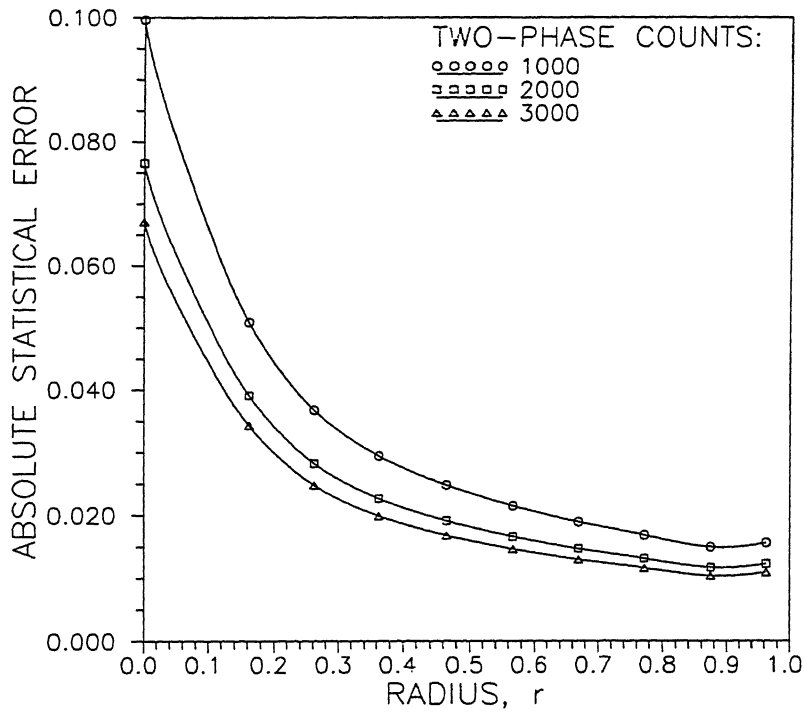
Figure 4.4: Absolute statistical error in local values, $\sigma_{\alpha(r)}$, in the reconstruction of assumed profile $0.4 \cos \frac{\pi r}{2R}$ for different N_{tp}. ($N_g = 12000 \& N_l = 3000$)
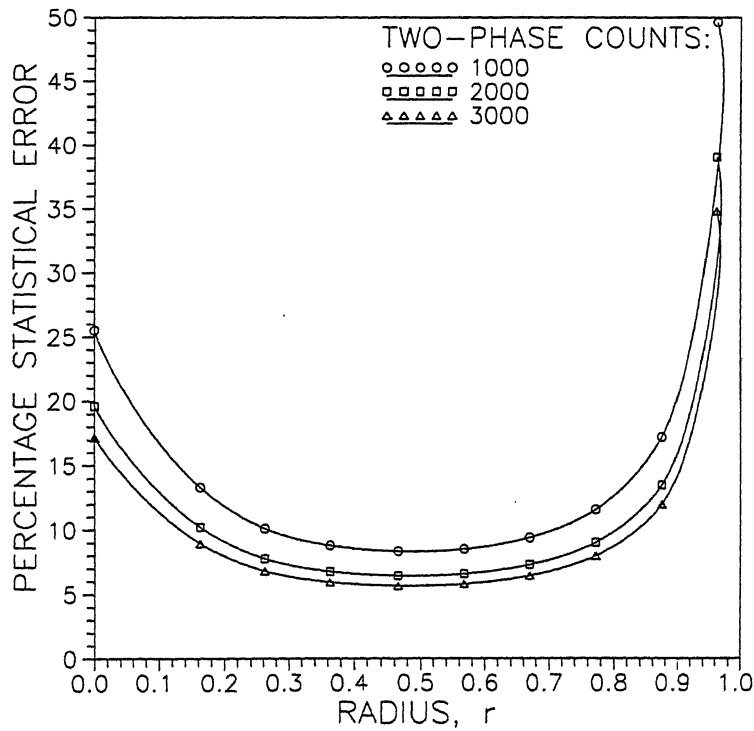
Figure 4.5:

Percentage statistical error in local values, $\frac{\sigma_{\alpha(r)} \times 100}{\alpha(r)}$, in the reconstruction of assumed profile $0.4 \cos \frac{\pi r}{2R}$ for different N_{tp}. ($N_g = 12000 \& N_l = 3000$)
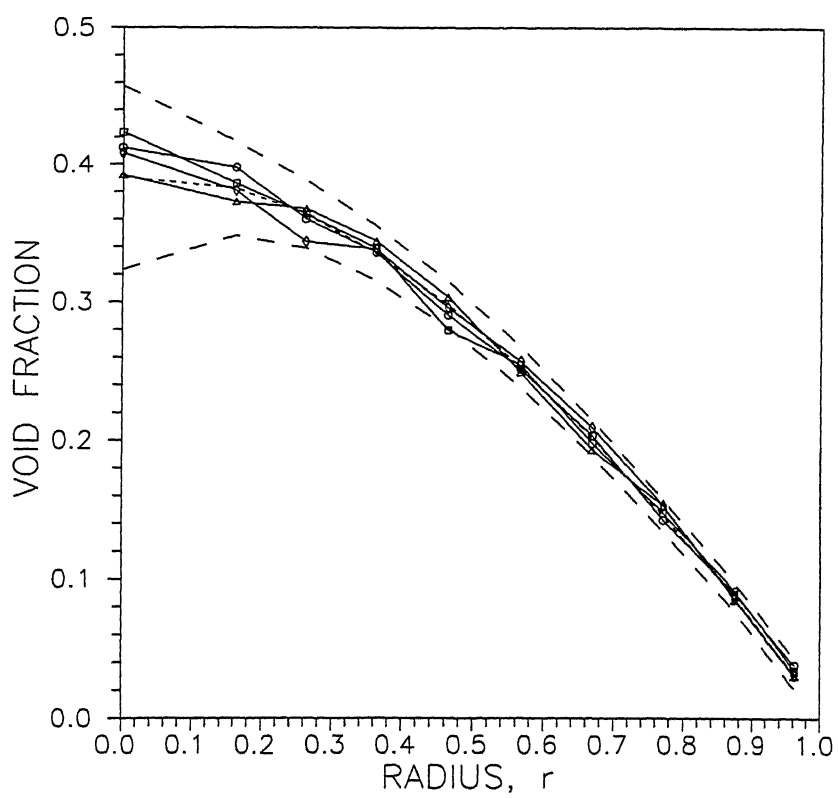
Figure 4.6:

Reconstructions of the assumed profile $0.4\cos\frac{\pi r}{2R}$ from simulated data corrupted with $(1\text{-}\sigma)$ statistical noise, along with error predicted by Eq. (4.6).

4.2 Dynamic Bias Error

Chord-averaged, time averaged void fractions in this work are measured by means of time-integrated counts obtained over a long period of time. But voids along the path of the beam are varying in very short time periods and such fluctuations result in increased transmittance compared to that through a constant void fraction. Harms & Laratta [27] have expressed this dynamic bias error in terms of the instantaneous chord-averaged void fraction $\bar{\alpha}(t)$.

$$
\begin{aligned}
\Delta\hat{\alpha}_d &= \frac{1}{\lambda}\ln\left(\frac{1}{\tau}\int_0^\tau e^{\lambda\bar{\alpha}(t)}dt\right) - \frac{1}{\tau}\int_0^\tau \bar{\alpha}(t)dt \qquad (4.7)\\
&= \hat{\alpha}_m - \hat{\alpha}_a
\end{aligned}
$$

where,

$\lambda = \mu_l L$

$L = $ Length of the beam in the flow area.

$\tau = $ Measurement time.

$\hat{\alpha}_m = $ measured chord and time averaged value under the assumption of constant void fraction

and,

$\hat{\alpha}_a = $ actual chord and time averaged value.

Hence, to estimate the dynamic bias error the variation of $\alpha(\bar{t})$ should be known. In the absence of such information in mercury-nitrogen flows, we follow the approach of Thiagarajan et. al. [45] to develop a conservative error estimate. The results of statistical measurements made by Jones & Zuber [31] and Vince & Lahey [32], though in air-water flows, are also utilized.

First we discretise Eq. (4.7) in the following way. Suppose the time over which the experiment is performed is split into a series of equal time intervals, Δt. Δt is sufficiently small, so that $\bar{\alpha}(t)$ may be assumed to be a constant

in it. We designate the chord-integrated value in the ith time interval as α_i . N number of measurements are made in time τ and hence,

$$\tau = N\Delta t$$

$$\hat{\alpha_m} = \frac{1}{\lambda}\ln\left(\frac{1}{N}\sum_{i=1}^{N}e^{\lambda\bar{\alpha_i}}\right) \tag{4.8}$$

$$\hat{\alpha_a} = \frac{1}{N}\sum_{i=1}^{N}\alpha_i \tag{4.9}$$

and the dynamic bias error

$$\Delta\hat{\alpha}_d = \hat{\alpha_m} - \hat{\alpha_a}$$

The magnitude of the dynamic bias error increases with the path length λ and the scatter in the values of $\bar{\alpha}(t)$ about its mean $\hat{\alpha}$. This is made explicit by alternately expressing Eq.(4.7) as follows (see Ref.[28]).

$$\Delta\hat{\alpha}_d = \frac{1}{\lambda}\ln\left[1 + \sum_{n=2}^{\infty}\frac{\lambda^n}{n!}\frac{1}{\tau}\int_0^{\tau}(\bar{\alpha}(t) - \hat{\alpha})^n\,dt\right]$$

$$= \frac{1}{\lambda}\ln\left[1 + \text{higher moments of }(\bar{\alpha}(t) - \hat{\alpha})\right] \tag{4.10}$$

The dynamic bias error is strongly dependent on the variance and higher moments of the probability distribution of the instantaneous void fractions. In view of this, the following observations from Jones & Zuber [31] and Vince & Lahey [32] are relevant to us.

Jones & Zuber [31] carried out measurements of instantaneous void fractions in vertical air-water flows through a rectangular channel by x-ray attenuation. The PDFs of instantaneous void fractions, $\bar{\alpha}(t)$, were found to be characteristic of the flow regime . Bubbly flow is characterised by a single low void peak. Slug flow has two peaks, one at high void and other at low void. Annular flow produces a single peak at high void fraction.

Vince and Lahey [32] repeated the above experiment with improved equipments on a vertical air-water flow through a cylindrical pipe. The PDFs observed were largely similar to that of Ref. [31] though sharp peaks were observed at the limiting values of $\hat{\alpha}$ for bubbly and annular flows. Also, PDFs obtained at 6 chordal positions were found to be similar

to each other. The variance of the PDFs change with the flow regime. For a *zero superficial liquid velocity*, the variance first increased with $\hat{\alpha}_a$, reached a maximum (of ≈ 0.16 at $\hat{\alpha}_a = 0.5$), and thereafterwards decreased to low values (See Fig. 4.7). The transition to and from slug flow is characterised by a variance of 0.04. The maximum variance occurred at fully developed slug flows.

If PDFs of $\bar{\alpha}(t)$, are simulated for the range $0 < \hat{\alpha} < 1$, such that the variances of these PDFs follow the trend of Fig. 4.7, we may develop an estimate for the dynamic bias error for the present mercury-nitrogen flow using Eqs. (4.8) and (4.9). Hence the following procedure is adopted.

PROCEDURE

1. Generate a large number of random numbers $\bar{\alpha}_i$ normally distributed about mean m_0, with a large standard deviation of 0.5.

2. Set
$\bar{\alpha}_i = 0$ if $\bar{\alpha}_i < 0$
$\bar{\alpha}_i = 1$ if $\bar{\alpha}_i > 1$

3. Calculate the mean of the distribution so obtained by Eq.(4.9). This is the true time averaged void fraction, $\hat{\alpha}_a$. Calculate the variance for comparison with Fig. 4.7.

4. Calculate $\hat{\alpha_m}$ with L = Inner dia of the pipe. Evaluate the dynamic bias error.

5. Change m_0 by small values, each time repeating steps 1–4, till the entire range of $0 \le \hat{\alpha}_a \le 1$ is covered.

6. Repeat 1–5, each time decreasing L for different chord positions till the periphery of the pipe is reached.

Figure 4.8 expresses the variance of the PDFs at each $\hat{\alpha}$ as a function of $\hat{\alpha}$. Figure 4.9 plots the estimated dynamic bias error for the range of $0 \le \hat{\alpha}_a \le 1.0$.

Note that similarity has been assumed between air-water and mercury-nitrogen flows. Also, at liquid velocities higher than zero, while the variance continues to predict the flow regime, a given variance can occur at a value of $\hat{\alpha}$ different from that of Fig. 4.7.

The error estimate in Fig. 4.9 should then be viewed as a first approximation and is not being applied to the data collected in the present work.

4.3 Geometry Related Errors

These are errors arising out of the differences between data collection geometries assumed in the calculations and actually maintained in the course of the experiment. An error in the determination of the centre of the pipe can result in all the rays of a scan being displaced from the positions required in the algorithm. The plane of rays can also get shifted from the horizontal erroneously. But in the present set-up this would have caused a misalignment of the source and detector axes, alerting the experimenter through a drastic fall in the detected counts. These geometry related errors are reflected in the elements of matrix $[S]$ of the CSI equation (2.6). In this section a qualitative estimation of the errors due to inaccurate positioning of the rays is attempted.

The inputs to calculate the matrix $[S]$ are,

1. Diameters of the object and assumed zones.

2. Perpendicular distances from the centre to the rays.

For set-up used in the present study the scale determining the position of the source-detector axis with respect to the pipe was graduated in 0.5 mm. Hence we assume the errors in input (2) above to be of the order of 0.5 mm. Simulated data was obtained for a void fraction distribution of $0.4 \cos \frac{\pi r}{2R}$ for the system described in Section 3.2 . The position of the i'th ray from centre was taken to be $Xi + \delta x$, where $\delta x = \pm 0.5$ mm. This data was then used to reconstruct the profile using LSS and B-CSI. While reconstructing, the rays were assigned to positions X_i.
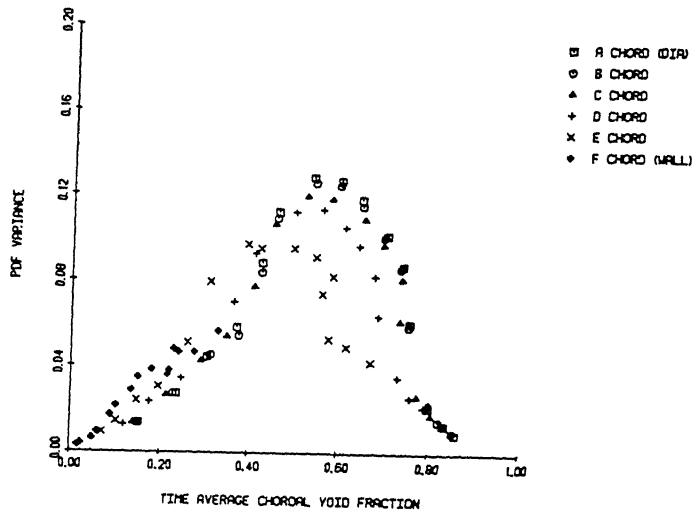
Figure 4.7: The PDF variance vs time averaged chordal void fraction for zero liquid superficial velocity.
(from Ref. [32])
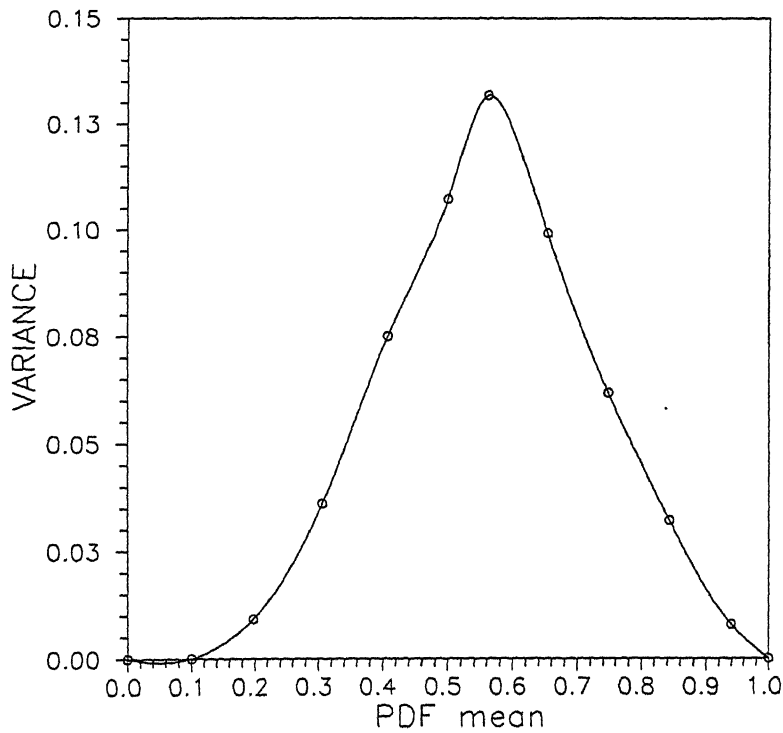
Figure 4.8: Variance of $\bar{\alpha}(t)$ as a function of $\hat{\alpha}_a$
(for the simulation procedure of Section 4.2)

Figures 4.10 and 4.11 show the errors in B-CSI and LSS profiles due to a shift of ± 0.5 mm. By a positive shift, we mean a shift towards the half that was scanned and vice versa.

From the LSS profiles it is clear that the ordinary least squares solution of the overdetermined system does not help to get the desired fit when errors are present in the matrix S. Also, the effects of a finite width of the beam have not been considered here.
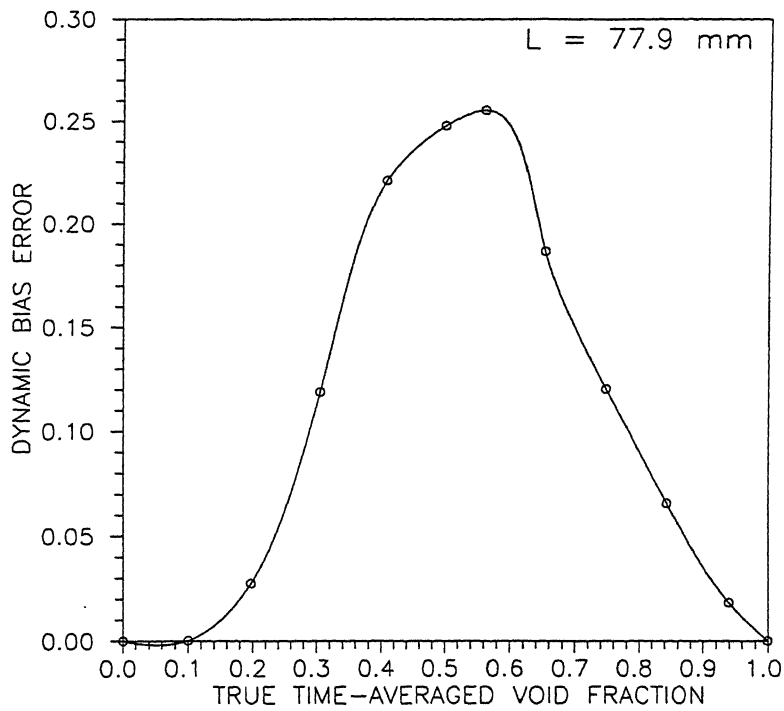
Figure 4.9: Dynamic bias error,$\Delta\hat{\alpha}_d$.
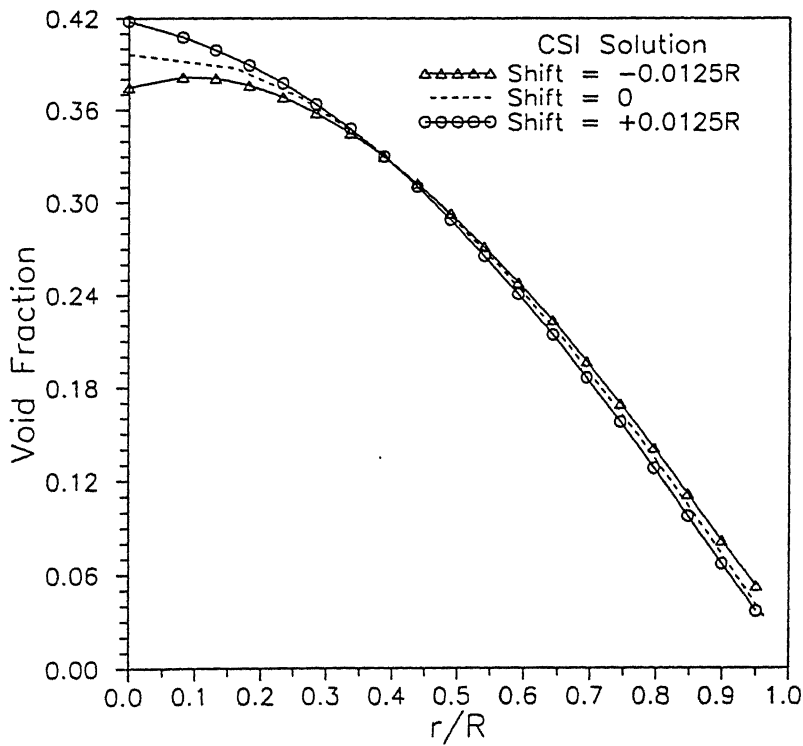
Figure 4.10: Difference in B-CSI reconstructions due to inaccurate positioning of rays with respect to the object. (Assumed distribution, $0.4\cos\frac{\pi r}{2R}$)
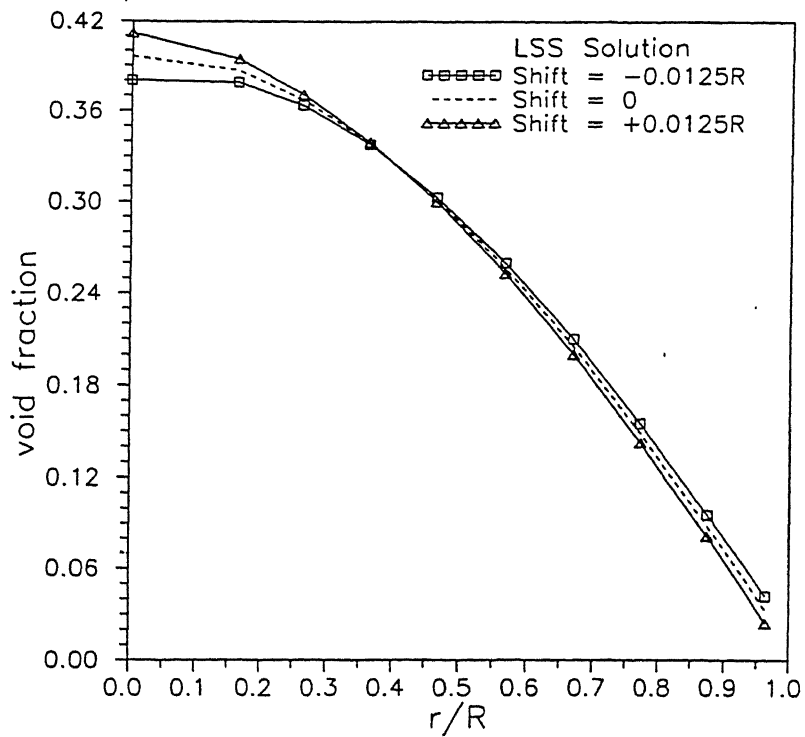
Figure 4.11: Difference in LSS reconstructions due to inaccurate positioning of rays with respect to the object. (Assumed distribution, $0.4\cos\frac{\pi r}{2R}$)

Chapter 5

RESULTS

5.1 General Considerations

The data collected for the present work is described in Chapter 3. Void fraction distribution for each data case has been reconstructed using the algorithms B-CSI, C-CSI and LSS. Fortran programs were written to implement these algorithms.

The geometry matrix [S] for B-CSI being triangular, the inversion was done through a simple backsubstitution. The least squares inversion has been done after forming normal equations and solving them using Cholesky decomposition. The computer program for this was adapted from the book by R. L. Branham Jr. [46] . The results so obtained were identical to those from a standard subroutine of NAG library which uses orthogonal transformations for the inversion.

Detailed presentation of all the results is described in the following Section. In all the graphs of $\alpha(r)$ vs r plotted, the void fraction for a given zone (except for the central and outermost zones) is assigned to that radius r_{0i} which divides the zone into two equal areas. That is,

$$r_{0i} = \sqrt{\frac{r_{i+1}^2 + r_i^2}{2}} \qquad (5.1)$$

where,

r_{i+1} = Outer radius of the i_{th} zone

$r_i = $ Inner radius   and

$n = $ Total number of zones.

Void fractions of the first and last zones are assined to radii, $r_{i0} = 0$ and $r_{0n} = $ Inner radius of the pipe, respectively. The points are joined by straight lines. No further attempt has been made to smoothen the curves so as to preserve the characteristics of each tomographic solution.

5.2 Presentation of Results

5.2.1 Major Cases

The air, mercury & two-phase count rates and chord-averaged void fractions for the 11 Major Cases of data appear in Tables C.1 to C.31 of Appendix C. The void fraction distributions for each Major Case have been calculated by the following algorithms.

B-CSI (No. of zones = No. of rays)

LSS (No. of zones $\leq$ No. of rays/2)

C-CSI (as in LSS)

A summary of the results appear in Table 5.1. The presentation of detailed results calculated by each algorithm is described below.

B-CSI Results

The Basic-CSI algorithm (abbreviated as B-CSI) for parallel-beam geometry is described in Chapter 2. Here the number zones assumed is equal to the number of rays from centre to the inner periphery of the pipe. The reconstructed zonal void fractions for all the Major Cases are tabulated in Tables C.2 to C.32 of Appendix C. 1-σ statistical uncertainites calculated by Eq.(4.6) also appear in these tables. The dynamic bias error has not been estimated because of the reasons cited in Chapter 4. Plots of $\alpha(r)$ vs r appear in this Chapter as Figs. 5.1 to 5.11.

Table 5.1: Summary of results

Major Case Name	Number of rays per scan	Mercury flow rate (kg/s)	Nitrogen flow rate $\times 10^{-3}$ (kg/s)	Cross sectionally averaged void fraction, $\langle \alpha \rangle$ B-CSI & C-CSI	LSS
BN400	10	28.9	4.68	0.1868	0.1886
BS400	19	28.9	4.68	0.1731	0.1730
BN600	19	29.4	6.81	0.2593	0.2599
BS600	19	29.4	6.81	0.2426	0.2424
TN400	10	27.2	4.67	0.2947	0.2952
TS400	19	27.2	4.67	0.2505	0.2507
TN600	10	27.9	7.06	0.3751	0.3757
TS600	10	27.9	7.06	0.3355	0.3360
TS800	6	34.1	8.84	0.3872	0.3878
TS200	6	20.8	2.43	0.1640	0.1643
TS100	6	17.6	1.23	0.1050	0.1053

LSS Results

The Least Squares Solution Algorithm (LSS) which is an overdetermined version of B-CSI is described in Chapter 2. The linear system of equations of the CSI direct problem Eq.(2.6) is made overdetermined by assuming the number of zones to be lesser than the number of rays. In general, we assign the LSS zones such that at least two rays pass through them. The selection of the number of zones and their radii for the various data cases are done in the following way.

- For data cases with 19 rays (ray spacing = 2 mm), 9 zones of outer radii 4, 8, 12, 16, 20, 24, 28, 32 & 38.95 mm are selected. Note that three rays pass through the outer most zone.

- For Cases with 10 rays (ray spacing = 4 mm), 5 zones of outer radii 8, 16, 24, 32 & 38.95 mm are selected.

- For Cases with 6 rays (ray spacing = 7 mm), 3 zones of outer radii 14, 28 & 38.95 mm are selected.

Void fraction distributions reconstructed with LSS are tabulated in Tables C.3 to C.33 of Appendix C. $\alpha(r)$ vs r plots are included in this Chapter as Figs. 5.12 to 5.22.

C-CSI Results

In this locally collapsed version of B-CSI, the number of zones is assumed to be less than the number of rays. For the present reconstructions, the C-CSI zones have been selected to be the same as that of the LSS zones. The void fractions in a given C-CSI zone is the area average of the values of the B-CSI zones comprising it. The objective of these reconstructions is to provide a comparison with the corresponding LSS values. Hence the plots of $\alpha(r)$ Vs r are superimposed with LSS solutions in Figs.5.23 to 5.33.

5.2.2 Minor Cases

Void fraction distributions of the Minor Cases are done only with LSS. The objective being to provide a comparison between reconstructions of different constant-counts, the local void fractions have not been tabulated and only the plots of $\alpha(r)$ vs r are shown in Figs. 5.34 , 5.35 & 5.36.

5.3 Discussion

5.3.1 Cross sectionally Averaged Void Fraction

The expected behaviour of the LMMHD natural circulation loop is well reflected in the experimentally determined area-averaged void fractions, $\langle \alpha \rangle$. The void fraction at a given elevation increases with the nitrogen flow-rate and with the distance from the mixer.

The values of $\langle \alpha \rangle$ calculated by LSS and C-CSI correspond well between each other. In general, the order of difference between them is 0.001. Values determined from diametrically opposite halves of the pipe under the same flow conditions are found to be identical. The largest difference (≈ 0.04) of the four pairs occurs for TN400 and TS400. Data collection from each half requires a long duration of time. Considering the possibility of instabilities in the flow during this time interval, this difference of 0.04 should be viewed within the achievable accuracies.

curves is small till half the radius, before decreasing steeply to lower values near the pipe wall. Distributions calculated at the bottom elevation (1.1 m above the mixer) peak at the 2nd or 3rd zone (see Figs. 5.12 to 5.14) though case BS600 has differed (Fig. 5.15).

The reconstructions from diametrically opposite halves have, in general, differed from each other. One of the more comparable pairs is TN600 and TS600 where the order of differences between the values at corresponding zones is only 0.1 (see Tables C.21 and C.24). Except for the large value in the 3rd zone, case TS400 (Fig. 5.28) is also similar to that of case TN400 (Fig. 5.27). Large differences have occurred, particularly at the central zones between the pairs from the bottom elevatioin. These differences suggest that,

(a) either, the flow in the pipe is strictly not radial, or,

(b) the data collection exercise needs better alignment.

5.3.3   Minor Cases

The objective of considering these Minor Case data was to study the reconstructions for different numbers of two-phase counts. While it is expected that errors decrease with larger number of counts, our aim is to experimentally determine an optimum number beyond which the change in calculated zonal values is negligible.

Reconstructions from data of different constant-counts become more similar with the overdetermination of the system of equations. A comprehensive study of the effect of different constant-counts will require the comparison between B-CSI reconstructions. This is not attempted here. Hence we consider only the LSS reconstructions of the Minor Cases.

In order to compare the closeness of low count solutions to the corresponding Major Case solution, we define the following "Closeness Factor (CF)" as follows.

$$CF = \sqrt{\sum_{i=1}^{n} (\alpha_i - \alpha 0_i)^2} \qquad (5.2)$$

where,

Minor Case	CF	Minor Case	CF	Minor Case	CF
TN403	0.1293	TS403	0.5417	BS603	0.3679
TN406	0.0099	TS406	0.4217	BS606	0.2724
TN401	0.0043	TS401	0.2859	BS601	0.1020
TN402	0.0044	TS402	0.1605	BS602	0.1015

Table 5.2: Closeness values

α_i = Minor case value in the ith zone

$\alpha 0_i$ = Corresponding Major case value .

For a given Minor Case, a larger value of CF indicates larger difference from the corresponding major case colution and vice versa. Table 5.2 shows these values.

It is seen that solutions with 2000 counts follow the 3000 count solutions closely. This is clear from Figs. 5.34 to 5.36 also.

The Minor Case solutions provide a way to verify whether large experimental errors have affected the data during the of measurements. The low count data was collected in the course of the collection of 3000-count data. That is, as the counter was proceeding towards 3000, the times at which lower counts were reached were noted down. The intervention of any event during the period of measurement such as, a flow instability, change in detector characteristics etc. will be reflected in the corresponding low-count solution. The absence of large variations among the Minor Case reconstructions belonging to a group is thus reassuring.

5.4   Conclusions

We now summarise the main results and suggestions as follows:

1. Void fraction distributions in vertical mercury-nitrogen two-phase flows in the upcomer of a Liquid Metal Magneto Hydrodynamic (LMMHD) system have been measured for various flow rates using three different reconstruction algorithms of gamma-ray tomography. Though not verified by alternate measurement techniques, the results from the algorithms are consistent with the expected behaviour of the LMMHD system. Hence the applicability of the present method of data collection and algorithms used for reconstruction appear to be promising.

2. The tomographic reconstructions are done with the algorithms B-CSI, LSS and C-CSI (described in Chapter 3). The local values calculated by LSS and C-CSI are found to be very close.

   When the rays are closely spaced, the difference in detector response for adjacent rays will be small, especially at the central region of the pipe. Possible experimental errors can mask this small difference. The effect of such errors on the reconstructions using the above algorithms have not been fully analysed in this thesis. This withstanding, C-CSI and LSS reconstructions are found to clearly bring out the trends from the corresponding B-CSI solutions. Hence if smoother reconstructions are required from noisy data with closely spaced rays, C-CSI and LSS would be the preferable algorithms for reconstruction. Also, to minimise such errors, it is preferable to keep the ray spacing at the centre large, compared to that at the periphery.

3. Statistical error estimates (1-σ) for local values obtained by B-CSI have been derived in Chapter 4. It is found that the statistical errors are negligible when 3000 photons are collected for each measurement. This is consistent with the recommendations of Munshi and Vaidya (see Ref. [26])

4. The variation in reconstructions from data-sets with different values of constant counts collected for each reading has been ascertained experimentally. It is seen that, for a mercury-nitrogen two-phase flow system,

the trend of the void-fration profiles with 2000 counts follows those of the 3000 counts cases quite closely. In a highly attenuating medium as this one, observing larger number of counts requires longer interval of measurement during which instrument and flow instabilities can occur. To reduce the duration of the experiment it is thus recommended that 2000 counts may be collected (per chord).

5. A couple of other radial tomography algorithms, Radial Polynomials [40] and Filtered Bessel Functions [39], maybe tried to reconstruct void fraction profiles with the data collected in this study. The past experience with these algorithms for air-water flow data has been reported by Munshi [47], and it would be interesting to do a similar study on the mercury-nitrogen flows also.

* * * * * *
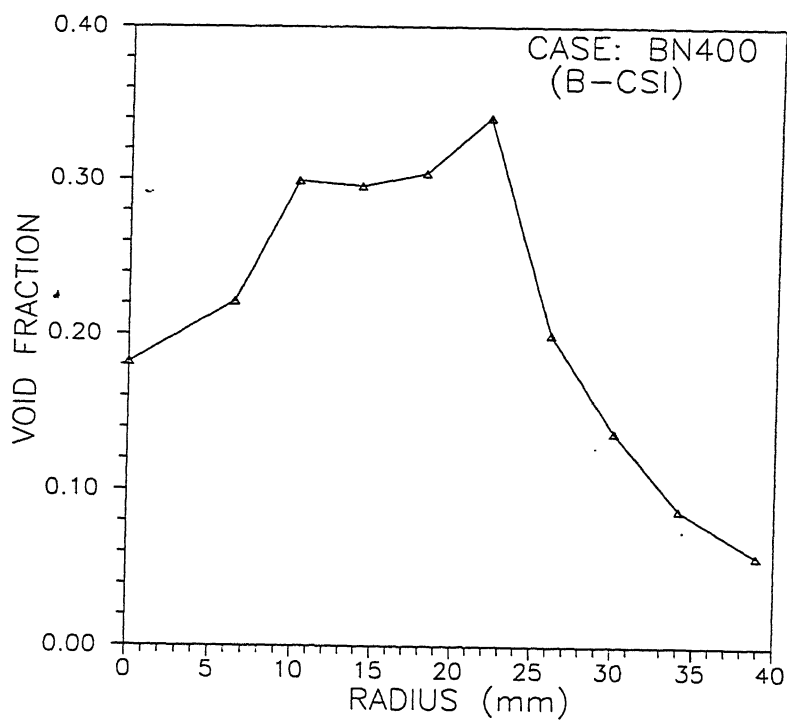
Figure 5.1: Void fraction distribution, $\alpha(r)$ vs r for BN400 (B-CSI)
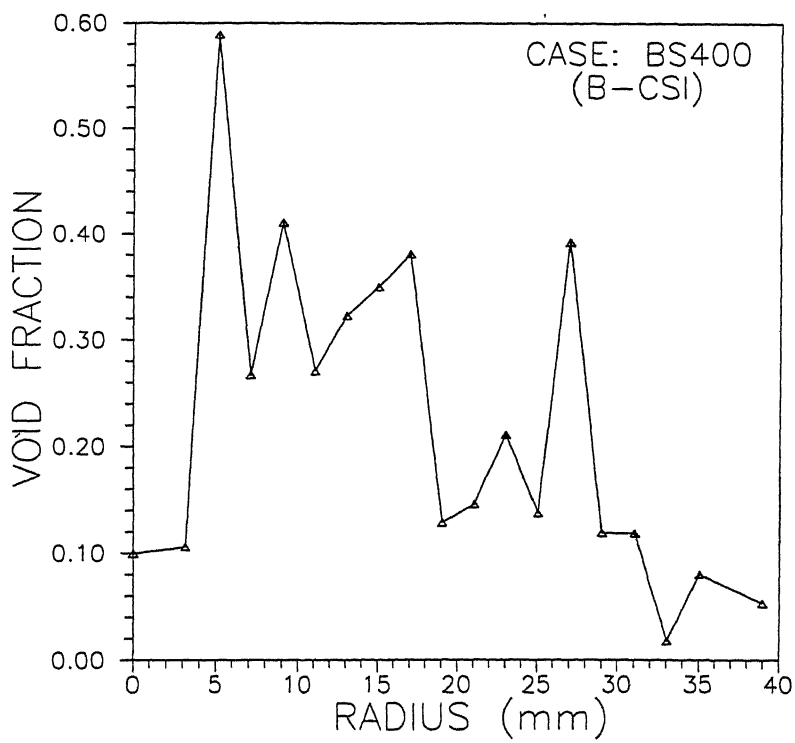
Figure 5.2: Void fraction distribution, $\alpha(r)$ vs r for BS400 (B-CSI)
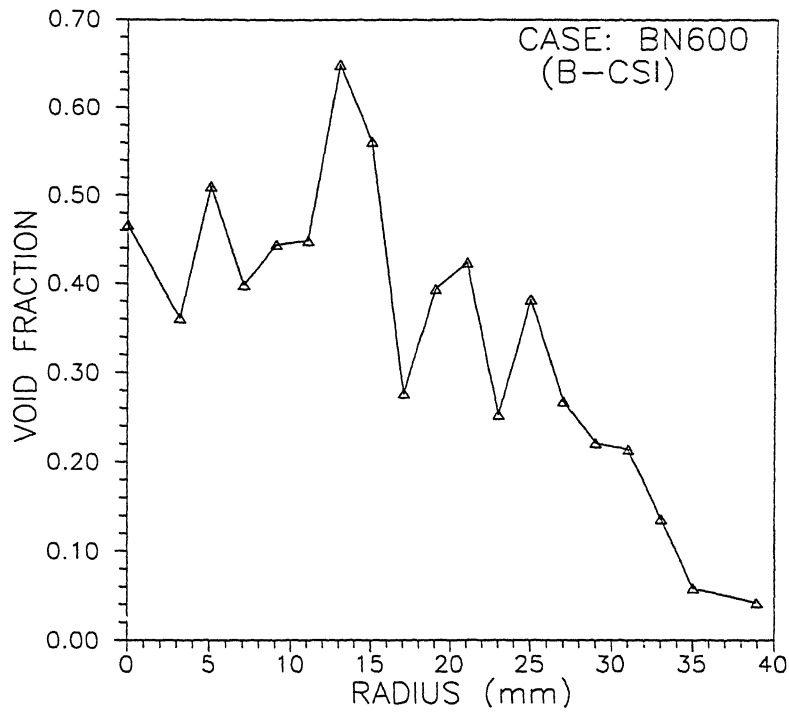
Figure 5.3: Void fraction distribution, $\alpha(r)$ vs r for BN600 (B-CSI)
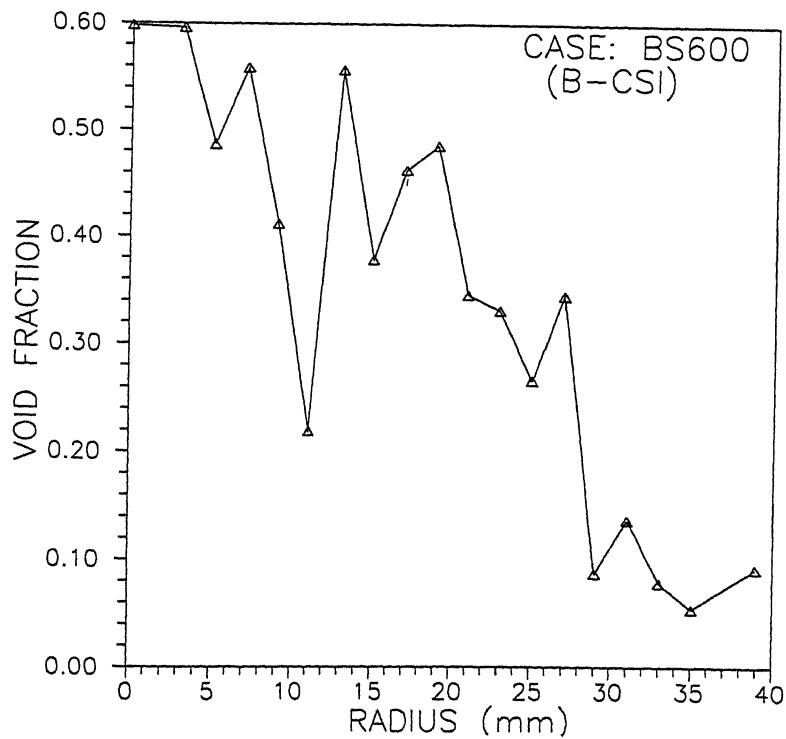
Figure 5.4: Void fraction distribution, $\alpha(r)$ vs r for BS600 (B-CSI)
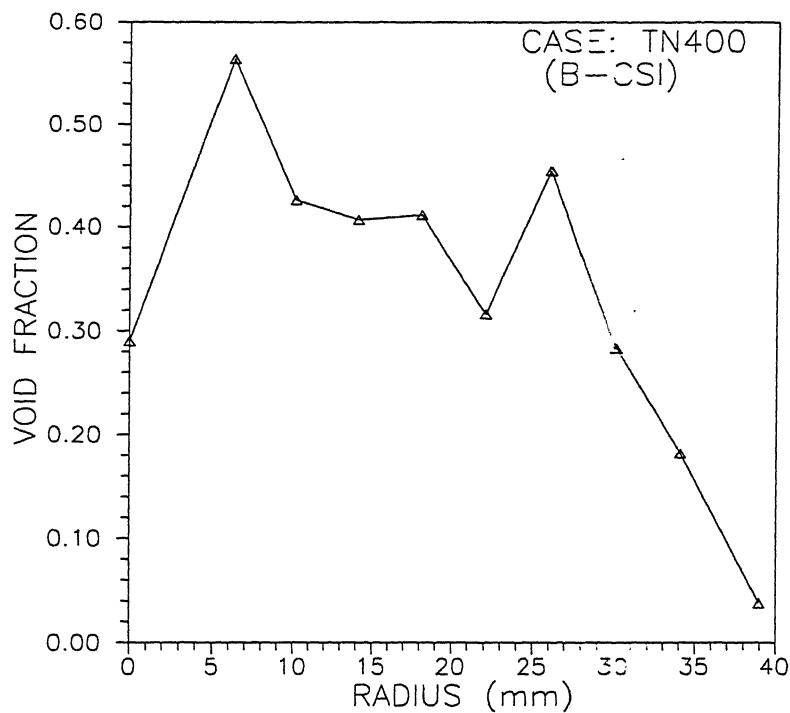
Figure 5.5: Void fraction distribution, $\alpha(r)$ vs r for TN400 (B-CSI)
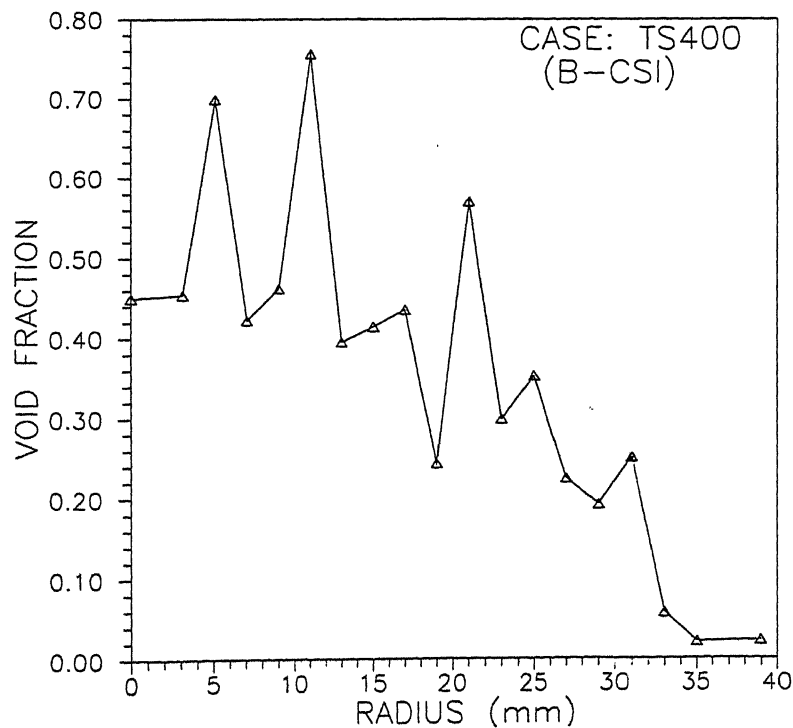
Figure 5.6: Void fraction distribution, $\alpha(r)$ vs r for TS600 (B-CSI)
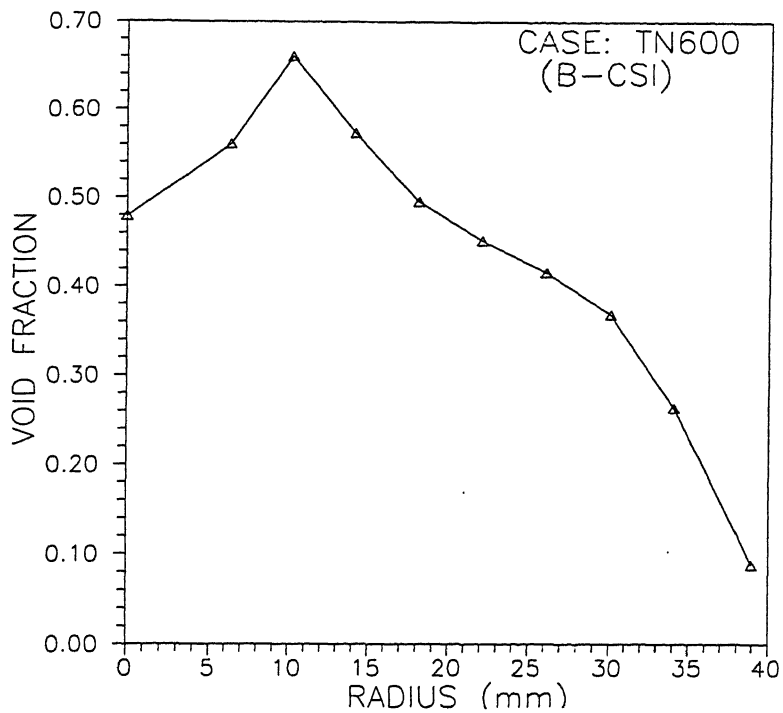
Figure 5.7: Void fraction distribution, $\alpha(r)$ vs r for TN600 (B-CSI)
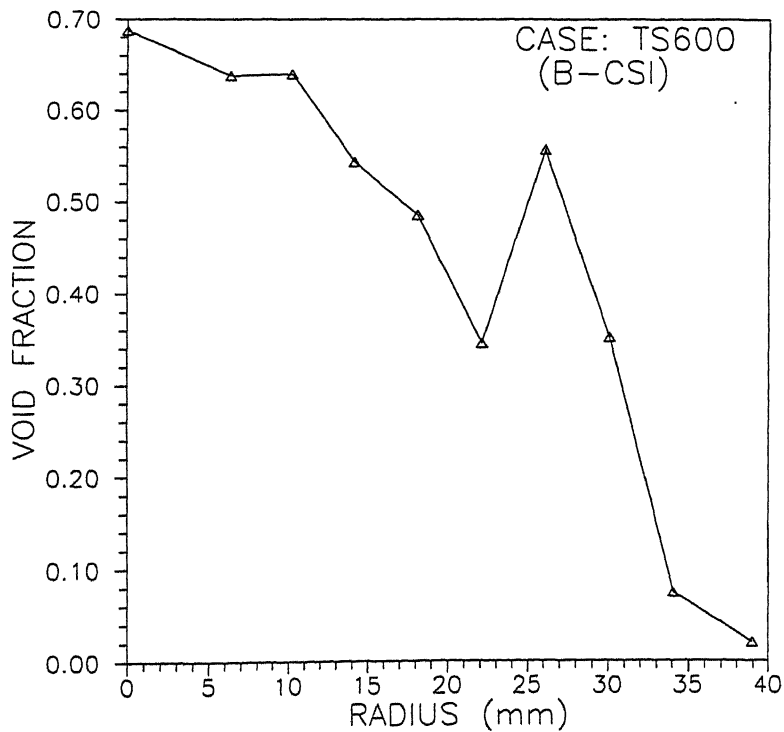
Figure 5.8: Void fraction distribution, $\alpha(r)$ vs r for TS600 (B-CSI)
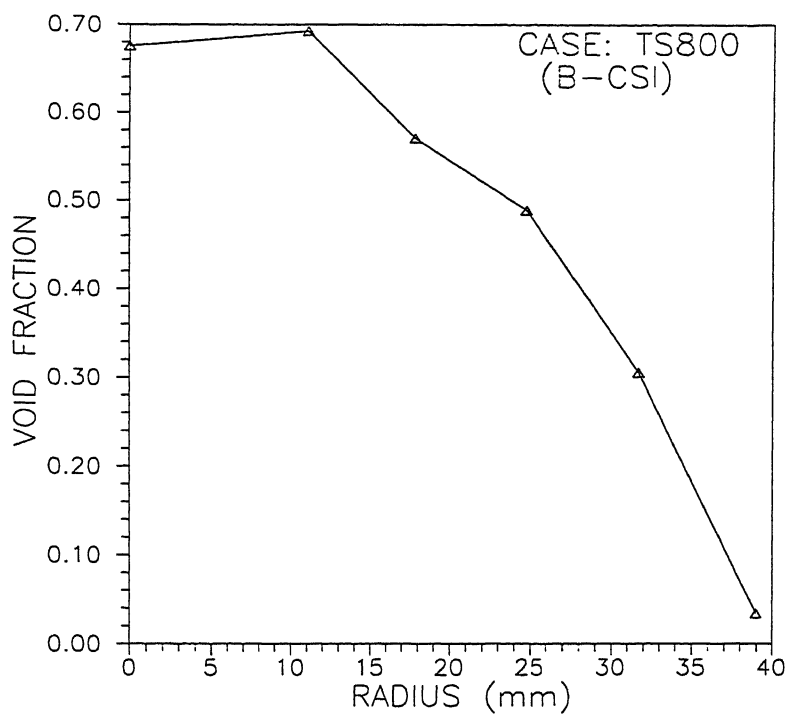
Figure 5.9: Void fraction distribution, $\alpha(r)$ vs r for TS800 (B-CSI)
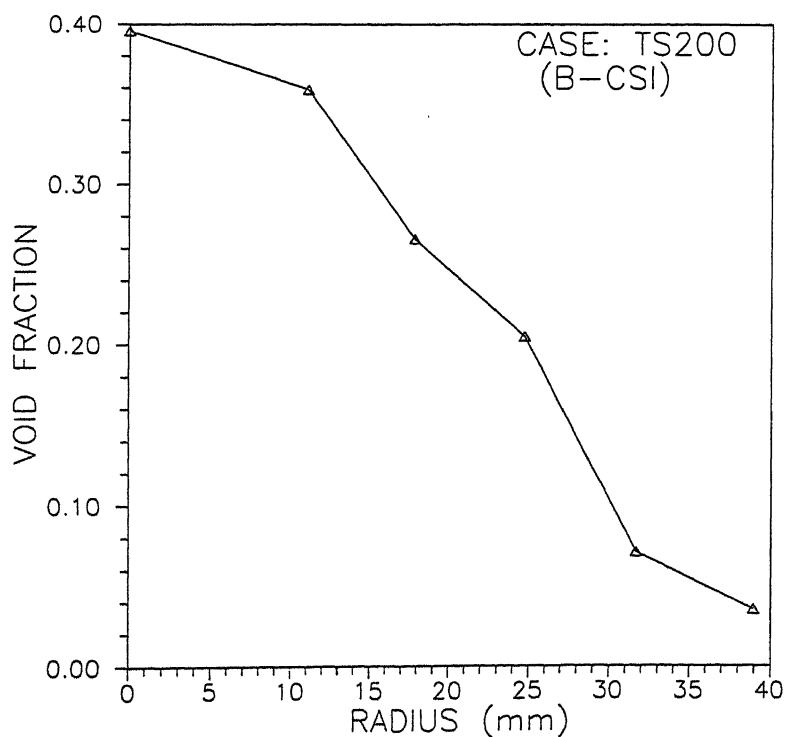
Figure 5.10: Void fraction distribution, $\alpha(r)$ vs r for TS200 (B-CSI)
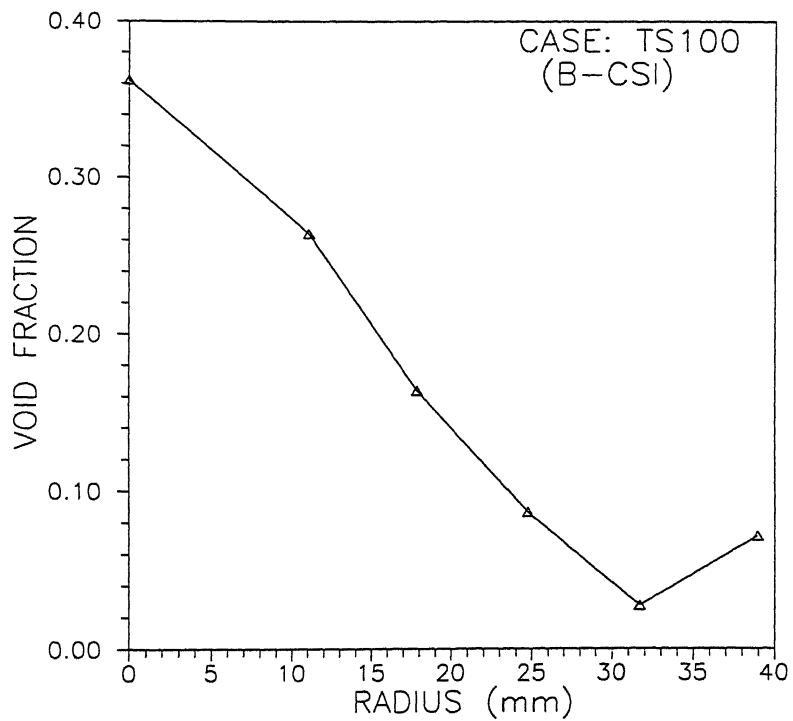
Figure 5.11: Void fraction distribution, $\alpha(r)$ vs r for TS100 (B-CSI)
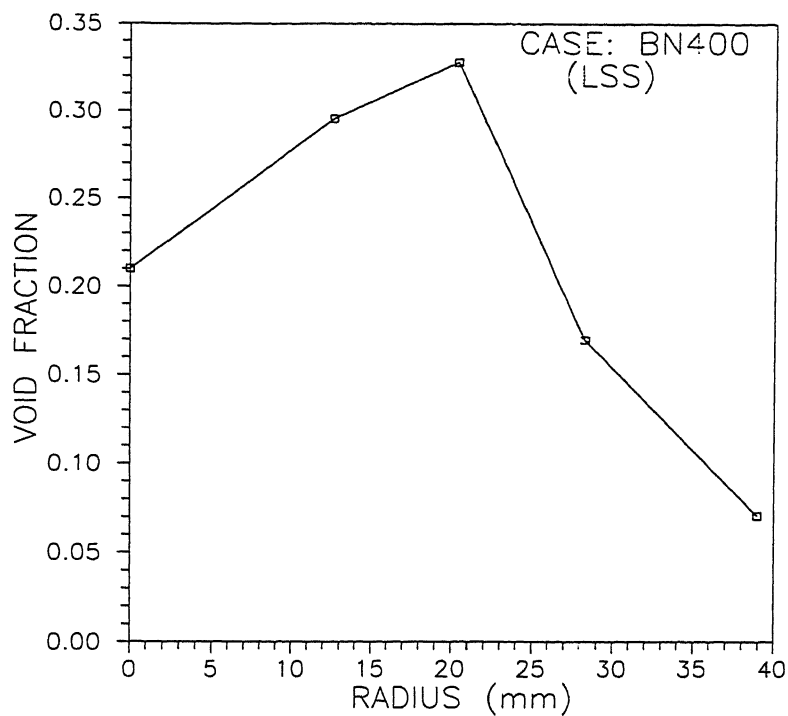
Figure 5.12: Void fraction distribution, $\alpha(r)$ vs r for BN400 (LSS)
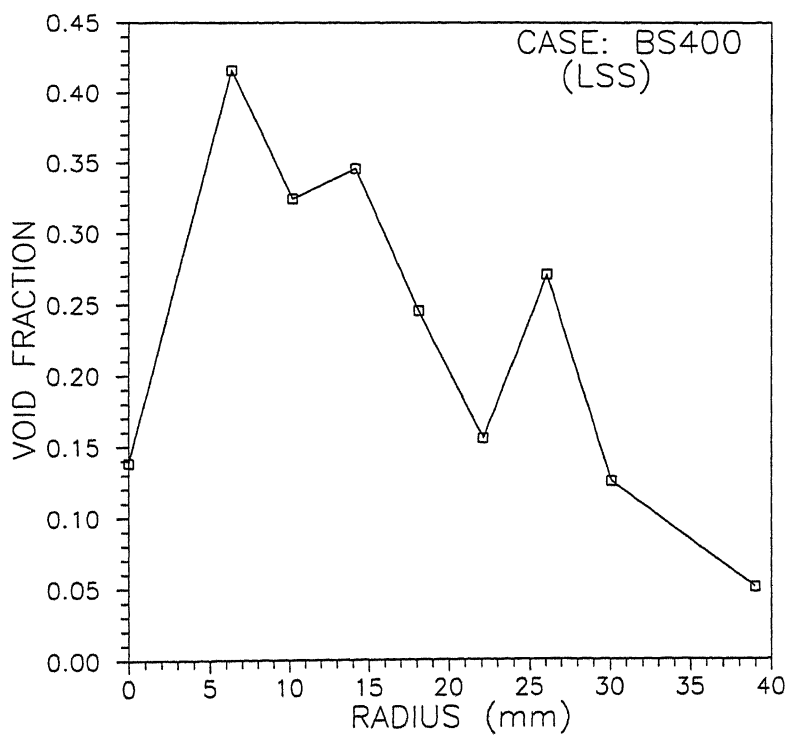
Figure 5.13: Void fraction distribution, $\alpha(r)$ vs r for BS400 (LSS)
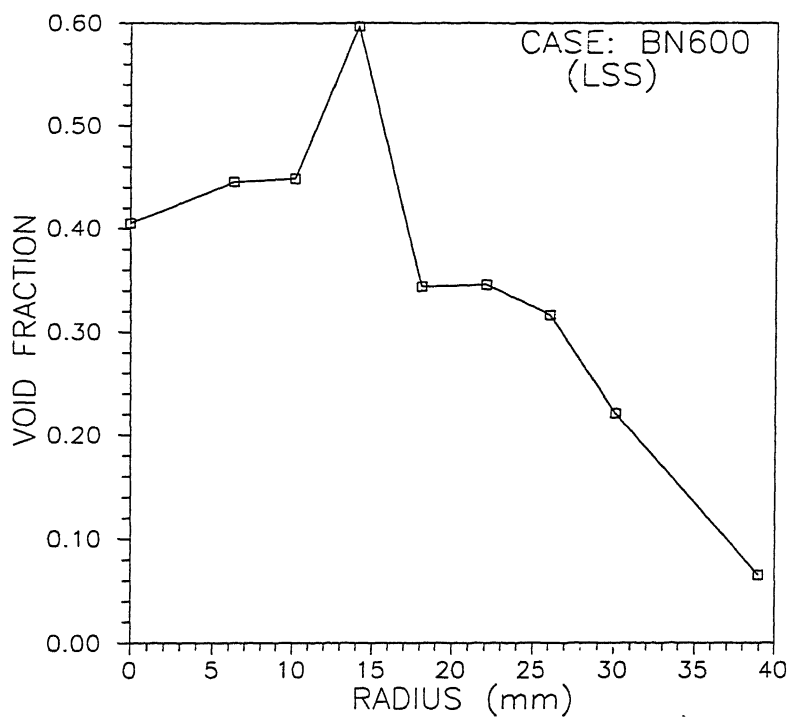
Figure 5.14: Void fraction distribution, $\alpha(r)$ vs r for BN600 (LSS)
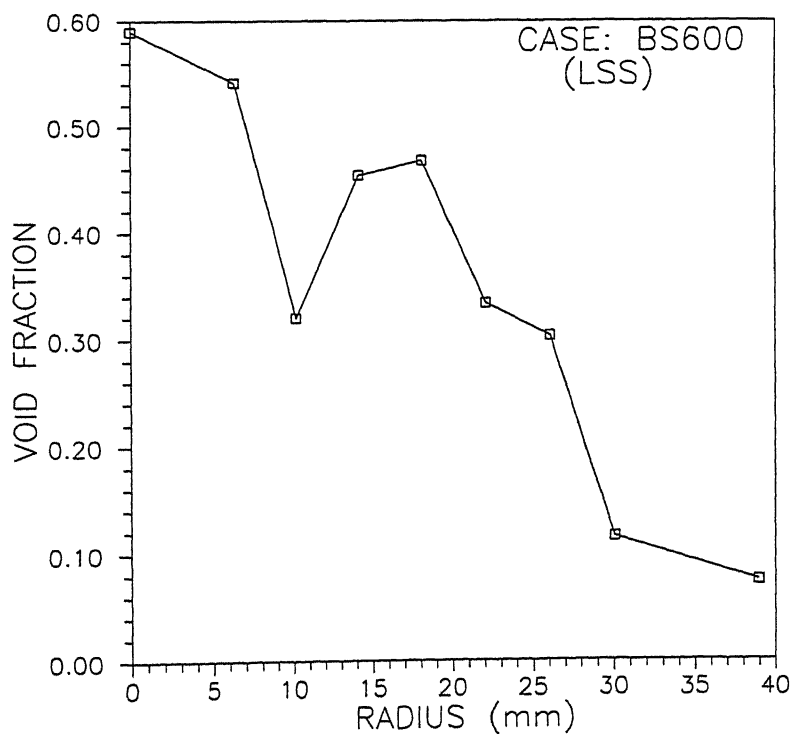
Figure 5.15: Void fraction distribution, $\alpha(r)$ vs r for BS600 (LSS)
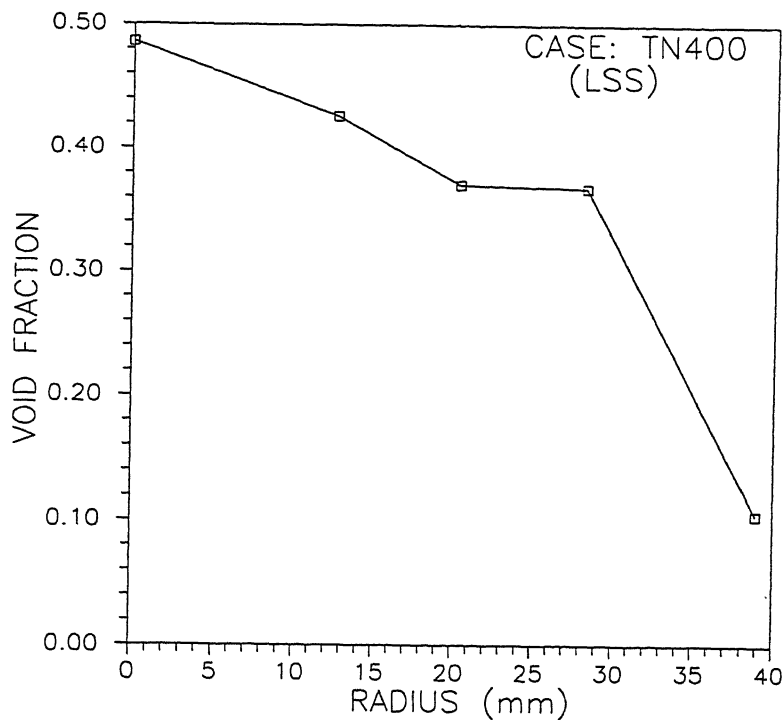
Figure 5.16: Void fraction distribution, $\alpha(r)$ vs r for TN400 (LSS)
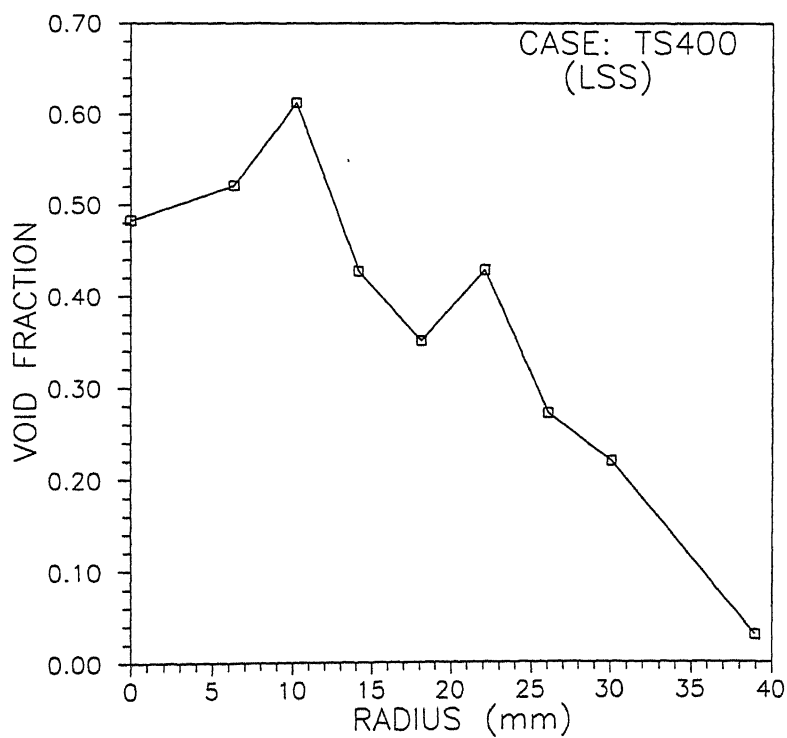
Figure 5.17: Void fraction distribution, $\alpha(r)$ vs r for TS400 (LSS)
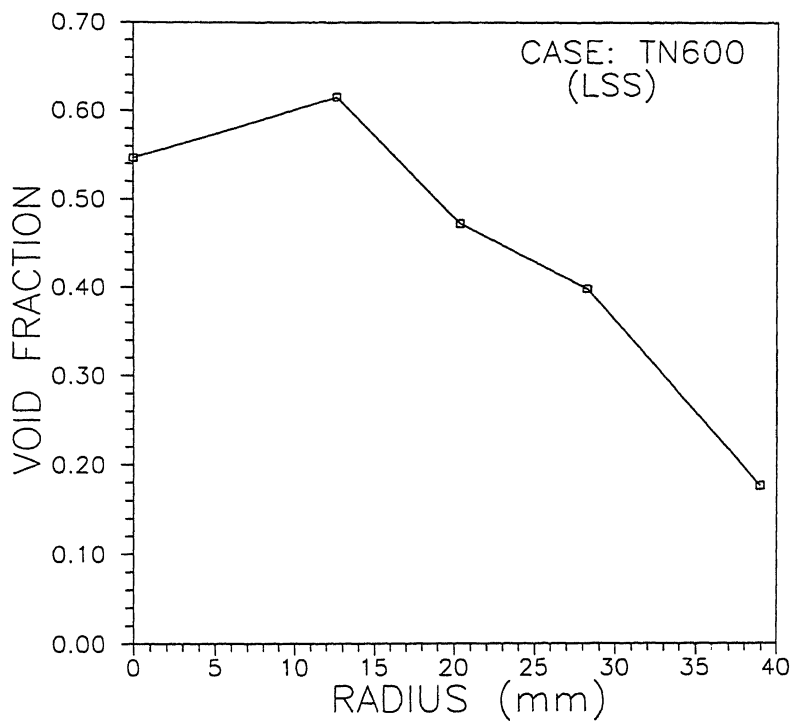
Figure 5.18: Void fraction distribution, $\alpha(r)$ vs r for TN600 (LSS)
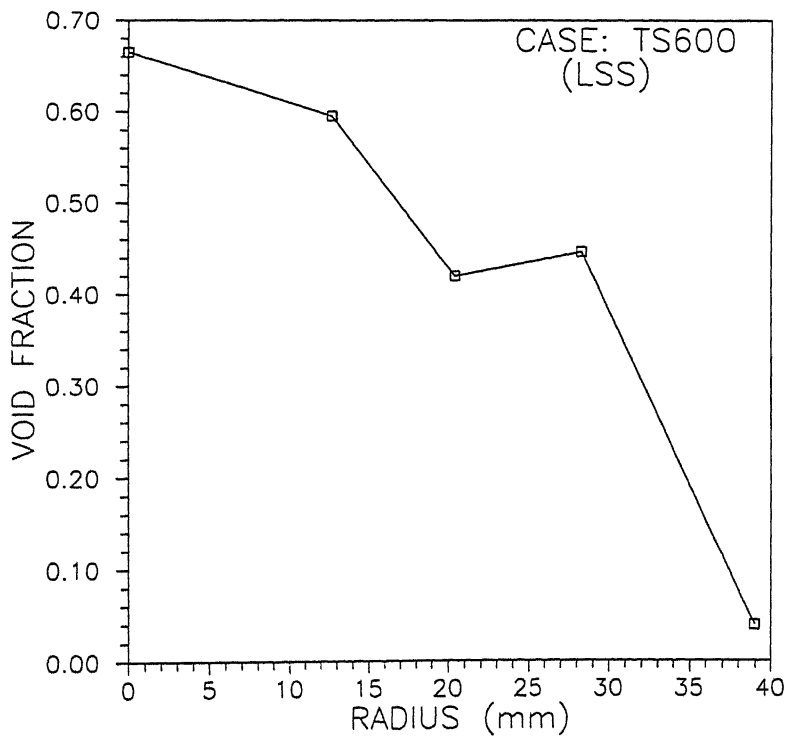
Figure 5.19: Void fraction distribution, $\alpha(r)$ vs r for TS600 (LSS)
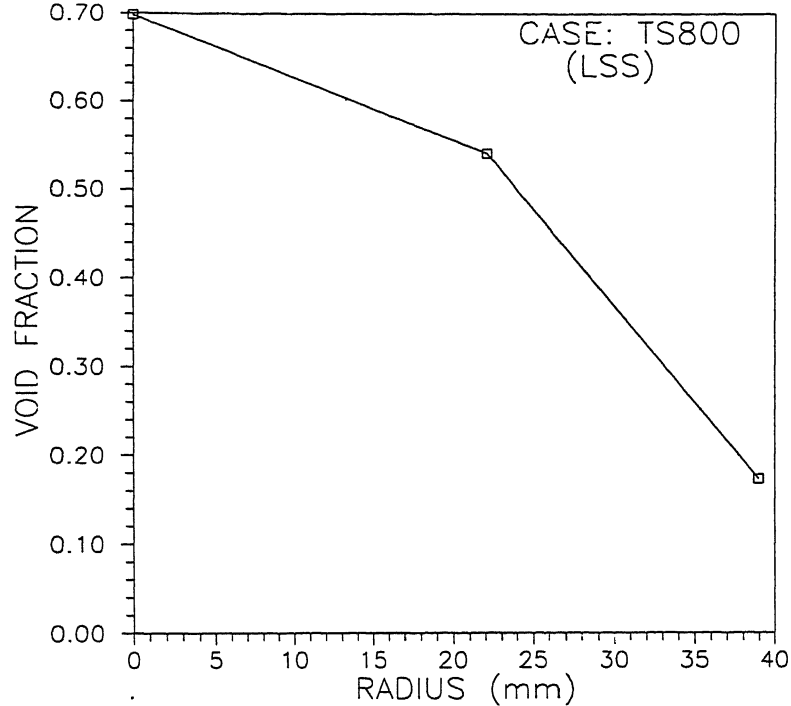
Figure 5.20: Void fraction distribution, $\alpha(r)$ vs r for TS800 (LSS)
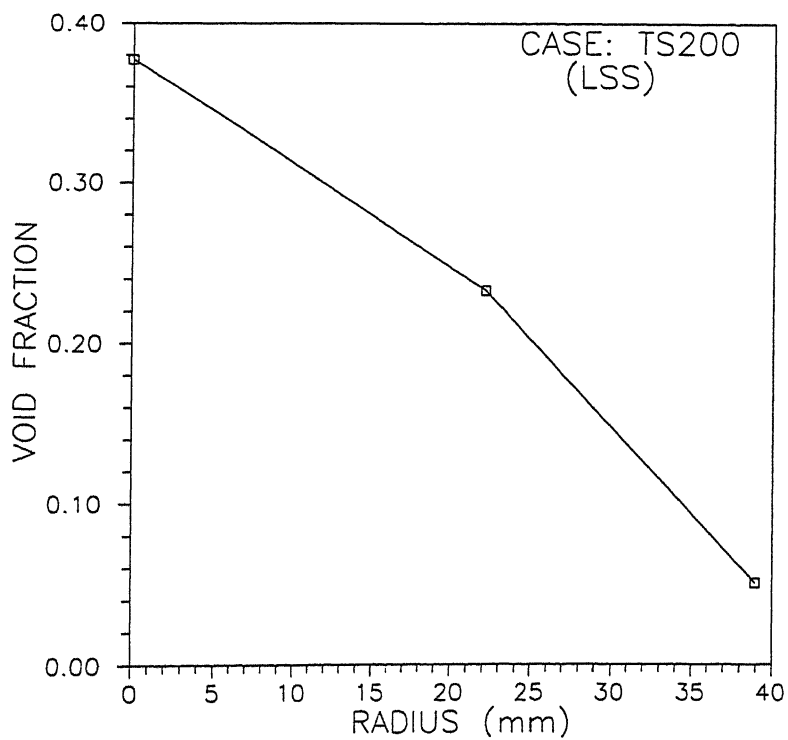
Figure 5.21: Void fraction distribution, $\alpha(r)$ vs r for TS200 (LSS)
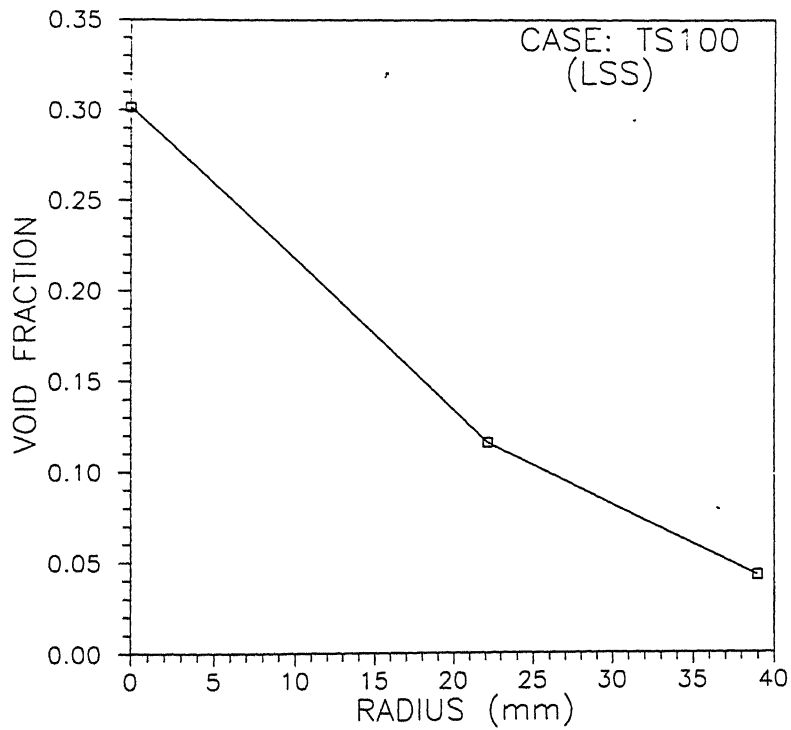
Figure 5.22: Void fraction distribution, $\alpha(r)$ vs r for TS100 (LSS)
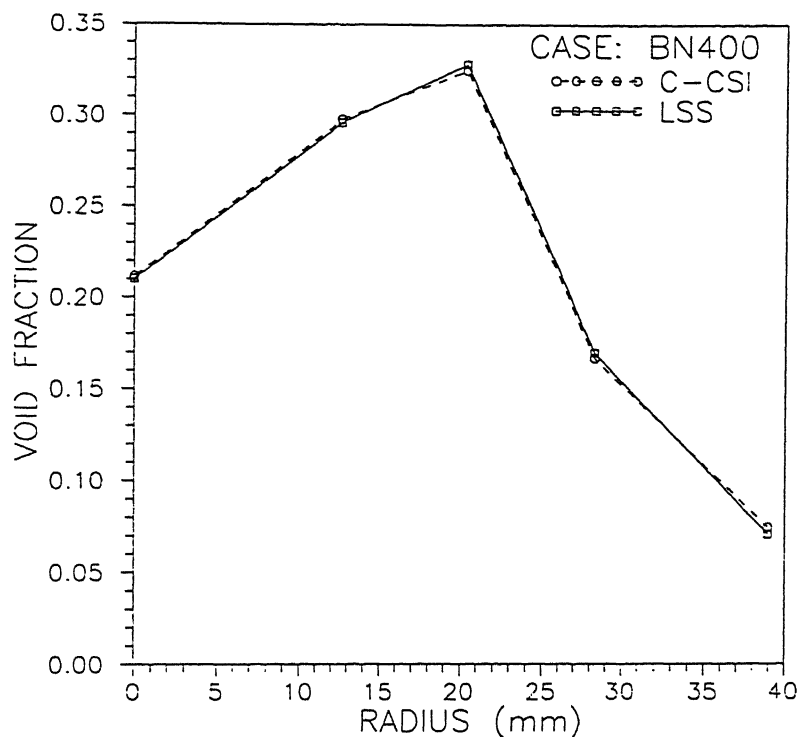
Figure 5.23: Void fraction distribution, $\alpha(r)$ vs r for BN400 (LSS & C-CSI)
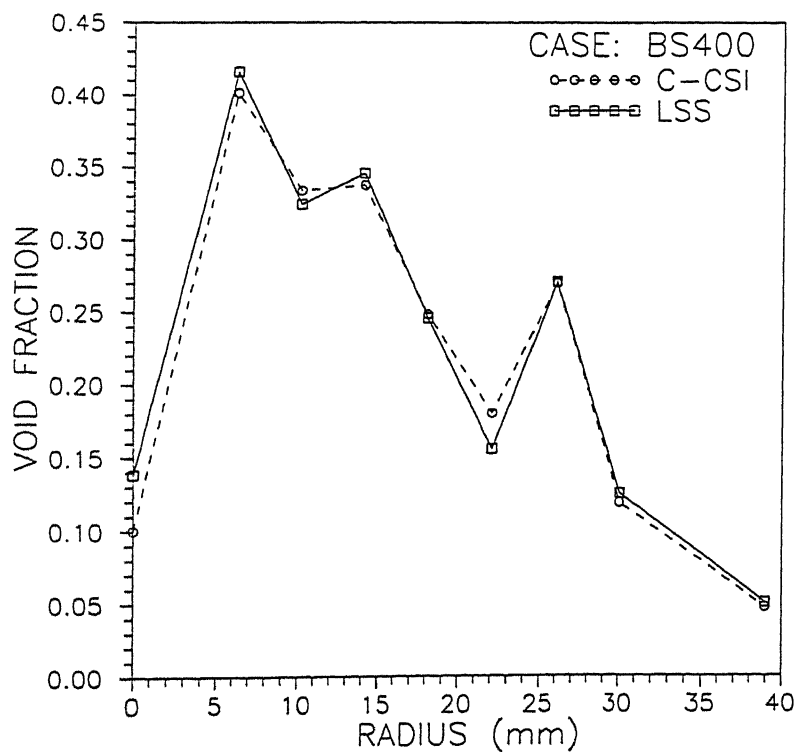
Figure 5.24: Void fraction distribution, $\alpha(r)$ vs r for BS400 (LSS & C-CSI)
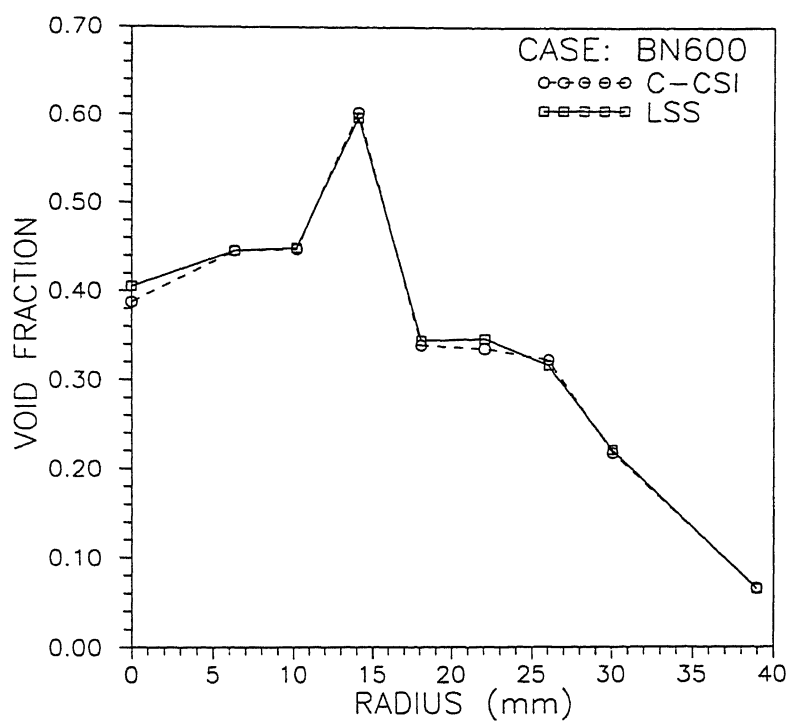
Figure 5.25: Void fraction distribution, $\alpha(r)$ vs r for BN600 (LSS & C-CSI)
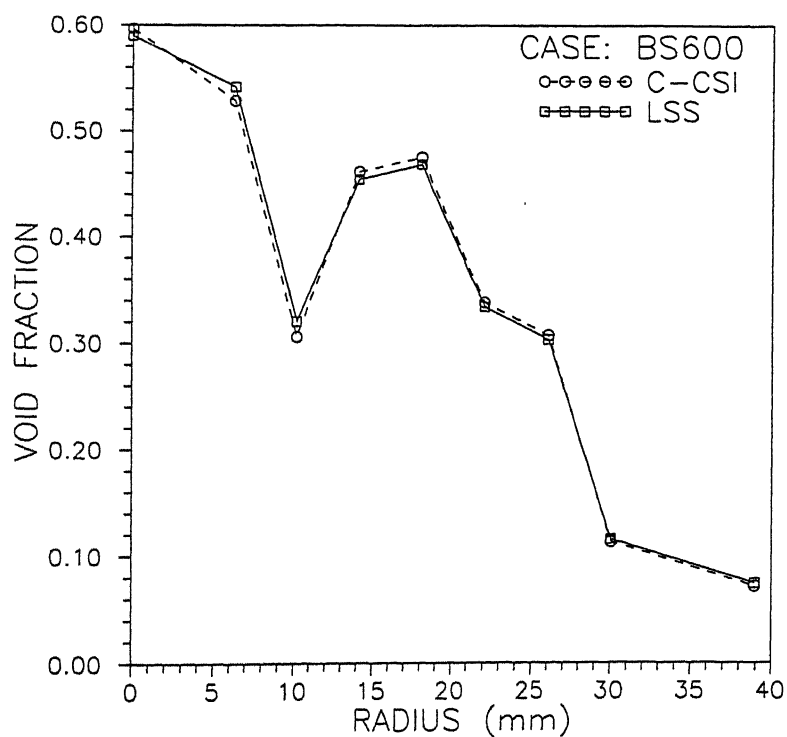
Figure 5.26: Void fraction distribution, $\alpha(r)$ vs r for BS600 (LSS & C-CSI)
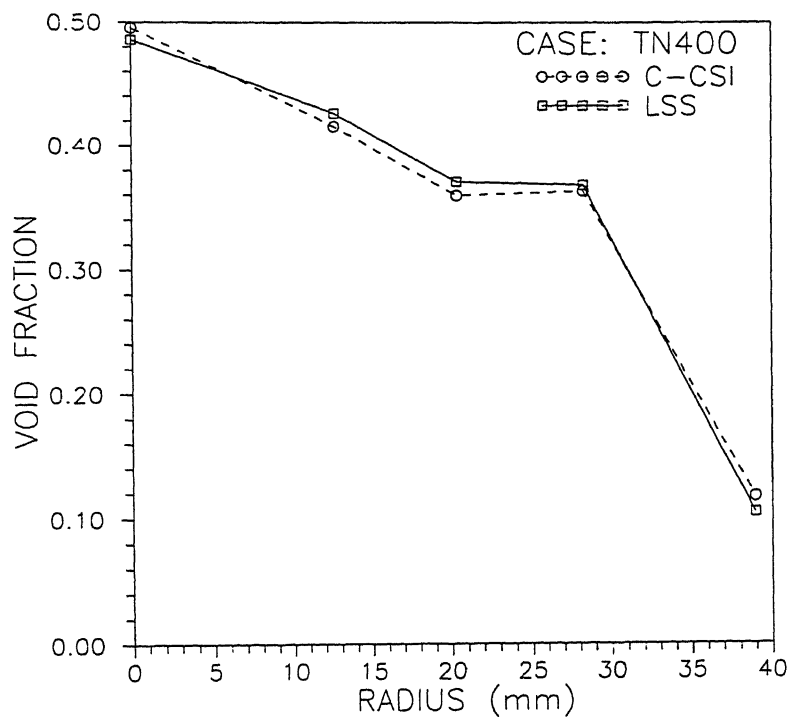
Figure 5.27: Void fraction distribution, $\alpha(r)$ vs r for TN400 (LSS & C-CSI)
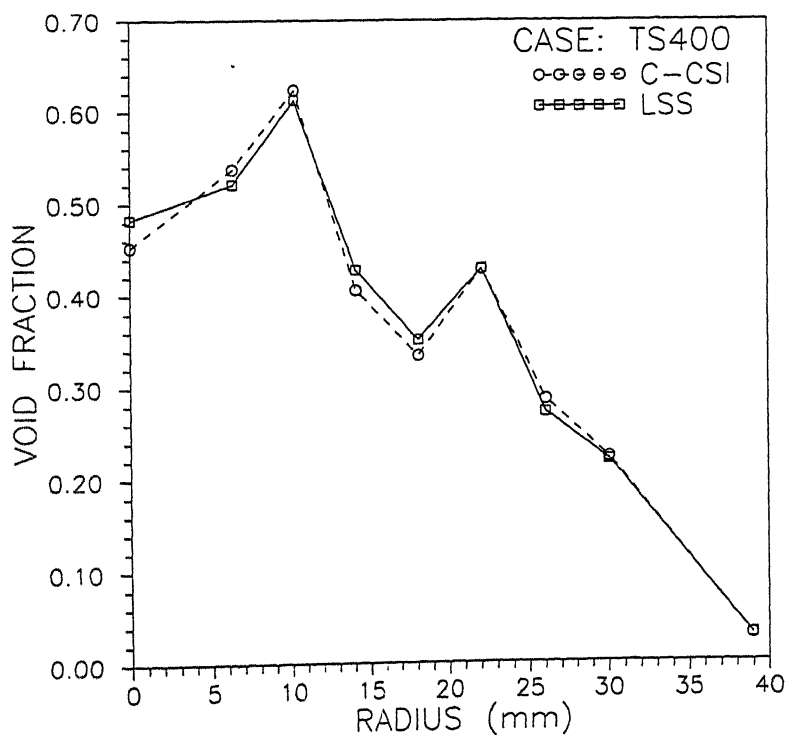
Figure 5.28: Void fraction distribution, $\alpha(r)$ vs r for TS400 (LSS & C-CSI)
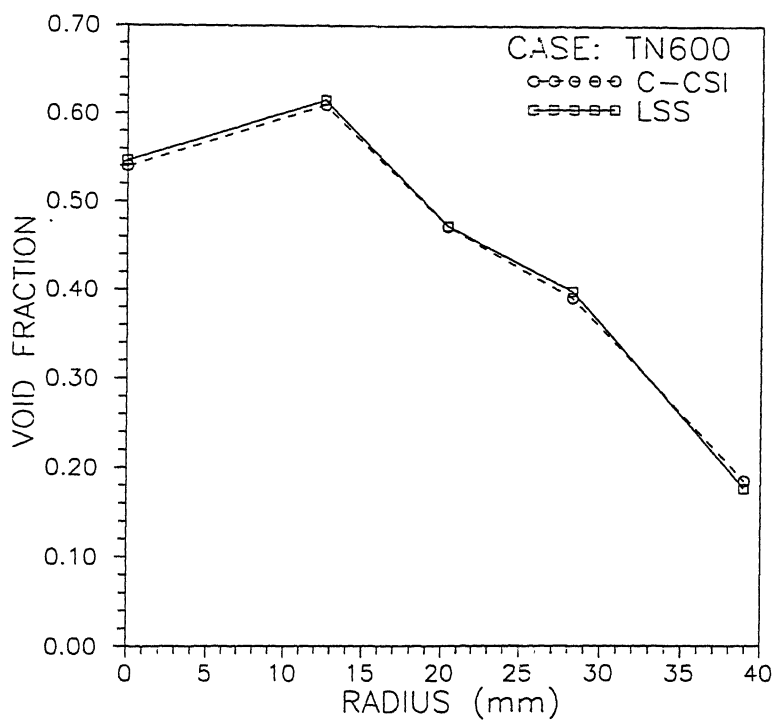
Figure 5.29: Void fraction distribution, $\alpha(r)$ vs r for TN600 (LSS & C-CSI)
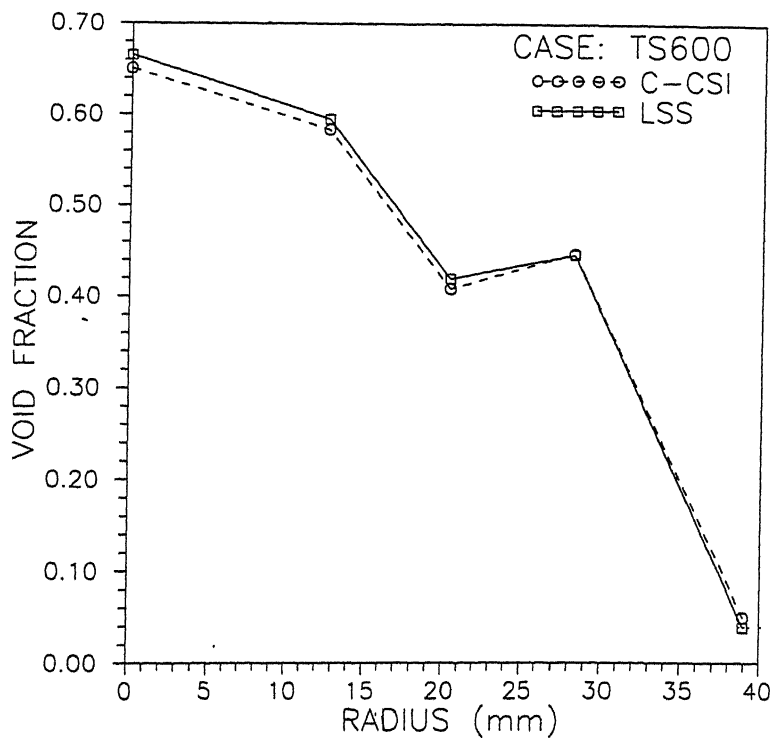
Figure 5.30: Void fraction distribution, $\alpha(r)$ vs r for TS600 (LSS & C-CSI)
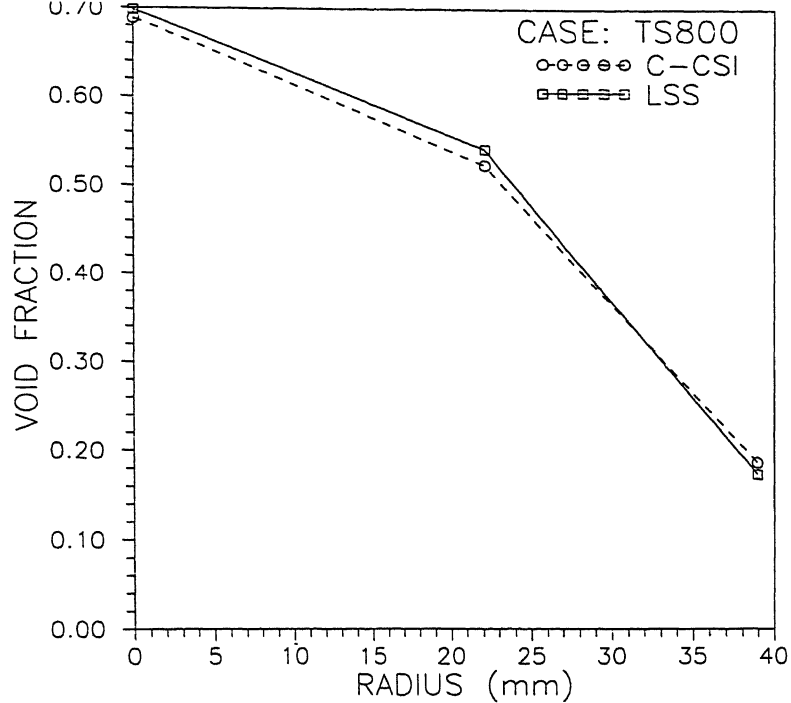
Figure 5.31: Void fraction distribution, $\alpha(r)$ vs r for TS800 (LSS & C-CSI)
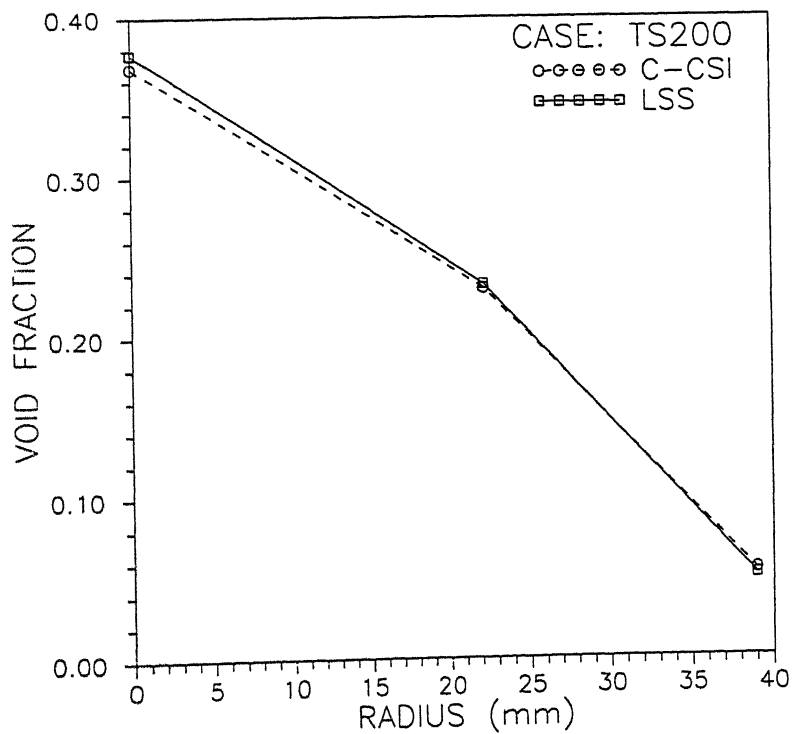
Figure 5.32: Void fraction distribution, $\alpha(r)$ vs r for TS200 (LSS & C-CSI)
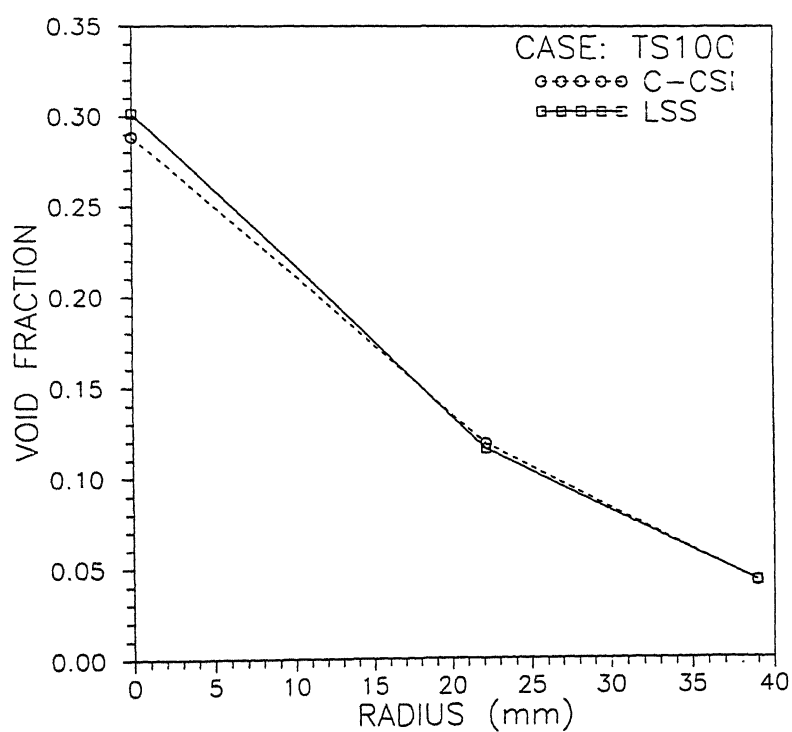
Figure 5.33: Void fraction distribution, $\alpha(r)$ vs r for TS100 (LSS & C-CSI)
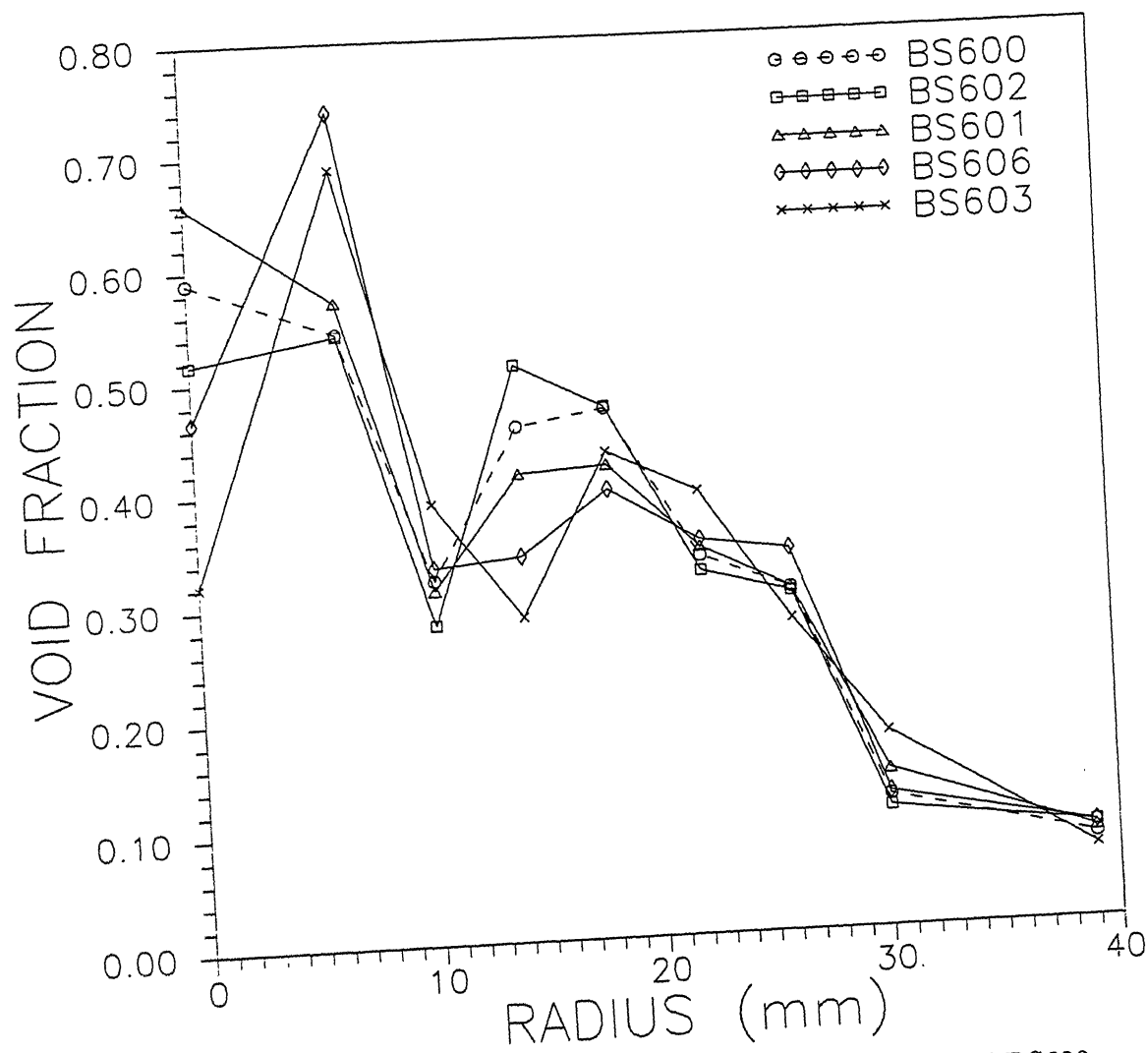
Figure 5.34: Void fraction distribution, $\alpha(r)$ vs r, for Minor Cases of BS600 (LSS) (Minimum number of two-phase counts: BS600 – 3000, BS602 – 2000, BS601 – 1000, BS606 – 600 & BS603 – 300.)
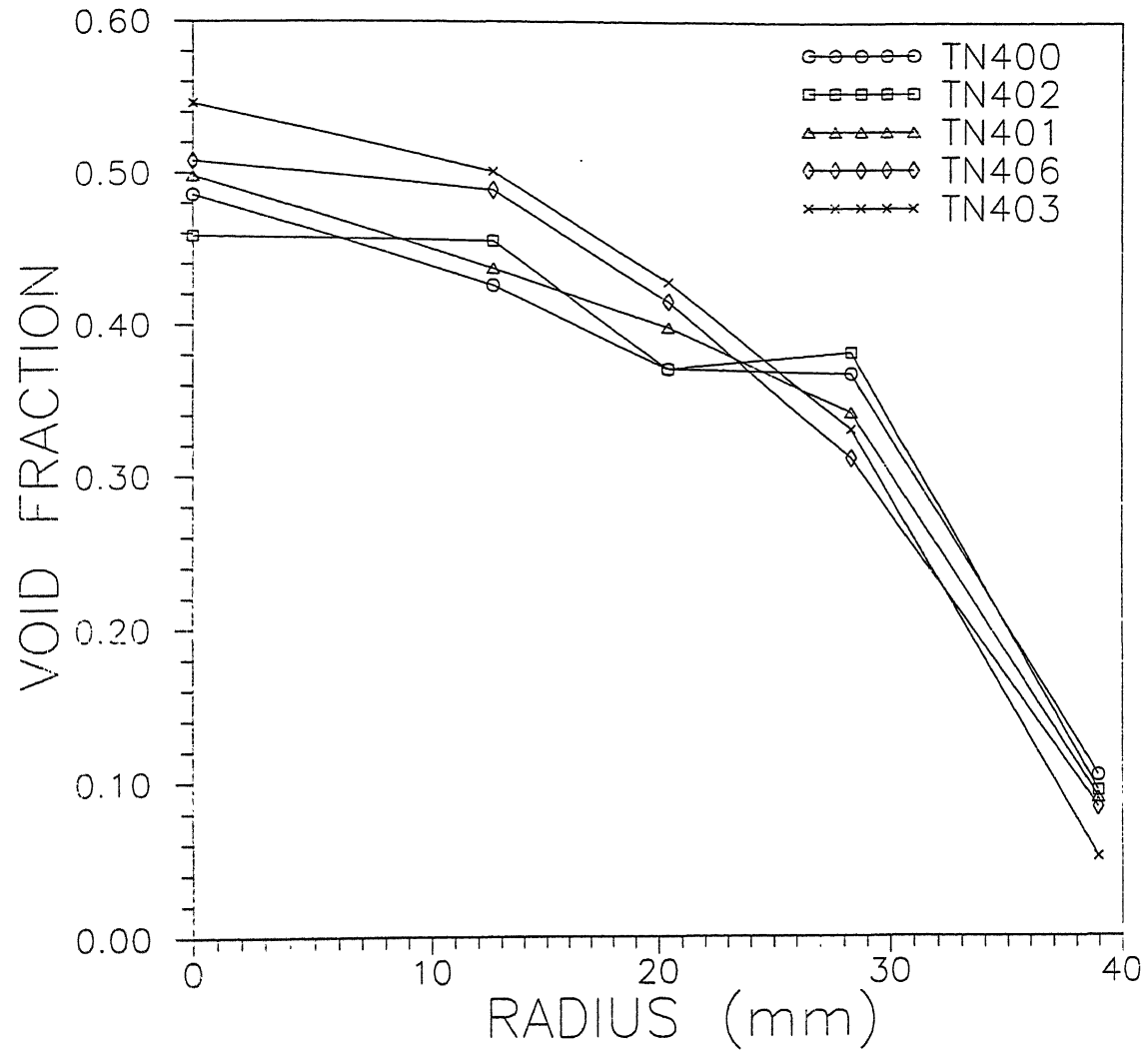
Figure 5.35: Void fraction distribution, $\alpha(r)$ vs r, for Minor Cases of TN400 (LSS) (Minimum number of two-phase counts: TN400 – 3000, TN402 – 2000, TN401 – 1000, TN406 – 600 & TN403 – 300.)
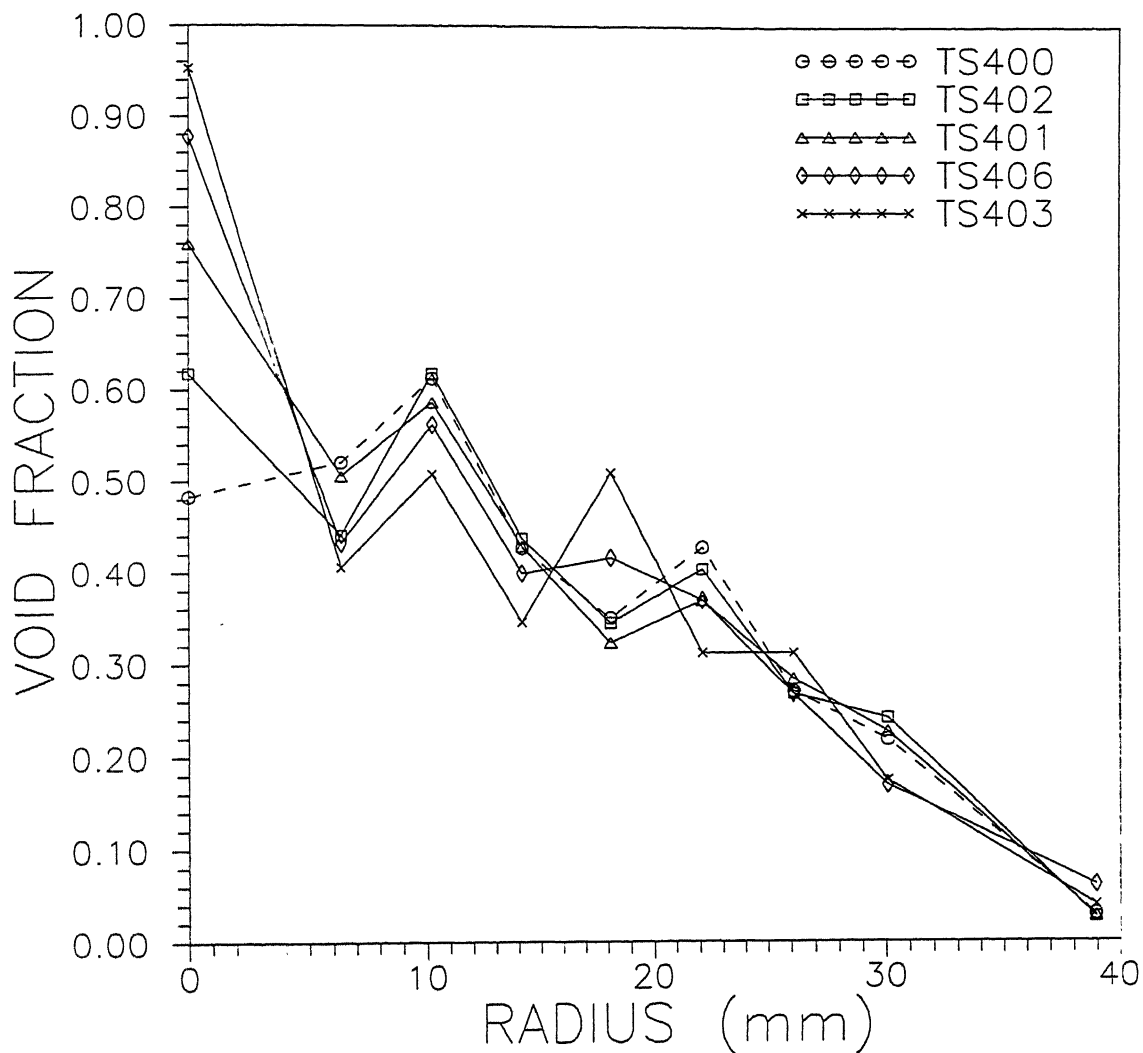
Figure 5.36: Void fraction distribution, $\alpha(r)$ vs r, for Minor Cases of TS400 (LSS) (Minimum number of two-phase counts: TS400 – 3000, TS402 – 2000, TS401 – 1000, TS406 – 600 & TS403 – 300.)

Bibliography

[1] P. Satyamurthy. Novel liquid metal magnetohydrodynamic electric power generators. *Physics Education*, 10:398 – 409, 1994.

[2] P. Satyamurthy, T.K. Thiyagarajan, N. Venkataramani, and V.K. Rohtagi. Design of 500W electrical steam-mercury Liquid Metal MHD experimental system. In *9th Int. Conf. on MHD Elec. Power Generation*, Thiruchirapally (India), 1989.

[3] O. C. Jones and J. M. Delhaye. Transient and statistical measurement techniques for two phase flows. *Int. Journal of Multiphase Flow*, 3:89–116, 1976.

[4] S. Z. Rouhani and M. S. Sohal. Two-phase flow patterns: A review of research results. *Progress in Nuclear Energy*, 11:219 – 259, 1983.

[5] A. J. C. Stekelenburg and T. H. J. J. van der Hagen. Two-phase flow monitoring by analysis of in-core neutron detector noise signals - a literature survey. *Annals of Nuclear Energy*, 20:611 – 621, 1993.

[6] J. B. Heineman, J. F. Marchaterre, and S. Mehta. Electromagnetic flow meters for void fraction measurement in two-phase metal flow. *Rev. Scient. Instr.*, 34:399 – 401, 1963.

[7] Isbin. Void fractions in two-phase steam-water flow. *AIChE Journal*, 3:136 – 142, 1957.

[8] Isbin. Void fractions in two-phase flow. *AIChE Journal*, 3:427 – 432, 1959.

[9] E. J. Gibson, R. Rennie, and B. A. Say. The uses of gamma radiation in the study of expansion of gas-liquid systems. *Int. J. Appl. Radiation and Isotopes*, 2:129 – 135, 1957.

[10] R. W. Pike, B. Wilkins, and H. C. Ward. Measurement of void fraction in two-phase flow by x-ray attenuation. *AIChE Journal*, 11:794 – 799, 1965.

[11] A. A. Harms and C. F. Forrest. Dynamic effects in radiation diagnosis of fluctuating voids. *Nuclear Science and Engineering*, 46:408, 1971.

[12] S. Banerjee, E. Hussein, and D. A. Meneley. Simulation of a neutron scattering method for measuring void fraction in two-phase flow. *Nuclear Engineering and Design*, 53:393 – 405, 1979.

[13] M. Petrick and B. S. Swanson. Radiation attenuation method of measuring density of a two-phase fluid. *Rev. Scient. Instr.*, 29:1079 – 1085, 1958.

[14] G. D. Zakaib, A. A. Harms, and J. Valachopoulos. Two-dimensional reconstruction by neutron transmission. *Nuclear Science and Engineering*, 65:145 – 154, 1978.

[15] P. Munshi. Two-phase flow studies in the bubbly flow regime using a scanning gamma-ray densitometer. Master's thesis, Ohio State University, 1979.

[16] F.A. Kulacki, P. A. Schlosser, A. C. De Vuono, and P. Munshi. A preliminary study of the application of reconstruction tomography to void-fraction measurements in two-phase flow. In *Proc. ANS/ASME/NRC Topical Meeting on Nuclear Reactor Thermal-Hydraulics. NUREG/CP-0014*, pages 904–922, Saratoga Springs, (New York), 1980.

[17] E. Hussein and D. A. Meneley. Single exposure neutron tomography. *Int. Journal of Multiphase flow*, 12:1 – 34, 1986.

[18] R. Hummel and U. Wesser. Determination of density oise in a two-phase flow by x-ray CT. *Progress in Nuclear Energy*, 21:333 –341, 1988. (Proceedings of SMORN - V).

[19] S. Morooka, T. Ishizuka, M. Iizuka, and K. Yoshimura. Experimental study on void fraction in a simulated BWR fuel assembly (Evaluation of cross-sectional averaged void fraction). *Nuclear Engineering and Design*, 114:91 – 98, 1989.

[20] A. Inoue, T. Kurosu, T. Akoi, M. Yagi, T. Mitsutake, and S. Morooka. Void fraction distribution in BWR fuel assembly and evaluation of sub-channel code. *Journal of Nuclear Science and Technology*, 32:629 – 640, 1995.

[21] T.K. Thiyagarajan, P. Satyamurthy, N.S. Dixit, N.Venkataramani, A.Garg, and N.R. Kanvinde. Void fraction profile measurements in two-phase mercury-nitrogen flows using gamma-ray attenuation method. *Experimental Thermal and Fluid Science*, 10:347–354, 1995.

[22] G. T. Herman. *Image Reconstruction from Projections:Fundamentals of Computerised Tomography*. Academic Publishers, 1990.

[23] R.P. Gardner and R. L. Ely Jr. *Radioisotope Measuremnt Application in Engineering*. Reinhold Publishing Corp., New York, 1967.

[24] B. K. Malaviya and R. T. Lahey, Jr. Analysis of error in instantaneous void fraction measurements by a dual-beam x-ray technique. *Trans. Am. Nucl. Soc.*, 34:876, 1980.

[25] P. A. Schlosser, A. C. De Vuono, F. A. Kulacki, and P. Munshi. Analysis of high-speed CT scanners for non-medical applications. *IEEE Transactions on Nuclear Science*, NS-27:788, 1980.

[26] P. Munshi and M. S. Vaidya. Void fraction reconstruction with stochastic data. *Experiments in Fluids*, 16:217 – 222, 1994.

[27] A. A. Harms and F. A. R. Laratta. Dynamic bias in radiation interrogationof two phase flow. *Int. J. Heat and Mass Transfer*, 16:1459 – 1465, 1973.

[28] F. A. R. Laratta and A.A. Harms. A reduced formula for the dynamic bias in radiation interrogation of two-phase flows. *Int. J. of Heat and Mass Transfer*, page 264, 1974.

[29] W. T. Hancox and A. A. Harms. Discrete-time neutron interrogation of liquid flow systems. *Trans. Am. Nucl. Soc.*, 14:699, 1971.

[30] P. R. Barret. Systematic errors in the discrete time-interval transmission method for the estimation of void statistics in boiling channels. *Nuclear Engineering and Design*, 30:316–327, 1974.

[31] O. C. Jones and N. Zuber. The interrelation between void fraction fluctuations and flow patterns in two-phase flow. *Int. J. Multiphase Flow*, 2:273 – 306, 1975.

[32] M. A. Vince and R. T. Lahey Jr. On the development of an objective flow regime indicator. *Int. J. Multiphase Flow*, 8:93 – 124, 1982.

[33] R. T. Lahey Jr., G. Krycuk, and B. K. Malaviya. A high intensity x-ray system for stochastic measurements of two-phase flows. *Trans. Am. Nucl. Soc.*, 30:497, 1978.

[34] D. R. Wyman and A. A. Harms. Statistical uncertainty in the radiation diagnosis of two-phase flows. *Nuclear Engineering and Design*, 85:261, 1985.

[35] A. A. Harms, S. Lo, and W. T. Hancox. Measurement of time-averaged voids by neutron diagnosis. *Journal of Applied Physics*, 42:4080 – 4082, 1971.

[36] A. M. C. Chan and S. Banerjee. Design aspects of gamma densitometers for void fraction measurements in small scale two-phase flows. *Nuclear Instruments & Methods*, 190:135, 1981.

[37] A. C. De Vuono, P. A. Schlosser, F. A. Kulacki, and P. Munshi. Design of an isotopic CT scanner for two phase flow measurements. *IEEE Transactions on Nuclear Science*, NS-27:814 – 820, 1980.

[38] P. Munshi. A review of CT with application to two-phase flows. *Sadhna*, 15:93–55, 1990.

[39] R. K. S. Rathore, P. Munshi, V. K. Bhatia, and S. Pandimani. Filtered bessel functions in computerised tomography. *Nuclear Engineering Design*, 108:375 – 384, 1988.

[40] R. K. S. Rathore, P. Munshi, I. D. Dhariyal, and S. Swamy. Tomographic reconstruction of density field using radial polynomials. *Nuclear Technology*, 78:7 – 12, 1987.

[41] R. K. S. Rathore, P. Munshi, R. K. Jarwal, and I. D. Dhariyal. Investigation of bubbly air-water flow using chord segment inversion technique. *Nuclear Technology*, 82:227 – 304, 1988.

[42] P. R. Bevington. *Data Reduction and Error Analysis for Engineers.* Mc Graw Hill, New York, 1969.

[43] G. F. Knoll. *Radiation Detection and Measurement.* John Wiley, New York, 1979.

[44] E. Storm and H.I. Israel. Photon cross sections from 1 keV to100 MeV for elements $Z = 1$ to $Z = 100$. *Nuclear Data Tables (Sect. A)*, 71, 1970.

[45] T. K. Thiyagarajan, N. S. Dixit, P. Satyamurthy, N. Venkataramani, and V. K. Rohtagi. Gamma-ray attenuation method for void fraction measurement in fluctuating two-phase liquid metal flows. *Measurement Science and Technology*, 2:69–74, 1991.

[46] Richard L. Branham Jr. *Scientific Data Analysis: An Introduction to Overdetermined Systems.* Springer-Verlag, New York, 1990.

[47] P. Munshi. A comparative study of void fraction measurement by some algorithms of gamma-ray tomography. In A. R. Balakrishnan and S. Srinivasa Murthy, editors, *Proc. 11th National Heat and Mass Transfer Conf.*, Madras, 1991. p 309

Appendix A

A.1 Logarithmic Formula for Chord-averaged Void fraction (Derivation)

For a two-phase gas-liquid flow, the average mixture density along a chord in the flow area, $\bar{\rho}_m$, is related to the phase densities by the following relation.

$$\bar{\rho}_m = (1 - \bar{\alpha})\bar{\rho}_l + \bar{\alpha}\bar{\rho}_g \qquad (A.1)$$

where $\bar{\alpha}$ is the chord-averaged void fraction and $\bar{\rho}_l$ & $\bar{\rho}_g$ are the liquid and gas densities. If gas-density is much smaller than the liquid density, then

$$\bar{\rho}_m = (1 - \bar{\alpha})\bar{\rho}_l \qquad (A.2)$$

Since linear attenuation coefficient is proportional to density we may write,

$$\bar{\mu}_{tp} \approx (1 - \bar{\alpha})\bar{\mu}_l \qquad (A.3)$$

where $\bar{\mu}_{tp}$ & $\bar{\mu}_l$ are the linear attenuation coefficients of two-phase mixture and liquid respectively. Now consider a gamma ray beam passing through the cross section of a pipe (see Fig. A.1). If the pipe contains two-phase flow the countrate measured by the detector is given by

$$I_{tp} = I_0 e^{-(\bar{\mu}_l(1-\bar{\alpha})x + \bar{\mu}_p x_p)} \qquad (A.4)$$
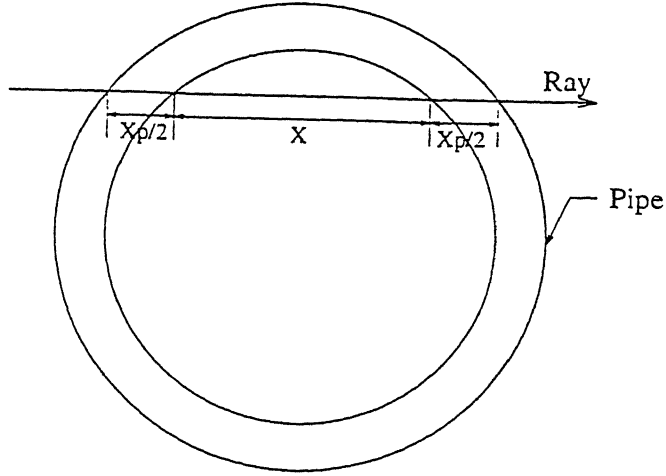
Figure A.1: Ray through the pipe

where,

x = Length of the ray in the flow-area of the pipe

x_p = Length of the ray passing through the pipe walls.

$\bar{\mu}_p$ = Linear attenuation coefficient of the pipe material

I_0 = Counts observed by the detector with no object intervening between it and the source (unobstructed counts).

Now suppose the pipe is filled with liquid alone ($\bar{\alpha} = 0$) and the measurement is repeated keeping the radial position of the ray unchanged. Then the countrate is,

$$I_l = I_0 e^{-(\bar{\mu}_l x + \bar{\mu}_p x_p)} \tag{A.5}$$

If a third measurement is taken along the same chordal position after emptying the pipe (ie. filling it with air),

$$I_g = I_0 e^{-(\bar{\mu}_g x + \bar{\mu}_p x_p)} \approx I_0 e^{-\bar{\mu}_p x_p} \tag{A.6}$$

To find an expression for the chord-integrated void fraction in terms of the count rates $I_{tp}, I_l \& I_g$, we perform the following algebraic steps.

$$\frac{I_{tp}}{I_l} = e^{-\bar{\mu}_l \bar{\alpha} x}$$

$$\frac{I_g}{I_l} = e^{-\bar{\mu}_l x}$$

and,

$$\frac{\ln\left(\frac{I_{tp}}{I_l}\right)}{\ln\left(\frac{I_g}{I_l}\right)} = \bar{\alpha} \tag{A.7}$$

Note the implicit assumption that the unobstructed count- rates seen by the detector when the three measurements were made, were the same.

A.2 Statistical Uncertainty in Chord-Averaged Void Fraction

The chord averaged void fraction in this work is calculated by

$$\bar{\alpha} = \frac{\ln(I_{tp}/I_l)}{\ln(I_g/I_l)} \tag{A.8}$$

where,

$$I_{tp} = N_{tp}/t_{tp}$$
$$I_l = N_l/t_l$$
$$I_g = N_g/t_g$$

and N_l, N_g and N_{tp} are the gamma counts observed along the same chord with liquid, gas and two-phase filling the pipe respectively. t_l, t_g and t_{tp} are the times (s) in which counts N_l, N_g and N_{tp} are collected.

Applying the error propogation formula to the above equation,

$$\sigma_{\bar{\alpha}}^2 = \left(\frac{\partial\bar{\alpha}}{\partial I_{tp}}\right)^2 \sigma_{Itp}^2 + \left(\frac{\partial\bar{\alpha}}{\partial I_l}\right)^2 \sigma_{Il}^2 + \left(\frac{\partial\bar{\alpha}}{\partial I_g}\right)^2 \sigma_{Ig}^2 \tag{A.9}$$

Evaluating the terms in the RHS of Eq. (A.9),
with ($1-\sigma$) confidence,
$\sigma_{Ntp} = \sqrt{N_{tp}}$
and assuming that there are no uncertainties in the measured times,

$$\sigma_{I_{tp}}^2 = \left(\frac{\partial I_{tp}}{\partial N_{tp}}\right)^2 \sigma_{N_{tp}}^2$$

$$= \left(\frac{\sqrt{N_{tp}}}{t_{tp}}\right)^2$$

$$= \frac{N_{tp}}{t_{tp}^2}$$

Similarly,

$$\sigma_{I_l}^2 = \frac{N_l}{t_l^2}$$

$$\sigma_{I_g}^2 = \frac{N_g}{t_g^2}$$

Also,

$$\left(\frac{\partial \bar{\alpha}}{\partial I_{tp}}\right) = \frac{1}{I_{tp} \ln(I_g/I_l)}$$

$$\left(\frac{\partial \bar{\alpha}}{\partial I_l}\right) = \frac{\ln(I_{tp}/I_g)}{I_l \left[\ln(I_g/I_l)\right]^2}$$

$$\left(\frac{\partial \bar{\alpha}}{\partial I_g}\right) = \frac{\ln(I_l/I_{tp})}{I_g \left[\ln(I_g/I_l)\right]^2}$$

Substituting in Eq. (A.9)

$$\sigma_{\bar{\alpha}}^2 = \frac{N_{tp}}{t_{tp}^2 I_{tp}^2}\left(\frac{1}{\ln(I_g/I_l)}\right)^2 + \frac{N_l}{t_l^2 I_l^2}\left(\frac{\ln(I_{tp}/I_g)}{\left[\ln(I_g/I_l)\right]^2}\right)^2 + \frac{N_g}{t_g^2 I_g^2}\left(\frac{\ln(I_l/I_{tp})}{\left[\ln(I_g/I_l)\right]^2}\right)^2$$

$$= \left(\frac{1}{\ln(I_g/I_l)}\right)^2 \left\{\frac{1}{N_{tp}} + \frac{1}{N_l}\left[\frac{\ln(I_{tp}/I_g)}{\ln(I_g/I_l)}\right]^2 + \frac{1}{N_g}\left[\frac{\ln(I_l/I_{tp})}{\ln(I_g/I_l)}\right]^2\right\}$$

$$= \frac{1}{\left[\ln(I_g/I_l)\right]^2}\left(\frac{1}{N_{tp}} + \frac{(\bar{\alpha}-1)^2}{N_l} + \frac{\bar{\alpha}^2}{N_g}\right)$$

Therefore,

$$\sigma_{\bar{\alpha}} = \frac{1}{\ln(I_g/I_l)}\left(\frac{1}{N_{tp}} + \frac{(\bar{\alpha}-1)^2}{N_l} + \frac{\bar{\alpha}^2}{N_g}\right)^{1/2}$$

A.3 Statistical Uncertainties in Local Values Calculated by CSI

Considering m number of rays, the CSI direct problem is written as, (see Chapter 2)

$$
\begin{bmatrix} S_{11} & S_{12} & . & . & S_{1m} \\ 0 & S_{22} & . & . & S_{2m} \\ . & . & . & . & . \\ . & . & . & . & . \\ 0 & . & . & 0 & S_{mm} \end{bmatrix} \begin{bmatrix} \alpha_1 \\ \alpha_2 \\ . \\ . \\ \alpha_m \end{bmatrix} = \begin{bmatrix} L_1 \bar{\alpha}_1 \\ L_2 \bar{\alpha}_2 \\ . \\ . \\ L_m \bar{\alpha}_m \end{bmatrix}
$$

where

$L_i = \sum_{j=1}^{m} S_{ij}$

Taking the equation for the kth ray

$$
S_{kk}\alpha_k + \sum_{j=k+1}^{m} S_{kj}\alpha_j = L_k \bar{\alpha}_k \tag{A.10}
$$

or,

$$
\alpha_k = \frac{1}{S_{kk}} \left(L_k \bar{\alpha}_k - \sum_{j=k+1}^{m} S_{kj}\alpha_j \right) \tag{A.11}
$$

Assuming that there are no uncertainties in the lengths S_{kj} and L_i and applying the error propogation formula to A.11,

$$
\sigma_{\alpha k}^2 = \left(\frac{\partial \alpha_k}{\partial \bar{\alpha}_k} \right)^2 \sigma_{\bar{\alpha} k}^2 + \sum_{j=k+1}^{m} \left(\frac{\partial \alpha_k}{\partial \alpha_j} \right)^2 \sigma_{\alpha j}^2 \tag{A.12}
$$

From Eq.(A.11),

$$
\frac{\partial \alpha_k}{\partial \bar{\alpha}_k} = \frac{L_k}{S_{kk}}
$$

and

$$\frac{\partial \alpha_k}{\partial \alpha_j} \;=\; -\frac{S_{kj}}{S_{kk}}$$

Substituting in Eq.(A.12)

$$\sigma^2_{\alpha k} \;=\; \frac{1}{S^2_{kk}}\left(L^2_k\sigma^2_{\bar\alpha k} + \sum_{j=k+1}^{m} S^2_{kj}\sigma^2_{\alpha j}\right)$$

That is, for $k = (m-1), (m-2)\ldots 1$,

$$\sigma_{\alpha k} = \frac{1}{S_{kk}}\left(L^2_k\sigma^2_{\bar\alpha k} + \sum_{j=k+1}^{m} S^2_{kj}\sigma^2_{\alpha j}\right)^{1/2} \tag{0.1}$$

For $k = m$, since $L_m = S_{mm}$

$$\sigma_{\alpha m} = \sigma_{\bar\alpha m}, \tag{0.2}$$

where,

$\sigma_{\alpha k} = (1\text{-}\sigma)$ uncertainty in the the local value calculated in the k'th zone.

$\sigma_{\bar\alpha k} = (1\text{-}\sigma)$ uncertainty of length-averaged value at the k'th chord.

and,

$m = $ Number of rays $=$ Number of zones.

A.4 Statistical Uncertainty in Cross sectional Average

The cross sectionally averaged void fraction is given by

$$\langle \alpha \rangle = \frac{\sum_{i=1}^{m} a_i \alpha_i}{A} \tag{A.14}$$

where,

a_i = Area of the ith zone and

$A = \sum_{i=1}^{m} a_i$ (the area of cross section)

Applying error propogation formula to Eq.(A.14) and simplifying

$$\sigma_{\langle \alpha \rangle} = \frac{\left(\sum_{i=1}^{m} a_i^2 \sigma_{\alpha i}^2 \right)^{1/2}}{A} \tag{A.15}$$

$$\tag{A.16}$$

Table B.1: Flow and Pressure gauge readings

Major Case Name	Distance above mixer (m)	Nitrogen flow rate (lpm)	MHD flow-meter OCV $\times 10^{-3}$V [1]	Pressure gauge readings [2] $(kg/cm^2\ g)$				
				P_r	P_1	P_2	P_3	P_4
BN400 & BS400	1.1	40	23.25	5.41	4.52	2.95	1.57	2.02
BN600 & BS600	1.1	60	23.67	5.21	4.37	2.84	1.10	1.92
TN400 & TS400	2.8	40	21.90	5.39	4.55	2.97	1.19	2.04
TN600 & TS600	2.8	60	22.42	5.17	4.31	2.84	1.11	1.93
TS800	2.8	80	27.41	5.05	4.32	3.34	1.11	1.95
TS200	2.8	20	16.76	5.65	4.79	3.13	1.29	2.22
TS100	2.8	10	14.16	5.75	4.89	3.24	1.30	2.28

CASE BN400

Elevation 1.1 m above mixer (bottom)

Half North

Nitrogen Flow rate 40 lpm

Number of rays 10

Distance from Centre (mm)	Air		Mercury		Two-phase Mixture	
	Counts	Time (s)	Counts	Time (s)	Counts	Time (s)
.0	7734	15	3398	1000	3001	297
4.0	7643	15	3511	1000	3005	283
8.0	7638	15	3406	900	3000	252
12.0	7794	15	3769	900	3003	238
16.0	7588	15	3281	600	3002	200
20.0	7838	15	3215	500	3005	182
24.0	7620	15	3714	400	3005	179
28.0	7459	15	3380	250	3008	149
32.0	7080	15	3575	150	3028	100
36.0	6119	15	4941	100	3016	54

Table B.2: Data for case BN400

CASE BS400

Elevation 1.1 m above mixer (bottom)

Half South

Nitrogen Flow rate 40 lpm

Number of rays 19

Distance from Centre (mm)	Air		Mercury		Two-phase Mixture	
	Counts	Time (s)	Counts	Time (s)	Counts	Time (s)
.0	7734	15	3398	1000	3001	297
2.0	7681	15	3184	900	3009	284
4.0	7662	15	3105	900	3009	244
6.0	7665	15	3336	900	3051	280
8.0	15475	30	3279	900	3003	263
10.0	15595	30	4616	1180	3004	278
12.0	15343	30	3843	900	3002	255
14.0	15512	30	3843	820	3012	242
16.0	15546	30	3189	650	3006	246
18.0	15453	30	3257	560	3016	277
20.0	15632	30	3187	450	3005	226
22.0	15390	30	4084	513	3015	195
24.0	15550	30	3283	350	3031	182
26.0	15422	30	3274	275	3019	123
28.0	15230	30	3239	200	3016	137
30.0	15057	30	3079	150	3020	114
32.0	14726	30	3164	100	3009	85
34.0	14397	30	3653	80	2099	39
36.0	13244	30	4182	60	3075	40

Table B.3: Data for case BS400

CASE BN600

Elevation 1.1 m above mixer (bottom)

Half North

Nitrogen Flow rate 60 lpm

Number of rays 19

Distance from Centre (mm)	Air		Mercury		Two-phase Mixture	
	Counts	Time (s)	Counts	Time (s)	Counts	Time (s)
.0	7734	15	3398	1000	3004	164
2.0	7643	15	3386	1000	3010	169
4.0	7643	15	3511	1000	3051	159
6.0	7731	15	4313	1200	3001	163
8.0	7638	15	3406	900	3014	155
10.0	7746	15	3633	900	3015	148
12.0	7794	15	3769	900	3196	141
14.0	7754	15	3592	800	3020	152
16.0	7588	15	3281	600	3037	175
18.0	7628	15	3763	637	3015	151
20.0	7838	15	3215	500	3014	147
22.0	7602	15	3159	400	3009	155
24.0	7620	15	3714	400	3016	127
26.0	7493	15	3523	300	3013	128
28.0	7459	15	3380	250	3042	127
30.0	7164	15	3441	200	3016	110
32.0	7080	15	3575	150	3065	97
34.0	6733	15	3269	100	3035	81
36.0	6119	15	4941	100	4264	79

Table B.4: Data for case BN600

CASE BS600

Elevation 1.1 m from mixer (Bottom)

Half South

Nitrogen Flow rate 60 lpm

Number of rays 19

Distance from Centre (mm)	Air		Mercury		Two-phase Mixture	
	Counts	Time (s)	Counts	Time (s)	Counts	Time (s)
.0	7734	15	3398	1000	3004	164
2.0	7681	15	3184	900	3006	162
4.0	7662	15	3105	900	3006	175
6.0	7665	15	3336	900	3010	167
8.0	15475	30	3279	900	3006	190
10.0	15595	30	4616	1180	3006	199
12.0	15343	30	3843	900	3022	152
14.0	15512	30	3843	820	3049	171
16.0	15546	30	3189	650	3038	160
18.0	15453	30	3257	560	3028	151
20.0	15632	30	3187	450	3029	159
22.0	15390	30	4084	513	3017	156
24.0	15550	30	3283	350	3050	155
26.0	15422	30	3274	275	3074	130
28.0	15230	30	3239	200	3040	137
30.0	15057	30	3079	150	3116	109
32.0	14726	30	3164	100	3083	79
34.0	14397	30	3653	80	3111	58
36.0	13244	30	4182	60	3221	39

Table B.5: Data for case BS600

CASE TN400

Elevation 2.8 m above mixer (Top)

Half North

Nitrogen Flow rate 40 lpm

Number of rays 10

Distance from Centre (mm)	Air		Mercury		Two-phase Mixture	
	Counts	Time (s)	Counts	Time (s)	Counts	Time (s)
.0	19195	30	8026	3346	4132	250
4.0	19413	30	4930	2030	3010	158
8.0	18665	30	3000	1183	3002	182
12.0	18829	30	3072	1000	3011	169
16.0	19265	30	3002	834	3011	158
20.0	18582	30	3069	650	3007	156
24.0	18224	30	3002	459	3019	111
28.0	17198	30	3005	307	3025	128
32.0	15308	30	3003	171	3006	105
36.0	13395	30	3026	73	3039	67

Table B.6: Data for case TN400

CASE TS400

Elevation 2.8 m above mixer (Top)

Half South

Nitrogen Flow rate 40 lpm

Number of rays 19

Distance from Centre (mm)	Air		Mercury		Two-phase Mixture	
	Counts	Time (s)	Counts	Time (s)	Counts	Time (s)
.0	19195	30	8026	3346	4132	250
2.0	20125	30	3004	1213	3004	174
4.0	20581	30	3472	1331	3086	159
6.0	20235	30	3020	1095	3029	180
8.0	19715	30	3010	1066	4361	250
10.0	20122	30	3004	985	3001	144
12.0	20353	30	3669	1030	3002	185
14.0	20846	30	4217	1030	3001	169
16.0	20047	30	3042	673	3010	166
18.0	19579	30	5208	1030	3012	185
20.0	19298	30	3048	526	3002	131
22.0	19427	30	3132	429	3009	161
24.0	19165	30	3030	362	3021	148
26.0	18344	30	3007	289	3044	156
28.0	17695	30	3042	223	5771	255
30.0	16627	30	3012	163	3003	104
32.0	15548	30	3017	106	3005	94
34.0	14380	30	3026	72	3011	68
36.0	12004	30	3034	47	3027	45

Table B.7: Data for case TS400

CASE TN600

Elevation 2.8 m above mixer (Top)

Half North

Nitrogen Flow rate 60 lpm

Number of rays 10

Distance from Centre (mm)	Air		Mercury		Two-phase Mixture	
	Counts	Time (s)	Counts	Time (s)	Counts	Time (s)
.0	19195	30	8026	3346	3001	104
4.0	19413	30	4930	2030	3018	99
8.0	18665	30	3000	1183	3022	95
12.0	18829	30	3072	1000	3003	101
16.0	19265	30	3002	834	3041	110
20.0	18582	30	3069	650	3011	107
24.0	18224	30	3002	459	3008	100
28.0	17198	30	3005	307	3060	94
32.0	15308	30	3003	171	3011	82
36.0	13395	30	3026	73	3017	59

Table B.8: Data for case TN600

CASE TS600

Elevation 2.8 m above mixer (Top)

Half South

Nitrogen Flow rate 60 lpm

Number of rays 10

Distance from Centre (mm)	Air		Mercury		Two-phase Mixture	
	Counts	Time (s)	Counts	Time (s)	Counts	Time (s)
.0	19195	30	8026	3346	3001	104
4.0	20581	30	3472	1331	3003	101
8.0	19715	30	3010	1066	3067	107
12.0	20353	30	3669	1030	3010	109
16.0	20047	30	3042	673	3019	111
20.0	19298	30	3048	526	3001	119
24.0	19165	30	3030	362	3005	77
28.0	17695	30	3042	223	3014	95
32.0	15548	30	3017	106	3017	89
36.0	12004	30	3034	47	3013	45

Table B.9: Data for case TS600

CASE TS800

Elevation 2.8 m above mixer (Top)

Half South

Nitrogen Flow rate 80 lpm

Number of rays 6

Distance from Centre (mm)	Air		Mercury		Two-phase Mixture	
	Counts	Time (s)	Counts	Time (s)	Counts	Time (s)
.0	19195	30	8026	3346	3045	80
7.0	19975	30	3098	1110	3024	75
14.0	20846	30	4217	1030	3038	81
21.0	19362	30	3097	473	3035	85
28.0	17695	30	3042	223	3020	88
35.0	13162	30	3100	70	3016	63

Table B.10: Data for case TS800

CASE TS200

Elevation 2.8 m above mixer (Top)

Half South

Nitrogen Flow rate 20 lpm

Number of rays 6

Distance from Centre (mm)	Air		Mercury		Two-phase Mixture	
	Counts	Time (s)	Counts	Time (s)	Counts	Time (s)
.0	19195	30	8026	3346	3019	336
7.0	19975	30	3098	1110	3015	319
14.0	20846	30	4217	1030	3014	289
21.0	19362	30	3097	473	3004	240
28.0	17695	30	3042	223	3007	174
35.0	13162	30	3100	70	3023	63

Table B.11: Data for case TS200

CASE TS100

Elevation 2.8 m above mixer (Top)

Half South

Nitrogen Flow rate 10 lpm

Number of rays 6

Distance from Centre (mm)	Air		Mercury		Two-phase Mixture	
	Counts	Time (s)	Counts	Time (s)	Counts	Time (s)
.0	19195	30	8026	3346	3026	489
7.0	19975	30	3098	1110	3001	485
14.0	20846	30	4217	1030	3001	427
21.0	19362	30	3097	473	3004	337
28.0	17695	30	3042	223	3014	192
35.0	13162	30	3100	70	3025	58

Table B.12: Data for case TS100

Table B.13: TWO-PHASE READINGS FOR MINOR CASES OF BS600

Distance from centre (mm)	BS603		BS606		BS601		BS602	
	Counts	Time (s)	Counts	Time (s)	Counts	Time (s)	Counts	Time (s)
.0	304	16	614	33	1014	55	2008	112
2.0	412	28	625	35	1032	54	2008	113
4.0	315	16	627	31	1008	58	2003	112
6.0	316	17	626	34	1002	58	2029	118
8.0	301	18	609	39	1028	68	2009	129
10.0	303	23	605	46	1032	71	2014	131
12.0	302	19	633	39	1027	58	2151	96
14.0	300	19	601	36	1002	56	2010	115
16.0	304	18	601	36	1008	57	2002	102
18.0	304	13	603	29	1001	51	2004	104
20.0	305	16	605	31	1016	54	2026	109
22.0	300	13	600	28	1023	48	2056	106
24.0	300	14	600	27	1000	51	2002	104
26.0	300	15	610	26	1000	40	2010	83
28.0	300	11	600	26	1009	43	2006	90
30.0	300	11	609	21	1000	34	2000	71
32.0	300	7	600	15	1006	25	2000	51
34.0	300	6	600	11	1016	19	2000	35
36.0	300	4	600	7	1000	12	2000	24

Note:

Air & Mercury readings and other parameters are the same as that of BS600.

Table B.14: TWO-PHASE READINGS FOR MINOR CASES OF TN400

Distance from centre (mm)	TN403		TN406		TN401		TN402	
	Counts	Time (s)	Counts	Time (s)	Counts	Time (s)	Counts	Time (s)
.0	300	18	600	37	1000	60	2000	122
4.0	470	19	606	27	1013	52	2012	102
8.0	305	15	605	33	1009	62	2014	113
12.0	309	18	629	34	1002	54	2007	109
16.0	309	13	610	29	1003	48	2007	98
20.0	306	20	602	36	1014	59	2018	112
24.0	303	15	606	29	1012	42	2010	70
28.0	320	13	608	27	1014	44	2020	85
32.0	303	13	616	23	1021	37	2019	73
36.0	314	8	623	15	1017	24	2010	45

Note:

Air & Mercury readings and other parameters are the same as that of TN400.

Table B.15: TWO-PHASE READINGS FOR THE MINOR CASES OF TS400

Distance from centre (mm)	TS403		TS406		TS401		TS402	
	Counts	Time (s)	Counts	Time (s)	Counts	Time (s)	Counts	Time (s)
.0	301	18.2	605	36	1010	61	2012	122
2.0	304	14	642	29	1000	48	2012	110
4.0	370	25	614	40	1003	59	2011	116
6.0	321	21	610	36	1006	60	2011	122
8.0	307	18	615	35	1008	58	2015	115
10.0	304	20	614	36	1026	59	2007	97
12.0	303	19	660	40	1000	60	2003	122
14.0	379	22	602	35	1006	64	2004	114
16.0	332	15	615	32	1004	60	2017	112
18.0	319	18	614	36	1004	65	2012	128
20.0	336	19	603	30	1006	51	2050	94
22.0	304	17	604	34	1008	53	2012	107
24.0	306	13	626	30	1015	48	2009	95
26.0	312	18	660	36	1015	52	2002	105
28.0	315	14	640	29	1004	45	2025	91
30.0	311	12	613	22	1005	33	2025	62
32.0	311	9	610	18	1004	31	2032	63
34.0	324	7	617	12	1009	24	2014	47
36.0	323	5	632	9	1021	15	2018	31

Note:

Air & Mercury readings and other parameters are the same as that of TS400.

Appendix C

TABULATED RESULTS

CASE BN400

Elevation 1.1 m above mixer (bottom)

Half North

Nitrogen Flow rate

Inner radius of the pipe 38.95 mm

Number of rays   10

Table C.1: Count rates and chord-averaged void fraction for BN400

Distance from centre (mm)	Count rates (s^{-1})			Length Averaged void fraction
	Air	Mercury	Two-Phase mixture	
.0	515.60	3.40	10.10	0 .2170
4.0	509.53	3.51	10.62	0 .2223
8.0	509.20	3.78	11.90	0 .2338
12.0	519.60	4.19	12.62	0 .2288
16.0	505.87	5.47	15.01	0 .2230
20.0	522.53	6.43	16.51	0 .2144
24.0	508.00	9.28	16.79	0 .1480
28.0	497.27	13.52	20.19	0 .1112
32.0	472.00	23.83	30.28	0 .0802
36.0	407.93	49.41	55.85	0 .0581

Table C.2: Void Fraction Distribution (CSI) for BN400

Zone Inner & Outer Radii (mm)		Void fraction $\alpha(r)$	$1-\sigma$ Statistical Uncertainty
.0	– 4.0	0.1819	0.0783
4.0	– 8.0	0.2214	0.0400
8.0	– 12.0	0.2996	0.0288
12.0	– 16.0	0.2963	0.0288
16.0	– 20.0	0.3046	0.0196
20.0	– 24.0	0.3408	0.0167
24.0	– 28.0	0.2006	0.0143
28.0	– 32.0	0.1372	·0.0131
32.0	– 36.0	0.0878	0.0114
36.0	– 38.95	0.0581	0.0107

Cross sectional average, $\langle \alpha \rangle = 0.1885 \pm 0.0050$

Table C.3: Void Fraction Distribution (LSS & C-CSI) for BN400

Zone Inner & Outer Radii (mm)		Void Fraction $\alpha(r)$	
		LSS	C-CSI
.0	– 8.00	0.2100	0.2115
8.0	– 16.0	0.2958	0.2977
16.0	– 24.0	0.3280	0.3245
24.0	– 32.0	0.1698	0.1667
32.0	– 39.0	0.0707	0.0745
Cross sectional average, $\langle \alpha \rangle$		0.1886	.1885

CASE BS400

Elevation 1.1 m above mixer (bottom)

Half South

Nitrogen Flow rate 40 lpm

Number of rays 19

Table C.4: Count rates and chord-averaged void fraction for BS400

Distance from centre (mm)	Count rates (s^{-1})			Length Averaged void fraction
	Air	Mercury	Two-Phase mixture	
.0	515.60	3.40	10.10	0 .2170
2.0	512.06	3.53	10.59	0 .2205
4.0	510.80	3.45	12.33	0 .2549
6.0	511.00	3.71	10.90	0 .2189
8.0	515.83	3.64	11.42	0 .2306
10.0	519.83	3.91	10.81	0 .2078
12.0	511.43	4.27	11.77	0 .2119
14.0	517.07	4.69	12.45	0 .2077
16.0	518.20	4.91	12.22	0 .1958
18.0	515.10	5.82	10.89	0 .1398
20.0	521.07	7.08	13.30	0 .1465
22.0	513.00	7.96	15.46	0 .1593
24.0	518.33	9.38	16.65	0 .1431
26.0	514.07	11.91	24.54	0 .1921
28.0	507.67	16.19	22.01	0 .0891
30.0	501.90	20.53	26.49	0 .0798
32.0	490.87	31.64	35.40	0 .0410
34.0	479.90	45.66	53.82	0 .0699
36.0	441.47	69.70	76.88	0 .0531

Table C.5: Void Fraction Distribution (CSI) for BS400

Zone Inner & Outer Radii (mm)	Void fraction $\alpha(r)$	$1-\sigma$ Statistical Uncertainty
.0 – 2.0	0.0996	0. 209
2.0 – 4.0	0.1058	0.1075
4.0 – 6.0	0.5891	0.0774
6.0 – 8.0	0.2670	0.0622
8.0 – 10.0	0.4107	0.0523
10.0 – 12.0	0.2707	0.0452
12.0 – 14.0	0.3227	0.0406
14.0 – 16.0	0.3500	0.0367
16.0 – 18.0	0.3808	0.0338
18.0 – 20.0	0.1287	0.0315
20.0 – 22.0	0.1458	0.0292
22.0 – 24.0	0.2111	0.0264
24.0 – 26.0	0.1378	0.0251
26.0 – 28.0	0.3922	0.0234
28.0 – 30.0	0.1190	0.0227
30.0 – 32.0	0.1186	0.0213
32.0 – 34.0	0.0179	0.0257
34.0 – 36.0	0.0801	0.0997
36.0 – 38.95	0.0531	0.0125

Cross sectional average, $\langle \alpha \rangle = 0.1731 \pm 0.0065$

Table C.6: Void Fraction Distribution (LSS & C-CSI) for BS400

Zone Inner & Outer Radii (mm)	Void Fraction $\alpha(r)$	
	LSS	C-CSI
.0 – 4.00	0.1387	0.1002
4.0 – 8.0	0.4161	0.4012
8.0 – 12.0	0.3245	0.3337
12.0 – 16.0	0.3459	0.3373
16.0 – 20.0	0.2456	0.2478
20.0 – 24.0	0.1559	0.1800
24.0 – 28.0	0.2710	0.2699
28.0 – 32.0	0.1255	0.1188
32.0 – 39.0	0.0534.	0.0513
Cross sectional average, $\langle \alpha \rangle$	0.1730	0.1731

CASE BN600

Elevation 1.1 m above mixer (bottom)

Half North

Nitrogen Flow rate 60 lpm

Inner radius of the pipe 38.95 mm

Number of rays 19

Table C.7: Count rates and chord-averaged void fraction for BN600

Distance from centre (mm)	Count rates (s^{-1})			Length Averaged void fraction
	Air	Mercury	Two-Phase mixture	
.0	515.60	3.40	18.32	0 .3354
2.0	509.53	3.39	17.81	0 .3311
4.0	509.53	3.51	19.19	0 .3412
6.0	515.40	3.59	18.41	~0 .3290
8.0	509.20	3.78	19.45	0 .3339
10.0	516.40	4.04	20.37	0 .3337
12.0	519.60	4.19	22.67	0 .3503
14.0	516.93	4.49	19.87	0 .3134
16.0	505.87	5.47	17.35	0 .2551
18.0	508.53	5.91	19.97	0 .2734
20.0	522.53	6.43	20.50	0 .2637
22.0	506.80	7.90	19.41	0 .2161
24.0	508.00	9.28	23.75	0 .2347
26.0	499.53	11.74	23.54	0 .1854
28.0	497.27	13.52	23.95	0 .1586
30.0	477.60	17.20	27.42	0 .1402
32.0	472.00	23.83	31.60	0 .0944
34.0	448.87	32.69	37.47	0 .0521
36.0	407.93	49.41	53.97	0 .0419

Table C.8: Void Fraction Distribution (CSI) for BN600

Zone Inner & Outer Radii (mm)	Void fraction $\alpha(r)$	$1-\sigma$ Statistical Uncertainty
.0 – 2.0	0.4667	0.1959
2.0 – 4.0	0.3610	0.1000
4.0 – 6.0	0.5103	0.0722
6.0 – 8.0	0.3986	0.0577
8.0 – 10.0	0.4444	0.0492
10.0 – 12.0	0.4488	0.0428
12.0 – 14.0	0.6495	0.0376
14.0 – 16.0	0.5620	0.0344
16.0 – 18.0	0.2768	0.0320
18.0 – 20.0	0.3944	0.0282
20.0 – 22.0	0.4245	0.0268
22.0 – 24.0	0.2532	0.0253
24.0 – 26.0	0.3824	0.0231
26.0 – 28.0	0.2679	0.0219
28.0 – 30.0	0.2215	0.0202
30.0 – 32.0	0.2142	0.0188
32.0 – 34.0	0.1363	0.0175
34.0 – 36.0	0.0583	0.0162
36.0 – 38.95	0.0419	0.0097

Cross sectional average, $\langle\alpha\rangle = 0.2593 \pm 0.0058$

Table C.9: Void Fraction Distribution (LSS & C-CSI) for BN600

Zone Inner & Outer Radii (mm)	Void Fraction $\alpha(r)$	
	LSS	C-CSI
.0 – 4.00	0.4054	0.3874
4.0 – 8.0	0.4455	0.4452
8.0 – 12.0	0.4487	0.4468
12.0 – 16.0	0.5970	0.6026
16.0 – 20.0	0.3445	0.3389
20.0 – 24.0	0.3463	0.3350
24.0 – 28.0	0.3169	0.3230
28.0 – 32.0	0.2210	0.2177
32.0 – 39.0	0.0692	0.0718
Cross sectional average, $\langle\alpha\rangle$	0.2599	0.2593

CASE BS600

Elevation 1.1 m above mixer (bottom)

Half South

Nitrogen Flow rate 60 lpm

Inner radius of pipe 38.95 mm

Number of rays 19

Table C.10: Count rates and chord-averaged void fraction for BS600

Distance from centre (mm)	Count rates (s^{-1})			Length Averaged void fraction
	Air	Mercury	Two-Phase mixture	
.0	515.60	3.40	18.32	0 .3354
2.0	512.07	3.54	18.56	0 .3331
4.0	510.80	3.45	17.18	0 .3212
6.0	511.00	3.71	18.02	0 .3211
8.0	515.83	3.64	15.82	0 .2965
10.0	519.83	3.91	15.11	0 .2763
12.0	511.43	4.27	19.88	0 .3214
14.0	517.07	4.69	17.83	0 .2841
16.0	518.20	4.91	18.99	0 .2904
18.0	515.10	5.82	20.05	0 .2761
20.0	521.07	7.08	19.05	0 .2302
22.0	513.00	7.96	19.34	0 .2131
24.0	518.33	9.38	19.68	0 .1847
26.0	514.07	11.91	23.65	0 .1822
28.0	507.67	16.19	22.19	0 .0914
30.0	501.90	20.53	28.59	0 .1036
32.0	490.87	31.64	39.03	0 .0765
34.0	479.90	45.66	53.64	0 .0684
36.0	441.47	69.70	82.59	0 .0919

Table C.11: Void Fraction Distribution (CSI) for BS600

Zone Inner & Outer Radii (mm)	Void fraction $\alpha(r)$	1-σ Statistical Uncertainty
.0 – 2.0	0.5979	0.2023
2.0 – 4.0	0.5960	0.1037
4.0 – 6.0	0.4861	0.0749
6.0 – 8.0	0.5587	0.0601
8.0 – 10.0	0.4117	0.0506
10.0 – 12.0	0.2191	0.0437
12.0 – 14.0	0.5567	0.0399
14.0 – 16.0	0.3782	0.0354
16.0 – 18.0	0.4627	0.0325
18.0 – 20.0	0.4854	0.0301
20.0 – 22.0	0.3454	0.0282
22.0 – 24.0	0.3310	0.0258
24.0 – 26.0	0.2661	0.0245
26.0 – 28.0	0.3450	0.2302
28.0 – 30.0	0.0873	0.0223
30.0 – 32.0	0.1371	0.0207
32.0 – 34.0	0.0786	0.0198
34.0 – 36.0	0.0542	0.0177
36.0 – 38.95	0.0919	0.0122

Cross sectional average, $\langle \alpha \rangle = 0.2426 \pm 0.0062$

Table C.12: Void Fraction Distribution (LSS & C-CSI) for BS600

Zone Inner & Outer Radii (mm)	Void Fraction $\alpha(r)$	
	LSS	C-CSI
.0 – 4.00	0.5900	0.5965
4.0 – 8.0	0.5418	0.5284
8.0 – 12.0	0.3207	0.3058
12.0 – 16.0	0.4542	0.4610
16.0 – 20.0	0.4682	0.4747
20.0 – 24.0	0.3343	0.3379
24.0 – 28.0	0.3036	0.3071
28.0 – 32.0	0.1158	0.1130
32.0 – 39.0	0.0783	0.0776
Cross sectional average, $\langle \alpha \rangle$	0.2424	0.2426

CASE TN400

Elevation 2.8m above mixer (Top)

Half North

Nitrogen Flow rate 40 lpm

Inner radius of pipe 38.95 mm

Number of rays   10

Table C.13: Count rates and chord-averaged void fraction for TN400

Distance from centre (mm)	Count rates (s^{-1})			Length Averaged void fraction
	Air	Mercury	Two-Phase mixture	
.0	639.83	2.40	16.53	0 .3455
4.0	647.10	2.43	19.05	0 .3688
8.0	622.17	2.54	16.49	0 .3403
12.0	627.63	3.07	17.82	0 .3304
16.0	642.17	3.60	19.06	0 .3215
20.0	619.40	4.72	19.28	0 .2885
24.0	607.47	6.54	27.20	0 .3145
28.0	573.27	9.79	23.63	0 .2166
32.0	510.27	17.56	28.63	0 .1450
36.0	446.50	41.45	45.36	0 .0379

Table C.14: Void Fraction Distribution (CSI) for TN400

Zone Inner & Outer Radii (mm)	Void fraction $\alpha(r)$	1-σ Statistical Uncertainty
.0 – 4.0	0.2899	0.0634
4.0 – 8.0	0.5638	0.0340
8.0 – 12.0	0.4263	0.0252
12.0 – 16.0	0.4072	0.0202
16.0 – 20.0	0.4121	0.0169
20.0 – 24.0	0.3167	0.0147
24.0 – 28.0	0.4547	0.0127
28.0 – 32.0	0.2837	0.0114
32.0 – 36.0	0.1822	0.0103
36.0 – 38.95	0.0379	0.0106

Cross sectional average, $\langle \alpha \rangle = 0.2947 \pm 0.0048$

Table C.15: Void Fraction Distribution (LSS & C-CSI) for TN400

Zone Inner & Outer Radii (mm)	Void Fraction $\alpha(r)$	
	LSS	C-CSI
.0 – 8.00	0.4857	0.4953
8.0 – 16.0	0.4258	0.4152
16.0 – 24.0	0.3706	0.3596
24.0 – 32.0	0.3679	0.3631
32.0 – 39.0	0.1046	0.1175
Cross sectional average, $\langle \alpha \rangle$	0.2952	0.2947

CASE TS400

Elevation 2.8 above mixer (top)

Half South

Nitrogen Flow rate 40 lpm

Inner radius of pipe 38.95 mm

Number of rays 19

Table C.16: Count rates and chord-averaged void fraction for TS400

Distance from centre (mm)	Count rates (s^{-1})			Length Averaged void fraction
	Air	Mercury	Two-Phase mixture	
.0	639.83	2.40	16.53	0 .3455
2.0	670.83	2.48	17.26	0 .3466
4.0	686.03	2.61	19.41	0 .3602
6.0	674.50	2.76	16.83	0 .3289
8.0	657.17	2.82	17.44	0 .3341
10.0	670.73	3.05	20.84	0 .3563
12.0	678.43	3.56	16.23	0 .2889
14.0	694.87	4.09	17.76	0 .2858
16.0	668.23	4.52	18.13	0 .2781
18.0	652.63	5.06	16.28	0 .2406
20.0	643.27	5.79	22.92	0 .2919
22.0	647.57	7.30	18.69	0 .2096
24.0	638.83	8.37	20.41	0 .2056
26.0	611.47	10.40	19.51	0 .1544
28.0	589.83	13.64	22.63	0 .1344
30.0	554.23	18.48	28.88	0 .1312
32.0	518.27	28.46	31.97	0 .0400
34.0	479.33	42.03	44.28	0 .0214
36.0	400.13	64.55	67.27	0 .0226

Table C.17: Void Fraction Distribution (CSI) for TS400

Zone Inner & Outer Radii (mm)		Void fraction $\alpha(r)$	1-σ Statistical Uncertainty
.0	– 2.0	0.4498	0.1821
2.0	– 4.0	0.4538	0.0959
4.0	– 6.0	0.6986	0.0689
6.0	– 8.0	0.4222	0.0559
8.0	– 10.0	0.4618	0.0461
10.0	– 12.0	0.7561	0.0414
12.0	– 14.0	0.3949	0.0370
14.0	– 16.0	0.4140	0.0333
16.0	– 18.0	0.4353	0.0301
18.0	– 20.0	0.2431	0.0279
20.0	– 22.0	0.5699	0.0265
22.0	– 24.0	0.2985	0.0251
24.0	– 26.0	0.3525	0.0233
26.0	– 28.0	0.2245	0.0221
28.0	– 30.0	0.1921	0.0196
30.0	– 32.0	0.2506	0.0202
32.0	– 34.0	0.0571	0.0199
34.0	– 36.0	0.0208	0.01880
36.0	– 38.95	0.0226	0.0139

Cross sectional average, $\langle\alpha\rangle = 0.2505 \pm 0.0061$

Table C.18: Void Fraction Distribution (LSS & C-CSI) for TS400

Zone Inner & Outer Radii (mm)		Void Fraction $\alpha(r)$	
		LSS	C-CSI
.0	– 4.00	0.4830	0.4528
4.0	– 8.0	0.5212	0.5374
8.0	– 12.0	0.6128	0.6237
12.0	– 16.0	0.4272	0.4052
16.0	– 20.0	0.3511	0.3339
20.0	– 24.0	0.4284	0.4280
24.0	– 28.0	0.2721	0.2860
28.0	– 32.0	0.2196	0.2223
32.0	– 39.0	0.0313	0.0313
Cross sectional average, $\langle\alpha\rangle$		0.2507	0.2505

CASE TN600

Elevation 2.8 m above mixer (top)

Half North

Nitrogen Flow rate 60 lpm

Inner radius of pipe 38.95 mm

Number of rays 10

Table C.19: Count rates and chord-averaged void fraction for TN600

Distance from centre (mm)	Count rates (s^{-1})		Two-Phase mixture	Length Averaged void fraction
	Air	Mercury		
.0	639.83	2.40	28.86	0 .4453
4.0	647.10	2.43	30.48	0 .4530
8.0	622.17	2.54	31.81	0 .4596
12.0	627.63	3.07	29.73	0 .4267
16.0	642.17	3.60	27.65	0 .3933
20.0	619.40	4.72	28.14	0 .3660
24.0	607.47	6.54	30.08	0 .3367
28.0	573.27	9.79	32.55	0 .2952
32.0	510.27	17.56	36.72	0 .2189
36.0	446.50	41.45	51.14	0 .0883

Table C.20: Void Fraction Distribution (CSI) for TN600

Zone Inner & Outer Radii (mm)		Void fraction $\alpha(r)$	$1-\sigma$ Statistical Uncertainty
.0	– 4.0	0.4790	0.0642
4.0	– 8.0	0.5604	0.0330
8.0	– 12.0	0.6605	0.0242
12.0	– 16.0	0.5733	0.0195
16.0	– 20.0	0.4959	0.1636
20.0	– 24.0	0.4519	0.0142
24.0	– 28.0	0.4164	0.0125
28.0	– 32.0	0.3690	0.0110
32.0	– 36.0	0.2642	0.0094
36.0	– 38.95	0.0883	0.0103

Cross sectional average, $\langle\alpha\rangle = 0.3751 \pm 0.0046$

Table C.21: Void Fraction Distribution (LSS & C-CSI) for TN600

Zone Inner & Outer Radii (mm)		Void Fraction $\alpha(r)$	
		LSS	C-CSI
.0	– 8.00	0.5467	0.5401
8.0	– 16.0	0.6152	0.6096
16.0	– 24.0	0.4728	0.4717
24.0	– 32.0	0.3984	0.3910
32.0	– 39.0	0.1768	0.1853
Cross sectional average, $\langle\alpha\rangle$		0.3757	0.3751

Table C.23: Void Fraction Distribution (CSI) for TS600

Zone Inner & Outer Radii (mm)	Void fraction $\alpha(r)$	1-σ Statistical Uncertainty
.0 – 4.0	0.6875	0.0688
4.0 – 8.0	0.6377	0.0357
8.0 – 12.0	0.6396	0.0259
12.0 – 16.0	0.5432	0.0208
16.0 – 20.0	0.4852	0.0179
20.0 – 24.0	0.3455	0.0157
24.0 – 28.0	0.5565	0.0137
28.0 – 32.0	0.3517	0.0128
32.0 – 36.0	0.0742	0.0126
36.0 – 38.95	0.0200	0.0140

Cross sectional average, $\langle\alpha\rangle = 0.3355 \pm 0.0050$

Table C.24: Void Fraction Distribution (LSS & C-CSI) for TS600

Zone Inner & Outer Radii (mm)	Void Fraction $\alpha(r)$	
	LSS	C-CSI
.0 – 8.00	0.6650	0.6501
8.0 – 16.0	0.5950	0.5834
16.0 – 24.0	0.4194	0.4084
24.0 – 32.0	0.4457	0.4468
32.0 – 39.0	0.0388	0.0499
Cross sectional average, $\langle\alpha\rangle$	0.3360	0.3355

CASE TS800

Elevation 2.8 m above mixer (top)

Half South

Nitrogen Flow rate 80 lpm

Inner radius of pipe 38.95 mm

Number of rays 6

Table C.25: Count rates and chord-averaged void fraction for TS800

Distance from centre (mm)	Count rates (s^{-1})			Length Averaged void fraction
	Air	Mercury	Two-Phase mixture	
.0	639.83	2.40	38.06	0 .4948
7.0	665.83	2.79	40.32	0 .4878
14.0	694.87	4.09	37.51	0 .4314
21.0	645.40	6.55	35.71	0 .3695
28.0	589.83	13.64	34.32	0 .2449
35.0	438.73	44.29	47.87	0 .0340

CASE TS800

Elevation 2.8 m above mixer (top)

Half South

Nitrogen Flow rate 80 lpm

Inner radius of pipe 38.95 mm

Number of rays 6

Table C.25: Count rates and chord-averaged void fraction for TS800

Distance from centre (mm)	Count rates (s^{-1})			Length Averaged void fraction
	Air	Mercury	Two-Phase mixture	
.0	639.83	2.40	38.06	0 .4948
7.0	665.83	2.79	40.32	0 .4878
14.0	694.87	4.09	37.51	0 .4314
21.0	645.40	6.55	35.71	0 .3695
28.0	589.83	13.64	34.32	0 .2449
35.0	438.73	44.29	47.87	0 .0340

Table C.26: Void Fraction Distribution (CSI) for TS800

Zone Inner & Outer Radii (mm)			Void fraction $\alpha(r)$	1-σ Statistical Uncertainty
.0	–	7.0	0.6756	0.0314
7.0	–	14.0	0.6927	0.0165
14.0	–	21.0	0.5709	0.0118
21.0	–	28.0	0.4890	0.0098
28.0	–	35.0	0.3060	0.0084
35.0	–	38.95	0.0340	0.0109

Cross sectional average, $\langle \alpha \rangle = 0.3872 \pm 0.0047$

Table C.27: Void Fraction Distribution (LSS & C-CSI) for TS800

Zone Inner & Outer Radii (mm)			Void Fraction $\alpha(r)$	
			LSS	C-CSI
.0	–	14.00	0.6984	0.6884
14.0	–	28.0	0.5405	0.5231
28.0	–	39.0	0.1824	0.1976
Cross sectional average, $\langle \alpha \rangle$			0.3878	0.3872

CASE TS200

Elevation 2.8 m above mixer (top)

HALF South

Nitrogen Flow rate 20 lpm

Inner radius of pipe 38.95 mm

Number of rays 6

Table C.28: Count rates and chord-averaged void fraction for TS200

Distance from centre (mm)	Count rates (s^{-1})			Length Averaged void fraction
	Air	Mercury	Two-Phase mixture	
.0	639.83	2.40	8.99	0 .2364
7.0	665.83	2.79	9.45	0 .2228
14.0	694.87	4.09	10.43	0 .1821
21.0	645.40	6.55	12.52	0 .1411
28.0	589.83	13.64	17.28	0 .0628
35.0	438.73	44.29	47.98	0 .0350

Table C.29: Void Fraction Distribution (CSI) for TS200

Zone Inner & Outer Radii (mm)		Void fraction $\alpha(r)$	1-σ Statistical Uncertainty
.0	– 7.0	0.3956	0.0336
7.0	– 14.0	0.3590	0.0181
14.0	– 21.0	0.2655	0.0128
21.0	– 28.0	0.2047	0.0107
28.0	– 35.0	0.0708	0.0091
35.0	– 38.95	0.0350	0.0109

Cross sectional average, $\langle \alpha \rangle = 0.1640 \pm 0.0051$

Table C.30: Void Fraction Distribution (LSS & C-CSI) for TS200

Zone Inner & Outer Radii (mm)		Void Fraction $\alpha(r)$	
		LSS	C-CSI
.0	- 14.00	0.3770	0.3682
14.0	- 28.0	0.2326	0.2300
28.0	- 39.0	0.0527	0.0566
Cross sectional average, $\langle \alpha \rangle$		0.1643	0.1640

CASE TS100

Elevation 2.8 m above mixer (top)

Half South

Nitrogen Flow rate 10 lpm

Inner radius of pipe 38.95 mm

Number of rays 6

Table C.31: Count rates and chord-averaged void fraction for TS100

Distance from centre (mm)	Count rates (s^{-1})		Two-Phase mixture	Length Averaged void fraction
	Air	Mercury		
.0	639.83	2.40	6.19	0 .1697
7.0	665.83	2.79	6.19	0 .1454
14.0	694.87	4.09	7.03	0 .1052
21.0	645.40	6.55	8.91	0 .0672
28.0	589.83	13.64	15.70	0 .0373
35.0	438.73	44.29	52.16	0 .0713

Table C.32: Void Fraction Distribution (CSI) for TS100

Zone Inner & Outer Radii (mm)	Void fraction $\alpha(r)$	1-σ Statistical Uncertainty
.0 – 7.0	0.3622	0.0340
7.0 – 14.0	0.2639	0.0186
14.0 – 21.0	0.1637	0.0132
21.0 – 28.0	0.0865	0.0110
28.0 – 35.0	0.0274	0.0092
35.0 – 38.95	0.0713	0.0107

Cross sectional average, $\langle\alpha\rangle = 0.1050 \pm 0.0052$

Table C.33: Void Fraction Distribution (LSS & C-CSI) for TS100

Zone Inner & Outer Radii (mm)	Void Fraction $\alpha(r)$	
	LSS	C-CSI
.0 – 14.00	0.3017	0.2885
14.0 – 28.0	0.1161	0.1187
28.0 – 39.0	0.0441	0.0449
Cross sectional average, $\langle\alpha\rangle$	0.1053	.1050

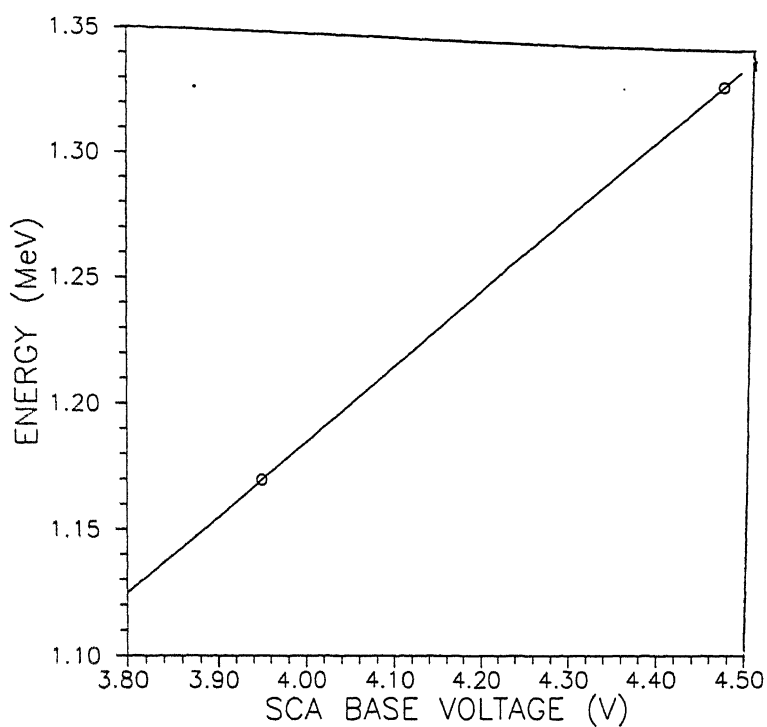Figure D.1: SCA CALIBRATION CURVE

SCINTILLATION DETECTOR AND PRE-AMPLIFIER

ECI Model: SH643

Detection head: NaI(tl) (2 in × 2in)

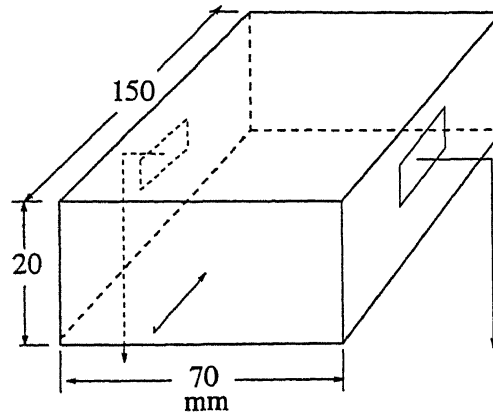Photomultiplier Tube: RCA 8053

Operating voltage: 650 v

Figure D.2: Dimensions of MHD flow channel

D.2 Flow measuring devices

MHD Flow meter

Fluid Velocity, $\bar{U} = \frac{V_{op}}{Bd}\frac{1}{k}$

where, V_{op} = Open circuit voltage (v)

b = Breadth of the channel (0.07 m)

d = Width (0.02 m)

k = End correction factor (0.912)

B = Magnetic Field Strength (0.24 Tesla at 150 Amps.)

Fluid mass flow rate = $\rho_l \bar{U} bd$

= $1242.7 \times V_{op}$

NETP- 1996- M-KUM-TOM